Experiments with Molecules on a Chip

Eine am Fritz-Haber-Institut der Max-Planck-Gesellschaft entstandene
und im Fachbereich Physik der Freien Universität Berlin eingereichte

Dissertation
zur Erlangung des Grades eines
Doktors der Naturwissenschaften

vorgelegt von

Silvio Marx

geboren in Leipzig
Deutschland

Berlin 2016

ERSTGUTACHTER:
Prof. Dr. Gerard Meijer
Radboud Universiteit Nijmegen und
Fritz-Haber-Institut der Max-Planck-Gesellschaft

ZWEITGUTACHTER:
Prof. Dr. Karsten Heyne
Freie Universität Berlin

TAG DER DISPUTATION:
29.06.2016

Kurzfassung

Diese Arbeit befasst sich mit kalten Molekülen auf einem Mikrochip. Kalte und ultrakalte Moleküle könnten einerseits hochpräzise Messungen von Moleküleigenschaften sowie deren Verhalten auf Quantenebene ermöglichen. Andererseits könnte man mit ihnen versuchen hochgenau kontrollierte chemische Reaktionen zu studieren oder einen Quantencomputer bauen.

In den hier vorgestellten Experimenten werden elektrisch neutrale, polare Moleküle in tieffeldsuchenden Quantenzuständen mittels elektrischer Felder auf dem Mikrochip gefangen und abgebremst, indem der Starkeffekt ausgenutzt wird, also die Energieniveauverschiebung von Atomen und Molekülen im elektrischen Feld. Nach der Manipulation der Moleküle auf dem Chip können diese quantenzustandsabhängig detektiert werden (REMPI-Methode).

Zuerst wurden CO Moleküle, welche im oberen Λ-Doublet Zustand des $a^3\Pi_1, v = 0, J = 1$ Zustands präpariert wurden, auf dem Chip gefangen und in dessen Mitte mit einem Infrarotlaser zum $J = 1$ oder $J = 2$ Rotationszustand des Vibrationszustands $v = 1$ angeregt. Dies konnte experimentell nachgewiesen sowie theoretisch analysiert werden, wobei die Moleküle die ganze Zeit gefangen waren.

Als Zweites wurden CO Moleküle auf dem Chip detektiert und die Struktur der zuvor gefangenen Molekülwolken mehrerer Fallen räumlich aufgelöst, welche 120 µm von einander entfernt sind, wofür der Chip mit Ionenlinsen erweitert wurde. Damit konnte die Temperatur der Wolken gemessen werden, indem die ballistische Expansion der Moleküle zeitlich verfolgt wurde; entweder durch Vergleich mittels Simulationen ($T = 11 \pm 1$ mK) oder durch Anwenden eines Expansionsmodells ($T = 13 \pm 3.5$ mK), welches auch im Bereich der ultrakalten Atome verwendet wird. Dies ermöglichte die Detektion der Manipulation des besetzten Phasenraums der gefangenen Moleküle, indem diese in den Fallen adiabatisch expandiert wurden. Damit konnte die Temperatur der Moleküle auf ca. ein Drittel der Ausgangstemperatur reduziert werden.

Drittes Ziel war das Fangen von Ammoniakmolekülen im Grundzustand, welches einerseits eine längere Fangzeit ermöglichen sollte und andererseits zeigen würde, dass auch andere Moleküle auf dem Chip gefangen werden können. Die Moleküle $^{14}NH_3$, $^{14}ND_3$ und $^{15}ND_3$ im $|v_{\mathrm{Inv}} = 1, J = 1, K = 1\rangle$ Zustand des Grundzustands $\widetilde{X}$ wurden dafür getestet. Es konnte kein Signal von gefangenen Molekülen gemessen werden. Dies wird auf nichtadiabatische Übergänge zurückgeführt, die zu großen Verlusten aus den Fallen führen.

Als Letztes wird in dieser Arbeit ein neuer chipbasierter Starkabbremser vorgestellt, der eine miniaturisierte Version eines „traveling-wave“-Ringabbremsers darstellt. Dieser Chip sollte wesentlich mehr Moleküle fangen können als der bisher benutzte Chip. Durch verbesserte Elektronik sollte es möglich sein, Moleküle direkt vom Molekülstrahl (bis ca. 360 m/s) zu fangen und zum Stillstand zu bringen, anders als mit bisherigen großen Ringabbremsern. Der Chip befindet sich bisher noch in der Entwicklung, um ihn mit der vollen Spezifikation (Spannung) betreiben zu können. Nach ersten Simulationen sollte der Chip gut funktionieren, was aber noch in Experimenten bestätigt werden muss.

Abstract

The subject of this thesis's work is research of cold molecules on a microchip. On the one hand, cold and ultracold molecules might allow high-precision measurements of molecular properties and the determination of their behavior at the quantum level. On the other hand, one could try to study highly controlled chemical reactions or to build a quantum computer with their help.

In the experiments presented here, electrically neutral, polar molecules in low-field-seeking states are trapped and decelerated on a microchip with the help of electric fields. This exploits the Stark effect: the energy level shift of atoms and molecules in an electric field. After manipulation on the chip the molecules can be detected quantum-state-specifically via the REMPI method.

At first, CO molecules were prepared in the upper Λ-doublet component of the $a^3\Pi_1, v = 0, J = 1$ state, trapped on the chip and get vibrationally excited by an infrared laser in the middle of the chip to the $J = 1$ or $J = 2$ rotational state of the vibrational state $v = 1$. This could be shown experimentally and was analyzed theoretically for molecules which were trapped at all times.

Secondly, CO molecules were detected on the chip and the structure of previously trapped molecule clouds of several of the only 120 µm spaced traps was spatially resolved. For this purpose the chip was extended with an ion lens setup, which enabled the determination of the temperature of the clouds by following the free ballistic expansion of the molecules in time; either by comparing the data to trajectory simulations ($T = 11 \pm 1$ mK) or by applying a ballistic expansion model ($T = 13 \pm 3.5$ mK), comparable to the method used by the ultracold atom community. The spatial imaging enabled the observation of a phase-space manipulation scheme, which adiabatically expanded the molecules in the trap and significantly reduces their temperature to approximately one third of their initial value.

The third goal was to trap ground state ammonia molecules, which should extend the trapping time and would show that also other molecules could be trapped on the chip. The ammonia isotopologues $^{14}NH_3$, $^{14}ND_3$, and $^{15}ND_3$ in the $|v_{\mathrm{Inv}} = 1, J = 1, K = 1\rangle$ state of the electronic ground state $\widetilde{X}$ were used. No signal could be measured from trapped molecules, which is attributed to large nonadiabatic transitions to untrappable quantum states, leading to severe trap loss.

At last, a new chip-based Stark decelerator is presented, which is a miniaturized version of the so-called "traveling-wave" ring decelerator. This chip-based decelerator should be able to trap more molecules compared to the chip that was used so far, and due to improved electronics it should be able to decelerate molecules from molecular beam velocities of approximately 360 m/s down to a standstill, in contrast to large-scale traveling-wave decelerators so far. The chip is still in development to achieve operation with the full specification (voltage). Performance simulations show the usefulness of this design, which needs to be tested in experiments.

Contents

CHAPTER 1

General Introduction

Miniaturization

Miniaturization of experimental tools has led to a series of exciting developments. Miniaturization improved the performance of devices in many fields, led to ever decreasing cost of production and increased the amount of tasks a single small device can perform. Notably in microelectronics it is observed that the size of a transistor shrinks exponentially fast (“Moore’s law”). This fast miniaturization is one of the main reasons why ever more integrated microchips with new functionality and increased performance can be built.

For chemistry, miniaturization of laboratory devices and the integration of them on a small surface area will ultimately lead to the so-called lab-on-a-chip. On a lab-on-a-chip, analysis of chemical substances might be performed more accurately, faster, cheaper, and with higher transportability than compared to standard methods. [Daw06] The lower cost of analysis is predominantly the result of a lower cost of production, of reagents, and also of reduced waist disposal. Continuing miniaturization will at some point lead to the insight that effects caused by the chip itself on the small amounts of reagents, e.g., capillary forces and interactions with the bulk material, will perturb the analysis. One way of solving these challenges is to avoid contact with the chip material, which might be done by manipulating the reagents with electric or magnetic fields only.

Atomic physics greatly benefited from miniaturization as well, which lead to the development of the atom chip [Hänsel01, Folman02, Fortàgh07, Reichel10]. The two main reasons for the success of the atom chip are the efficient laser cooling of atoms [Metcalf99] to low temperatures and the creation of large field gradients (i.e. forces) with small structures on the chip surface to enable the trapping of significant amounts of atoms. Today, the manipulation of atoms with this method is already quite mature. [Fortàgh07] Among others, applications are rapid Bose-Einstein condensation [Hänsel01], matter-wave interferometry and inertial and gravitational field sensing [Schumm05, vanZoest10], quantum computation [Ospelkaus11], and many-body non-equilibrium physics [Gring12].

Cold Molecules

Research with cold molecules offers various advantages over research with ultracold atoms, such as the degrees of freedom related to their vibrations and rotations, their possible permanent dipole moment, their complex symmetries, or the interactions between each other that can extend over long distances. Cold molecules can be used to address fundamental questions of science.

Molecules are used, for instance, to search for an electric dipole moment of the electron. One scheme to achieve this is by fully polarizing (heavy neutral) dipolar molecules in a laboratory electric field, which effectively creates very high internal fields in the molecule. This enables to push down the limits on a possible electric dipole moment of the electron by observing a possible energy shift of the dipole in the very high electric field, which might be observable in high-resolution spectra. [Baron14]

Molecules can also be used to address questions on fundamental symmetries in physics. One of these symmetries is parity, which describes the relation between a reflected object to its original (unreflected) counterpart. If a force violates this symmetry, a reflected objected might show different properties compared to the unreflected version of it. This could be manifested in a difference in energy levels between the two objects, which could be revealed by observing energy shifts in high-resolution spectra of enantiomers of molecules [Daussy99] (i.e. non-superposable mirror images of itself). The weak force has been shown to violate this symmetry, however the quantification of the effect has to be explored.

The very accurate predictions of electrodynamic phenomena at the quantum level via the theory of quantum electrodynamics (QED) can be tested directly using high-resolution spectroscopy of rotational levels in cold hydrogen molecules. [Salumbides11] The measurements of the rotational level energies fit perfectly well with the predictions of QED and relativistic effects so far.

Despite this very accurate description of the universe using mathematical laws, several fundamental parameters in the equations need to be determined experimentally; the fundamental constants, such as the gravitational constant G, the fine-structure constant α, the Boltzmann constant $\mathrm{k_B}$, or the proton-to-electron mass ratio μ_{pe}. Cold molecules might play an important role in the determination of these constants and to find a possible variation of them. The Boltzmann constant has been determined with precise laser spectroscopy of ammonia [Daussy07] rather than by thermodynamical methods. A temporal variation of μ_{pe} has been tested for by analyzing rovibrational spectra of the SF_6 molecule [Shelkovnikov08] and in molecular hydrogen spectra [Salumbides08]. Even over cosmic time scales this has been evaluated by analyzing methanol (CH_3OH) spectra of earth-bound and astronomical sources at early times during of the universe [Bagdonaite13]. A dependence of μ_{pe} on the mass density has been investigated by comparing laboratory and astronomical CH molecule microwave spectra [Truppe13].

Cold molecules could be used as qubits by orienting their dipole moments in a high electric field gradient [DeMille02], or by combining a superconducting microwave resonator and a long lived rotational states of ultracold molecules to achieve entanglement between qubits [André06], needed for building a quantum computer.

In chemistry, applications like collisions and reactions between molecules are of major importance and might be studied at the quantum level using selected quantum states at low interaction energies using slow beams of atoms and dipolar molecules [Krems08, Tscherbul08, Vogels15].

To perform the aforementioned experiments on cold molecules, they have to be generated before. One way is to use the already existing molecule of interest and supersonically expanding a gas mixture [Morse96] containing this molecule into vacuum, during which translationally and internally cold and slow beams of molecules are generated. These molecules can be trapped and decelerated using the interaction of an electric or magnetic dipole moment in the molecule with a high electric or magnetic field gradient. Devices such as Stark and Zeeman decelerators are capable of generating these gradients and translational temperatures reached with these decelerators are on the order of 10–100 mK.

Another method is cryogenic buffer gas cooling [Doyle95], where the molecular gas is cooled while flowing through a bath of cool atoms (the buffer gas) like He. After leaving the bath, the molecules enter an electric guide, which filters out molecules with the desired velocity and quantum state. With this method, translational temperatures on the order of 1 K are reached.

Ultracold molecular samples can also be achieved by first creating a cloud of ultracold atoms and then by binding them together via photo-association [Stwalley99], in which two colliding atoms absorb a photon from a laser to form an excited diatomic molecule ($T \approx 0.1$ mK). Alternatively, at ultracold temperatures on the order of 10^{-4} mK, a Feshbach resonance [Feshbach58] can be exploited to form molecules. When the interaction potential of two unbound particles almost matches the energy of a bound state, i.e., a rotational state of a molecule formed by the two atoms, ultra-cold molecules can be created.

Cold Molecules on Chips

One approach to combine the prospects offered by cold molecule research with the advantages of miniaturization is the molecule chip [Meek09b, Englert11, Marx13], which is the molecular analogue of the atom chip or ion chip [Stick06, Ospelkaus11]. At the time the experimental work for this thesis began, the molecule chip used throughout this thesis had already been developed and had been used for a variety of applications, see Reference [Meek10]. Molecules could be loaded and trapped on the chip directly from a molecular beam. Trapped molecular ensembles could be guided over the chip surface and could be decelerated to standstill within a few cm of chip length. Apart from the external degrees of freedom, rotational transitions were induced in the molecules on the chip, thereby demonstrating the manipulation of the internal degrees of freedom as well. [Santambrogio11]

This Thesis

The goal of my thesis research was to explore the capabilities of the chip technology beyond the manipulation of the position, velocity and rotational states of trapped molecules. Therefore, the manipulation of the internal degrees of freedom was extended to induce (ro-)vibrational transitions of trapped molecules over the chip.

Then, with the capability of loading and trapping molecules on the chip and manipulating their internal and external degrees of freedom, only the detection of them on the chip remained to be shown to demonstrate that the chip is a fully integrated environment for working with samples of cold molecules. This is particularly interesting because information about the spatial and velocity distribution of trapped molecules is quickly washed out after the molecules leave the traps and the chip. Therefore, a detection zone was implemented on the chip and on-chip detection was finally demonstrated. Molecules are ionized after being released from the traps and a set of electrostatic lenses images the initial molecular distribution onto a detector. With this on-chip detection method, not only time resolved ion counting can be performed, but also spatial images can be captured, giving access to phase space information of trapped molecules. With the possibility of spatial imaging it could be shown that the phase space distribution of the ensembles of trapped molecules can be manipulated on the chip by adiabatically expanding the trapped molecules, thereby reducing the temperature of the trapped ensemble.

Furthermore, it is desirable to show that other species can also be trapped and manipulated on the chip, in particular molecules in their ground state, which would enable longer trapping and manipulation times. Therefore, different ammonia isotopologues in their ground state were tried but none of these could be trapped thus far.

Although the density of molecules trapped on the chip is analogous to that of the molecules captured in macroscopic decelerators, the small size of the microtraps results in a very low number of trapped molecules. Therefore, a different decelerator technology was developed to tackle this problem. This new decelerator offers a larger trap volume and depth.

The content of this thesis is presented in five chapters. In Chapter 2, a theoretical description about the relevant electronic, vibrational and rotational energy states of the carbon monoxide and ammonia molecule is provided, which is useful for the understanding of the content of later chapters. Then, the basics for working with a molecular beam and the microchip is presented. Particularly interesting for most chapters is the description of the traps on the chip and the manipulation via guiding and deceleration. Furthermore, the excitation of CO molecules into the metastable electronic state, which is needed for trapping, as well as the detection of both molecules is explained. Finally, a brief overview of how to simulate the trajectories of molecules on and off the chip is included.

Chapter 3 reports on the vibrational excitation of trapped CO molecules on the chip. To understand how the vibrational excitation with an infrared laser (IR) works for trapped molecules, it is initially studied with free-flying molecules in a homogeneous and variable electric field. The analysis reveals the dependence of the excitation on the electric field strength and the polarization of the laser relative to the electric field. Furthermore, the excitation of trapped molecules and measurements of guided and vibrationally excited molecules are shown.

Chapter 4 presents the spatially resolved on-chip molecule detection with a new detection setup. The spatial imaging technique is described and used to determine the temperature of previously trapped molecules by following the free ballistic expansion of the molecular clouds after the release from the traps. A model is presented how to extract a temperature directly from the measurements, without the need of performing trajectory simulations. Furthermore, the manipulation of the temperature on the chip can be verified using the imaging technique. Finally, the manipulation process is explained with the help of two simple models: molecules in a harmonic trap and the expansion of an ideal gas.

Chapter 5 describes the efforts to trap ammonia molecules on a chip. While previously only electronically excited, metastable CO molecules were used on the chip, it is desirable to show the trapping of ground state molecules. A setup is presented to achieve this goal. As it turns out, no trapped ammonia molecules could be detected in the described way. The used methods are checked and an alternative approach is presented, creating a small offset electric field along the traps to reduce possible nonadiabatic transitions, which might have prevented the trapping on the chip. Unfortunately, this did not help to trap ammonia molecules either.

Chapter 6 describes the alternative chip design. While the original chip has a planar electrode geometry, the new design incorporates the concept of a three-dimensional ring electrode, which was successfully implemented on the scale of the large traveling-wave Stark decelerator. [Osterwalder10, Meek11a] A problem encountered with the macroscopic traveling-wave decelerators is posed by the rather demanding specifications of the driving electronics. The new design of the chip (referred to as the “ring chip”) has been developed starting from the commercially available electronic components and scaling the physical design accordingly. The working principle of the traveling-wave decelerator is explained in this chapter, followed by the design of the new chip and the analysis of the generated traps.

CHAPTER 2

Molecules on a Chip

2.1 Introduction

All experiments presented in this thesis are done using cold samples of polar molecules. The molecules are cooled by expanding a gas mixture into vacuum through the nozzle of a pulsed valve. The supersonic beam [Morse96] of polar molecules is then captured in the moving microtraps created by an array of microstructured electrodes deposited on a glass substrate. The electric microtraps are three-dimensional minima of electric field strength and polar molecules in low-field-seeking (lfs) quantum states can be trapped in there. A state is lfs if its Stark energy increases with increasing electric field strength. Molecules can show this effect in their electronic ground state. However, in the case of CO it is necessary to selectively excite the molecules with a laser to a metastable state, in order to increase the magnitude of the molecular electric dipole moment. Once the molecules are trapped, they can be either guided over the surface of the microchip or decelerated to any velocity between 400 and 0 m/s by applying the appropriate voltages to the chip electrodes. The microtraps have a tubular shape, they are approximately 4 mm long with a diameter of approximately 20 µm. Typical trap depths for metastable carbon monoxide molecules are of the order of a few tens of mK.

In this chapter first some spectroscopic properties of carbon monoxide and ammonia will be introduced, molecules that have been used in the experiments. A discussion about the molecular beam, the chip, the traps and the molecule detection will follow, serving as background information for the experiments. A brief summary of how numerical trajectory simulations for the extraction of phase space information are performed completes the chapter.

2.2 Molecules

A general description of the molecular quantum states that are relevant for the experiments is presented, without going into the detail of hyperfine structure. Furthermore, it will be explained how the molecular energy states behave in an electric field because this behavior is exploited throughout the thesis for the manipulation with the electric fields. This is done both for CO and ND_3 molecules.

2.2.1 Carbon Monoxide

The simplest molecule one can think of consists only of two atoms, a dimer. If the two atoms are equal the molecule cannot show a dipole moment and cannot be easily manipulated with inhomogeneous electric fields. However, a heteronuclear dimer generally has a dipole moment and CO is the molecule that will be analyzed here. A diatomic molecule has only one vibrational mode, to which a vibrational frequency ω_e is associated, and a rotation about an axis perpendicular to the internuclear axis, with the associated constant B.

Vibrations

The vibrational motion of a diatomic molecule can be treated as the oscillation of a single particle with effective mass μ_e around the center of mass. The effective mass μ_e is defined as $1/\mu_\text{e} = 1/m_\text{C} + 1/m_\text{O}$. The interaction potential $\hat{V}$ for low vibrational states can be treated as being harmonic, so $\hat{V} = \frac{\mu\omega_e^2}{2}\hat{x}^2$, where $\hat{x}$ is the displacement (operator) of the particle from equilibrium and ω_e the angular oscillation frequency. The Hamiltonian of this harmonic oscillator system is

$$\hat{\mathcal{H}}_\text{Vib,HO} = \frac{1}{2\mu_\text{e}}\hat{p}^2 + \frac{\mu_\text{e}\omega_e^2}{2}\hat{x}^2 \tag{2.1}$$

and has the eigenvalues

$$\mathcal{E}_\text{Vib,HO} = (v + \frac{1}{2})\omega_e\hbar. \tag{2.2}$$

The vibrational quantum number v is restricted to positive integer values starting from 0. This approximation is not perfect and it breaks down for higher vibrational quantum states; the potential is not perfectly harmonic and the anharmonic contributions need to be taken into account. Additional terms in the energy thus appear as corrections to the harmonic oscillator energies in a power series like

$$\mathcal{E}_{\mathrm{Vib,AO}} = (v + \frac{1}{2})\omega_e \hbar - (v + \frac{1}{2})^2 \omega_e x_e \hbar + (v + \frac{1}{2})^3 \omega_e y_e \hbar + \dots, \tag{2.3}$$

where the parameters ω_e, $\omega_e x_e$, $\omega_e y_e$, $\dots$ can be determined experimentally. [Atkins05] The energy differences between the lowest neighboring vibrational levels in the $a^3\Pi$ state are not constant but are given by 1715 cm^{-1}, 1686 cm^{-1}, and 1658 cm^{-1} [Huber79].

Angular Momenta and Rotations

To describe the spectroscopic patterns of diatomic molecules and to model the molecule's behavior beyond vibrations, the various terms in the Hamiltonian are classified according to their strength. [Lefebvre-Brion04] The CO molecule in the $a^3\Pi$ state is well described in the so-called Hund's case (a) coupling case. This coupling case describes the situation in which the dominating interaction is the electrostatic coupling of the electronic orbital angular momentum $\hat{\vec{L}}$ of the unpaired electron to the internuclear axis z. In addition, but to a lower degree, the electronic spin angular momentum $\hat{\vec{S}}$ is coupled to $\hat{\vec{L}}$ and, of even lower importance, is the interaction between nuclear rotation and electronic motion.

Unlike L, the total electron spin is a reasonably good quantum number S and its projections can take values $\Sigma = (-S, -S+1, \dots, S-1, S) = (-1, 0, 1)$, while the expectation values for the projections of $\hat{\vec{L}}$ on the internuclear axis can take the value $\Lambda = (-1, 1)$. The total angular momentum $\hat{\vec{J}}$ is formed by the coupling of the nuclear rotation $\hat{\vec{R}}$ with the electronic angular momenta as $\hat{\vec{J}} = \hat{\vec{R}} + \hat{\vec{L}} + \hat{\vec{S}}$. The projection of $\hat{\vec{J}}$ on the internuclear axis z, $\hat{J}_z$, has the eigenvalue $\Omega = |\Lambda + \Sigma| = (0, 1, 2)$ but all experiments presented here are done in the $\Omega = 1$ manifold, so $J = (\Omega, \Omega + 1, \dots) = (1, 2, \dots)$. The projection of $\hat{\vec{J}}$ on an external axis Z, $\hat{J}_Z$, are given the quantum number $M = (-J, -J+1, \dots, J-1, J)$.

In general, the rotation of a three-dimensional body about an arbitrary axis can be described using the 3×3 inertial matrix containing different moments and products of inertia, which is uniquely defined by the mass distribution of the object relative to the axes of rotation. When this matrix is diagonalized, the principal moments (I_A, I_B, I_C) and principal axes ($\vec{a}$, $\vec{b}$, $\vec{c}$) of inertia are found. In the CO molecule, the moment of inertia about the internuclear axis I_A is zero, whereas the two moments through the center of mass, but perpendicular to the internuclear axis, are identical ($I_B = I_C = I$). This gives rise to the rotational constant $B = \frac{\hbar}{4\pi c I}$ (in wavenumbers). With these moments of inertia the CO molecule falls into the linear rotor category. In the $|J, \Omega, M\rangle$ basis the total angular momentum and its projections obey

$$\begin{aligned} \langle J, \Omega, M| \hat{\vec{J}}^2 |J, \Omega, M\rangle &= J(J+1), \\ \langle J, \Omega, M| \hat{J}_z |J, \Omega, M\rangle &= \Omega, \\ \langle J, \Omega, M| \hat{J}_Z |J, \Omega, M\rangle &= M. \end{aligned} \tag{2.4}$$

The true eigenfunctions of the system must simultaneously be eigenfunctions of the inversion operator E^* in free space, which inverts coordinates in the molecule frame. The $|J, \Omega, M\rangle$ wavefunctions are not eigenfunctions of E^* and their parity is not defined. Definite parity wavefunctions can be constructed from linear combinations of $|J, \Omega, M\rangle$ and $|J, -\Omega, M\rangle$ states and are denoted with $|J, \Omega, M, \epsilon\rangle$, including a parity index $\epsilon = \pm 1$.

It can be shown that the rotational energy spectrum of the rigid rotor is then given as

$$\mathcal{E}_{\mathrm{Rot}} = BJ(J+1). \tag{2.5}$$

However, the vibrational potential is flattened when the molecule is in high rotational states. This is known as centrifugal distortion and yields correction terms to be added to the rotational energy as

$$\mathcal{E}_{\mathrm{Rot,CD}} = BJ(J+1) - D\left[J(J+1)\right]^2 + H\left[J(J+1)\right]^3 - \dots, \tag{2.6}$$

where D, H, ... are the centrifugal distortion constants [Martin91]. Since the experiment will be carried out in the $|\Omega| = 1$ manifold of the $a^3\Pi$ state the first rotational level is $J = 1$. The energy differences between the first four neighboring rotational levels ($J = 1, 2, 3, 4$) in the $a^3\Pi_1, v = 0$ state are 6.72 cm^{-1}, 10.1 cm^{-1}, and 13.5 cm^{-1}. In fact, the rotational constants show also a weak dependence on v, which reduces the energy splittings slightly in the $v = 1$ state to 6.65 cm^{-1}, 10.0 cm^{-1}, and 13.3 cm^{-1} [Huber79].

Stark Effect

The energy of a polar molecule in an electric field is described by the Hamiltonian $\hat{\mathcal{H}}_{\mathrm{Stark}} = -\vec{\mu}\vec{E} = -|\vec{\mu}||\vec{E}|\cos\hat{\Theta}$, the so-called Stark energy. The dipole moment $\vec{\mu}$ is defined as the expectation value of the orientation of the dipole operator, $\langle\hat{\vec{\mu}}\rangle$. The direction of the dipole moment is also defined as $\vec{\mu} = q\vec{r} = \mu\vec{z}$, where $\vec{r}$ points from the negative to the positive charge q in the molecule and $\vec{z}$ is along the internuclear axis z. The electric field $\vec{E} = |\vec{E}|\vec{Z}$ points along the external Z-axis.

Depending on the orientation of the quantum mechanical dipole there are basically three cases how the dipole can behave in an inhomogeneous electric field. When the dipole moment $\vec{\mu}$ is oriented parallel to $\vec{E}$, the energy in the molecular quantum state decreases with increasing electric field strength. This is a high-field-seeking (hfs) state. If the vectors are perpendicular, the energy will not change and the state is non-field-seeking (nfs). In the last case, the vectors are anti-parallel and the energy increases with increasing field strength. This state is called low-field-seeking (lfs). Only lfs states are used in the experiments described in this thesis.

In order to calculate the behavior of a molecule in the electric field, the Stark energy is treated as a perturbation. Thus, one can write

$$\begin{aligned}\hat{\mathcal{H}} &= \hat{\mathcal{H}}_0 + \lambda\hat{\mathcal{H}}_{\text{Stark}} \\ &= \hat{\mathcal{H}}_{\text{El}} + \hat{\mathcal{H}}_{\text{Vib}} + \hat{\mathcal{H}}_{\text{Rot}} - \lambda|\vec{\mu}||\vec{E}|\cos\hat{\Theta}.\end{aligned} \tag{2.7}$$

This leads to an expansion of the energy of the system in state $|n\rangle$

$$\mathcal{E}_n = \mathcal{E}_n^{(0)} + \lambda\mathcal{E}_n^{(1)} + \lambda^2\mathcal{E}_n^{(2)} + ... \tag{2.8}$$

The parameter n represents the quantum numbers defining the state of the system (electronic, vibrational and rotational part). Since the couplings between electronic and vibrational states via the Stark Hamiltonian are much weaker than for the rotational part (also due to the larger energy separation between them), the quantum numbers J, Ω, M and ϵ are usually sufficient. The zeroth order term in the energy expansion $\mathcal{E}_n^{(0)}$ is simply the energy of the unperturbed system at zero electric field. The first order correction, which is the most important contribution for low electric fields, is

$$\begin{aligned}\mathcal{E}_n^{(1)} &= \mathcal{E}^{(1)}(J,\Omega,M) \\ &= \langle J,\Omega,M,\epsilon'|\,\hat{\mathcal{H}}_{\text{Stark}}\,|J,\Omega,M,\epsilon\rangle \\ &= -|\vec{\mu}||\vec{E}|\,\langle J,\Omega,M,\epsilon'|\cos\hat{\Theta}\,|J,\Omega,M,\epsilon\rangle\,.\end{aligned} \tag{2.9}$$

For states where $\epsilon' = \epsilon$, $\mathcal{E}^{(1)}(J, \Omega, M)$ is zero because $\hat{\mathcal{H}}_{\text{Stark}}$ is an odd function.[1]

The solution to Equation 2.9 using the direction cosine elements [Zare88] gives

$$\mathcal{E}^{(1)}(J, \Omega, M) = -|\vec{\mu}||\vec{E}|\frac{M\Omega}{J(J+1)}. \tag{2.10}$$

Corrections of order $\mathcal{E}_n^{(2)}$ (coupling different values of J) and higher are omitted because of their small effect in the fields used in the experiments (fields $\leq$ 5 kV/cm give at most 1% Stark energy difference for the $a^3\Pi_1, v = 0, J = 1, M\Omega = -1$ lfs state). Altogether, including the energy splitting between the different parity states (due to Λ-doublet splitting $\mathcal{E}_\Lambda$) to the Stark Hamiltonian ($\hat{\mathcal{H}} = \hat{\mathcal{H}}_{\text{Split}} + \hat{\mathcal{H}}_{\text{Stark}}$ for each rotational level), for setting up the eigenvalue problem in the $|J, \Omega, M, \epsilon\rangle$ basis one needs to solve the determinant equation for the energy of the molecule in the field, $\mathcal{E}_{\text{Stark}}$:

$$\begin{vmatrix} \frac{\mathcal{E}_\Lambda}{2} - \mathcal{E}_{\text{Stark}} & -|\vec{\mu}||\vec{E}|\frac{M\Omega}{J(J+1)} \\ -|\vec{\mu}||\vec{E}|\frac{M\Omega}{J(J+1)} & \frac{-\mathcal{E}_\Lambda}{2} - \mathcal{E}_{\text{Stark}} \end{vmatrix} = 0. \tag{2.11}$$

The solutions are found to be

$$\mathcal{E}_{\text{Stark}}(J, \Omega, M) = \pm\sqrt{\left(\frac{\mathcal{E}_\Lambda}{2}\right)^2 + \left(|\vec{\mu}||\vec{E}|\frac{M\Omega}{J(J+1)}\right)^2}, \tag{2.12}$$

and the force acting on the molecule is

$$\vec{F} = -\vec{\nabla}\mathcal{E}_{\text{Stark}}. \tag{2.13}$$

2.2.2 Ammonia

The geometrical structure of the ammonia molecule in the electronic ground state is not planar because the nitrogen atom possesses a lone electron pair which distort the shape. In fact, the structure has been determined to be pyramidal, where the base plane is defined by the three hydrogen atoms forming an equilateral triangle [Townes75] and the nitrogen atom sits in the apex of the pyramid. The symmetry axis of the molecule goes through the center of the base and the nitrogen atom. The angle between this symmetry axis and

---

[1] $\hat{\mathcal{H}}_{\text{Stark}} = -\vec{\mu}\vec{E} = -\mu E_z z$ is an odd function under space inversion because $z \to -z$ implies $\hat{\mathcal{H}}_{\text{Stark}} \to -\hat{\mathcal{H}}_{\text{Stark}}$. Therefore, the expectation value of $\hat{\mathcal{H}}_{\text{Stark}}$ (Equation 2.9) using levels of the same parity would vanish.

one N–H bond axis is called the umbrella angle ρ (where, e.g., $\rho = 0°$ would correspond to a “closed umbrella” during sunshine and $\rho \approx 90°$ to an opened one during rain). The potential $V(\rho)$, describing the molecule’s energy as a function of the umbrella angle, is of major importance for the description of the molecule’s Stark effect because it determines the energy level separation between the interacting parity states for ammonia molecules in an electric field. Vibrational oscillations in this potential are called umbrella modes (ν_2) and are associated with the inversion of the molecule.

Inversion

Following [Townes75] the ground state vibrational behavior is determined from the potential $V(\rho)$, showing a double minimum as seen in Figure 2.1, corresponding to the nitrogen atom being on either of the sides of the base plane when in equilibrium. These equilibrium positions appear at approximately ±22° from the planar (90°) geometry (or $\rho_0 = 68°$ and 112°). On either side the nitrogen oscillates around the equilibrium position with an energy in the infrared region because of its zero point energy. However, because it does not cost an infinite amount of energy to bring the nitrogen on the other side of the base plane the potential height between the two minima is finite. Quantum mechanical tunneling through this 2023 cm^{-1} high barrier at $\rho = 90°$ allows the molecule to switch between the two configurations even in the ground state with an energy less than 2023 cm^{-1}. This inversion happens at a rate in the microwave frequency region for the lowest vibrational state and leads to an energy splitting between its substates.

The appearance of the inversion splitting can also be understood by first considering the potential well to be infinitely high and then lowering it to a finite value. For the infinitely high well the nitrogen would be perfectly localized on one side of the base plane. The system would then be described with the two wave functions $|\Psi_\mathrm{l}\rangle$ and $|\Psi_\mathrm{r}\rangle$, having degenerate energy levels. Now, lowering the potential well, there is a nonzero component of each wave function also on the other side. Similarly to CO the true wave functions $|\Psi_\mathrm{Inv}\rangle$ must be eigenfunctions of the inversion operator as well, which can be expressed as linear superpositions of $|\Psi_\mathrm{l}\rangle$ and $|\Psi_\mathrm{r}\rangle$ in the form

$$\begin{aligned} |\Psi_0\rangle &= \frac{1}{\sqrt{2}} \left(|\Psi_\mathrm{l}\rangle + |\Psi_\mathrm{r}\rangle\right) \\ |\Psi_1\rangle &= \frac{1}{\sqrt{2}} \left(|\Psi_\mathrm{l}\rangle - |\Psi_\mathrm{r}\rangle\right) . \end{aligned} \tag{2.14}$$

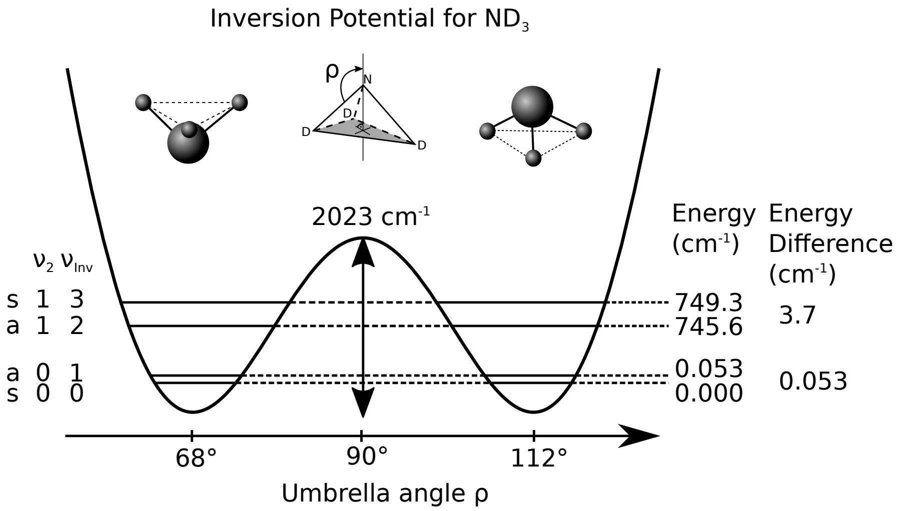

Figure 2.1: Inversion of $^{14}ND_3$, one of the molecule used in the experiment. Splittings and umbrella angles are exaggerated for clarity and are not to scale. The values are taken from References [Swalen62, Špirko83].

Since these functions have a different probability amplitude (especially in the region around the barrier), they are not necessarily expected to have the same energy, which is indeed the case. The symmetric wave function $|\Psi_0\rangle$ has a lower energy than the antisymmetric $|\Psi_1\rangle$. Correspondingly, the vibronic ground states are called $\widetilde{X}(\nu_{\text{Inv}} = 0)$ and $\widetilde{X}(\nu_{\text{Inv}} = 1)$.

As turns out from elaborate calculations [Townes75] the inversion splitting is very sensitive on the reduced mass of the system. The reduced mass is larger for $^{14}ND_3$ compared to $^{14}NH_3$ and decreases the splitting of the vibrational ground state from 0.79 cm^{-1} in $^{14}NH_3$ to 0.053 cm^{-1} in $^{14}ND_3$ [Swalen62]. This turns out to be advantageous for trapping in weak electric fields because then the Stark energy rises faster with electric field strength, see Subsection 2.2.1. This is the main reason why $^{14}ND_3$ is the preferred isotopologue in this experiment.

Rotation

In ammonia, one principal axis of inertia coincides with the symmetry axis of the molecule and its moment of inertia is called I_C. The other two moments of inertia, I_A and I_B are equal and smaller than I_C. This is typical for oblate symmetric tops [Townes75]. The energy levels of the symmetric top are determined from the Hamiltonian

$$\hat{\mathcal{H}}_{\text{Rot}} = B\hat{\vec{J}}^{2} + (C - B)\hat{J}_z^{\,2}, \tag{2.15}$$

where $C = \frac{\hbar}{4\pi c I_{\text{C}}}$ and $B = \frac{\hbar}{4\pi c I_{\text{B}}}$ (in wavenumbers) denote the rotational constants. The rotational eigenenergies are given by

$$\mathcal{E}_{\text{Rot}}(J, K, M) = BJ(J + 1) + (C - B)K^2. \tag{2.16}$$

The quantum number K is the eigenvalue of the projection of the total angular momentum on the internuclear axis z, $\hat{\vec{J}}_z$. Symmetrized eigenfunctions $|J, K, M, \epsilon\rangle$ are analogously obtained as for CO. These eigenenergies are only approximately true for low values of J. For higher rotational quantum numbers J the vibrational potential flattens due to effects like centrifugal distortion. To correct the rotational energies, additional terms are added in a power series like form. The energies then become

$$\mathcal{E}_{\text{Rot,CD}}(J, K, M) = BJ(J+1)+(C-B)K^2-D_J[J(J+1)]^2-D_{JK}J(J+1)K^2-D_K K^4+\dots \tag{2.17}$$

with parameters $D_{J,JK,K} \approx 10^{-6}B$. [Martin91] The lowest rotational energy level of the ^{14}ND$_3$ isotopologue are plotted in Figure 2.2(a). It can be seen how the rotational energy is lowered for increasing values of K due to the oblate structure of the molecule. The energy level most relevant to the experiment is the lowest level showing first order Stark effect, the $|J = 1, K = 1\rangle$ level.

Stark Effect

The calculation of the Stark energy of the ammonia molecule is similar to the CO calculation, except that the angular momentum along the symmetry axis is now described by the quantum number K rather than by Ω. Then, first order perturbation yields

$$\mathcal{E}^{(1)}(J, K, M) = -|\vec{\mu}||\vec{E}|\frac{MK}{J(J + 1)}. \tag{2.18}$$

This perturbation couples the two inversion doublet components for each value of J because these are the closest levels of different parity. The form of the Stark energy of the levels

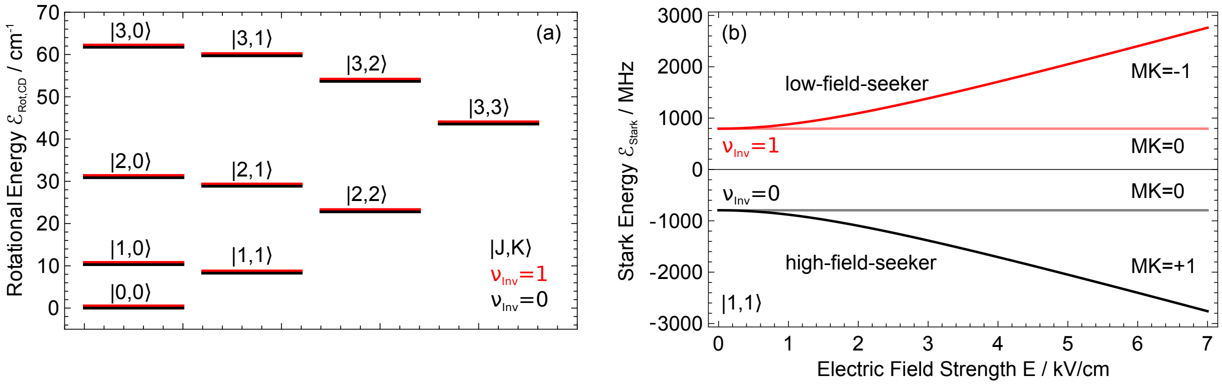

Figure 2.2: Energy levels of the ^{14}ND$_3$ ammonia isotopologue. (a) Rotational manifold up to $J = 3$ for the lowest two inversion states. The inversion splitting is exaggerated and the constants for the calculation are taken from Reference [Fusina86]. (b) Stark effect of the $|J = 1, K = 1\rangle$ rotational state. The Stark energy is much smaller than the energy difference between the rotational states for the field strengths achievable on the chip (1 cm^{-1} $\approx$ 30 GHz).

in the field is similar as well:

$$\mathcal{E}_{\mathrm{Stark}}(J, K, M) = \pm\sqrt{\left(\frac{\mathcal{E}_{\mathrm{Inv}}}{2}\right)^2 + \left(|\vec{\mu}||\vec{E}|\frac{MK}{J(J+1)}\right)^2} \tag{2.19}$$

with $\mathcal{E}_{\mathrm{Inv}}$ the inversion doublet energy splitting in ammonia. The lowest populated level with a first order Stark effect is the $|J = 1, K = 1\rangle$ rotational level, higher rotational levels have a low population.

The Stark energy of the ^{14}ND$_3$ ammonia molecule for the $|\nu_2 = 0, J = 1, K = 1\rangle$ levels is shown in Figure 2.2(b). The figure shows the Stark energy in comparably low electric fields (a few kV/cm), typical for the fields obtained on the chip. The upper as well as the lower state splits into $MK = 0$ and ± 1 which behave differently. The $MK = 0$ levels show no first order Stark effect, whereas the $MK = -1$ and $MK = +1$ levels shift up or down in energy, respectively, with increasing electric field. Significant deviations from this picture would arise at higher electric fields where couplings to neighboring rotational levels come into play. Interactions with other levels are expected to be weak because the energy shift of ≤ 2 GHz (0.067 cm^{-1}) is much less than the energy difference to any perturbing level from the rotational manifold which is on the order of at least a few cm^{-1}.

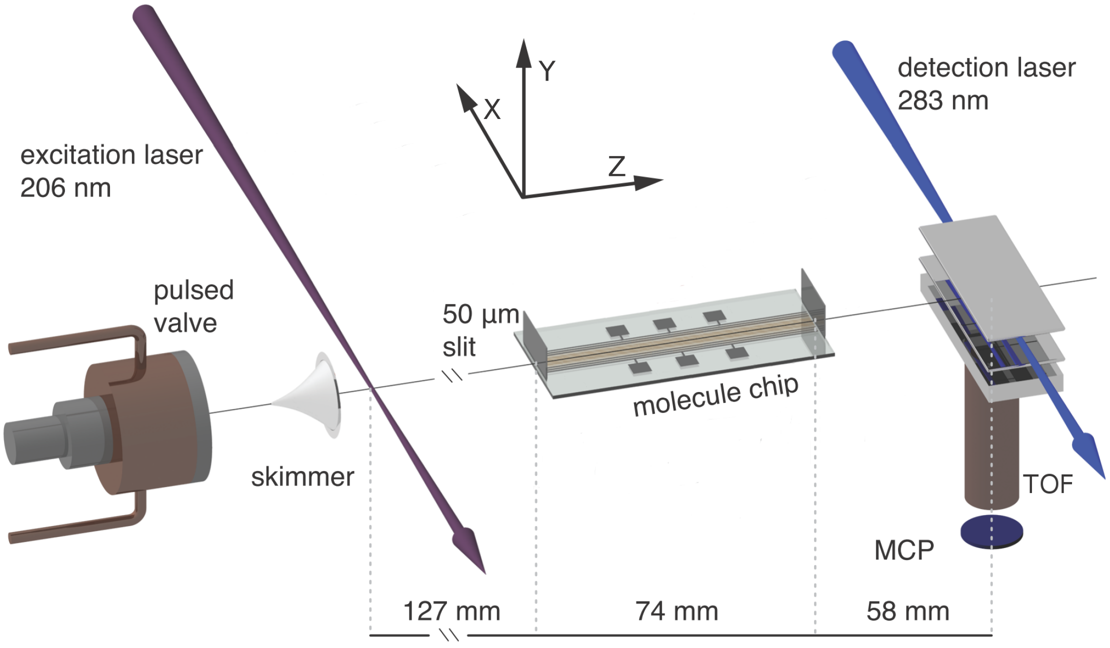

Figure 2.3: Overview of the experimental setup. A molecular beam is generated with a pulsed valve, and is skimmed before the manipulation on the chip occurs. In case of CO, the molecules are excited with a 206 nm laser before the chip. After on-chip manipulation, detection occurs in a time-of-flight (TOF) setup.

2.3 Experimental Setup

The vacuum apparatus consists of a source chamber and a main chamber separated by a 1 mm diameter skimmer. Both chambers are pumped by turbomolecular pumps (1×520 l/s for the source chamber, 2×260 l/s for the main chamber) backed by a membrane pump. Under normal operating conditions, the pressure in the source chamber is approximately 10^{-5} mbar and the pressure in the main chamber is between 10^{-7} mbar and 10^{-6} mbar. The source chamber contains the molecular beam source (the pulsed valve), whereas the main chamber contains an excitation laser in the case of CO, the molecule chip manipulation region and a detection setup (laser and TOF spectrometer). For an overview see Figure 2.3.

2.3.1 Molecular Beam

A supersonic molecular beam is produced by expanding a gas mixture of a noble gas with CO through the nozzle of a modified General Valve Series 99 (Parker). The temperature of the valve's body is controlled with a flow of nitrogen, whose temperature is stabilized to

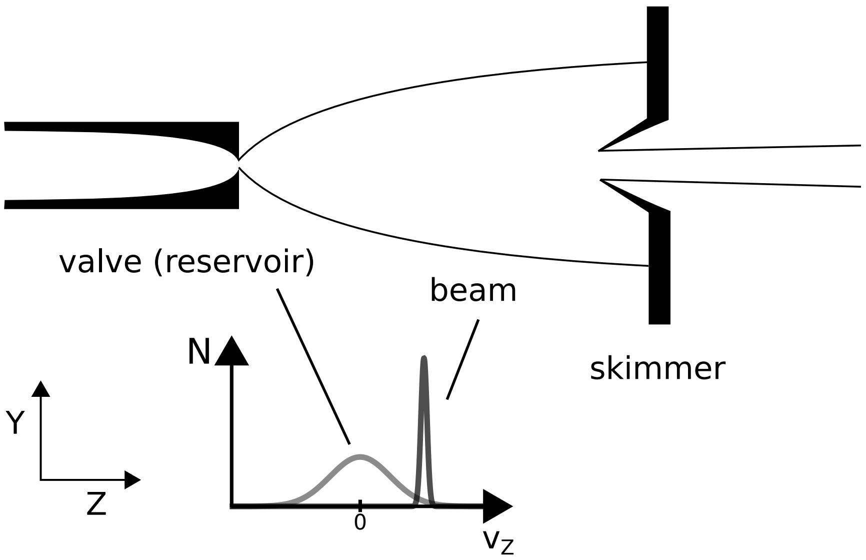

Figure 2.4: Supersonic expansion of a gas from a reservoir into the vacuum chamber. The velocity distribution along the expansion axis (Z) is converted from a broad distribution with average of 0 m/s to a narrow distribution with nonzero average velocity. The beam is skimmed before reaching the experiment.

the desired value between 100 and 300 K using a PID controller. The cooling is achieved by contact with a liquid nitrogen bath, while the heater is an electric resistor. The valve is opened for approximately 100 µs and the whole experiment runs at a repetition rate of 10 Hz. While leaving the valve, the mean free path of the atoms and molecules is much smaller than the nozzle diameter. Therefore, many collisions take place and the rapid, adiabatic expansion cools the molecular beam. Soon after the molecules have left the valve, the cooling process is interrupted and no collisions take place anymore. Typically, the following final temperatures are obtained: translation $\leq$1 K, rotation 5 K and vibration 50 K. The reasons for the different temperatures of the different degrees of freedom are the different relaxation rates. The translational relaxation rate is the highest because there is a continuum of energy states available. The rotational relaxation rate is somehow lower because the energy levels are quantized but the energy separation is small. [Strekalov95] Thus translations and rotations couple rather well. The vibrational relaxation rate is lower predominantly because the energy separation between vibrational states is typically much higher. For an illustration of the expansion see Figure 2.4.

When using a high pressure in the valve reservoir and when the hole of the valve is much larger than the mean free path of the molecules which is the case in the experiment the continuum model of the gas flow may be applied. [Morse96] The gas dynamics can be described using a continuous mass distribution rather than treating the gas as a set of individual particles. This means that the gas flow during the expansion can be treated as adiabatic and isentropic, to a good approximation. Then, the sum of the enthalpy $H(Z) = U + pV$ (internal energy U of the atoms/molecules and energy stored in the reservoir pV) and the kinetic energy of the flowing gas is

$$H(Z) + \frac{1}{2}mv^2(Z) = \text{constant}, \tag{2.20}$$

where Z is the expansion axis and $v(Z)$ the average flow velocity along this axis. The initial enthalpy depends on the temperature of the gas in the valve reservoir, T_0. The flow velocity is then ultimately limited by the conversion of the whole enthalpy of the gas in the reservoir $H(T_0)$ into velocity which yields

$$v_{\text{max}} = \sqrt{\frac{2H(T_0)}{m}}. \tag{2.21}$$

Therefore, the final maximum possible velocity is inversely proportional to the square root of the mass. In the experiments presented in this thesis, molecular beams of light molecules (m = 20 amu for $^{14}ND_3$ and m = 28 amu for ^{12}CO) were produced and a pure beam of either of these molecules has a speed of approximately 1000 m/s at 300 K.

In the experiments, the molecular beam's velocity is reduced linearly during deceleration, but the kinetic energy reduces quadratically with the velocity. Therefore, the slower the initial molecular beam can be, the easiest the experiment will be. Since the operation takes place in the high source pressure regime, the properties of a gas mixture can be described to a good approximation by the weighted averages of the enthalpies and masses. [Morse96] A 20% mixture of ammonia in xenon leads to a maximum velocity of approximately 350 m/s at 300 K. At 200 K the velocity drops to approximately 300 m/s.

The lowest speed and temperature that can be obtained are limited by clustering in the beam. Clustering releases latent heat that heats up the rest of the beam and reduces the number of free molecules. As it depends on the polarizability and temperature of the constituents of the molecular beam, optimal conditions for beams of different molecules are found by empirically choosing different carrier gases and valve temperatures.

Typically, mixtures of 20% CO in Kr at 140 K or 20% ND_3 in Xe at 203 K were used, which both give a final beam speed of approximately 330 m/s. The pressure of the gas mixture in the valve is 2 bar (absolute). Krypton and xenon are inert noble gas atoms, which means they are not expected to interact chemically with the sample molecules. Also, they do not disturb the detection process. The carrier gas atoms and the seed molecules have a very similar velocity distribution after the many collisions between each other despite the different masses. Since the velocity of the particles is faster than the local speed of sound, the beam is called supersonic.

CO Excitation

After the cooling of the gas mixture through supersonic expansion, the CO molecules occupy only the lowest few rotational levels of the $X^1\Sigma^+, v = 0$ ground state. These levels show only a small Stark energy change in the fields producible on the chip. To reach a state with larger Stark energy an excitation to the electronically excited state $a^3\Pi_1, v = 0, J = 1\ (+) \leftarrow X^1\Sigma^+, v = 0, N = 1\ (-)$ is performed. This level shows an order of magnitude larger Stark energy shift compared to the ground state because in addition to the small energy splitting between the neighboring different parity states it has a much larger dipole moment of 1.375 Debye [Wicke72, Woods88]. The spin-orbit manifold with $|\Omega| = 1$ is selected, because transitions to these levels are more than 40 times more intense than transitions to the other spin-orbit components [Gilijamse07]. The particular transition used is the so-called $Q_2(1)$ transition, where Q implies ΔJ=0, where the subindex indicates the spin-orbit manifold with $\Omega = 1$ in the final state, and where (1) means that the transition started from $N = 1$. The two different parity components of the $a^3\Pi_1, v = 0, J = 1$ state are split by only 394 MHz in zero field due to the Λ-doubling; the upper one (+) is lfs and the lower one (−) is hfs. The parity must change in this $Q_2(1)$, dictated by the selection rules of an electric dipole transition. Since the ground state has spin $S = 0$ and the excited state has spin $S = 1$, strictly this transition would not be allowed because the spin must be preserved in an electric dipole excitation. In reality the $a^3\Pi$ triplet state is slightly mixed with the $A^1\Pi$ singlet state through spin-orbit-interaction, giving the $a^3\Pi_1 \leftarrow X^1\Sigma^+$ transition some intensity. Molecules in this state are metastable with a radiative lifetime of 2.6 ms [Gilijamse07], long enough for the experiments. For further details about the transition see References [Meek10, Jongma97].

UV-Laser System (OPO)

Technically, the aforementioned transition is induced via absorption of laser photons of 206 nm wavelength. The laser has a typical energy of approximately 1 mJ in a 5 ns long pulse. The beam is focused to reach a higher fluence, exciting more molecules in the molecular beam. The bandwidth of approximately 200 MHz (FWHM) allows one to excite only the upper (lfs) Λ-doublet component of the $a^3\Pi_1$, $v = 0$, $J = 1$ state.

To generate the 206 nm light a pulsed Nd:YAG laser at 532 nm is used (Spectra Physics QuantaRay Pro Series) as the primary source of laser light which is split in two parts. The first part is frequency doubled to 266 nm in a BBO crystal (single pass) and travels through an optical delay line for later temporal and spatial overlap with the converted second part. The second part of the 532 nm beam pumps an optical parametric oscillator cavity (OPO) with two KTP crystals, providing a 917 nm and a 1267 nm beam of which only the first is used. The output beam characteristics of the OPO is determined by the phase matching bandwidth of the crystals, the seed light, and the cavity modes. To control the output frequency of the OPO it is injection seeded using a commercial cw diode laser system (Toptica DL 100 Pro) at 917 nm. Both parts, the 266 nm and the 917 nm beam, are overlapped and in a further BBO crystal the final 206 nm pulse is obtained by sum frequency generation. This beam is then used to excite the CO molecules into the metastable CO* ($a^3\Pi_1$) state. The layout of the laser is shown in Figure 2.5, which is a replica of the laser described in [Velarde10].

The most notable difference from the original design is the locking mechanism. In the original design, in each experimental cycle the OPO cavity's resonance position was determined and it was held at this resonance during the IR pulse generation with the pump beam. In this setup the cavity length is held at resonance using a small periodic modulation of the cavity length (10 mV peak-to-peak at 1013 Hz added to the DC piezo voltage controlling one cavity mirror's position) which provides an error signal for a lock-in-amplifier. The lock-in determines the deviation from resonance and provides a compensating output signal to the piezo crystal, effectively stabilizing the cavity length to a fixed multiple of the seeding wavelength.

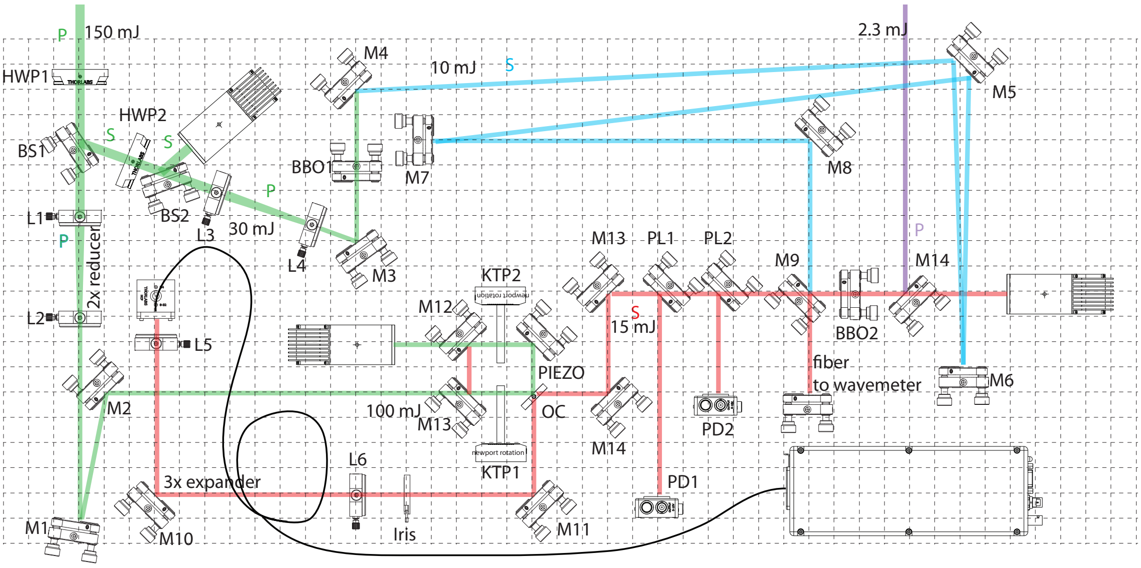

Figure 2.5: OPO laser layout for CO excitation. The 532 nm pump light (green) is split to generate 266 nm light (blue) and to pump the OPO cavity to generate 917 nm light (red). The latter are combined to produce 206 nm light (purple) for CO excitation. P and S represent the polarizations of the laser beams. [Abel12a]

2.3.2 Traps for Molecules on a Chip

The Chip and Electric Fields

Because inhomogeneous electric fields can exert forces on electric dipoles, one might trap molecules by forming a potential minimum using such fields. For hfs states this potential would be created by a maximum of electric field in all directions, for lfs states by a minimum of electric field.[2]

To trap molecules in lfs quantum states, electric field minima are created on a microchip. A design for trapping molecules on a microchip was first presented in 2008 by Meek et al. [Meek08] and only minor improvements have been made ever since. The chip consists of a glass plate with gold microelectrodes on the surface to which voltages are applied. Specifically, the electrode design consists of an array of equidistant, parallel, gold electrodes, each of which is 4 mm long, 10 µm wide and approximately 100 nm high. They are deposited onto a 1 mm thick glass plate with a center-to-center spacing of 40 µm. This structure is periodically extended over 74 mm. Each electrode is electrically connected

---

[2] A maximum of electric field in all directions is not possible [Wing84].

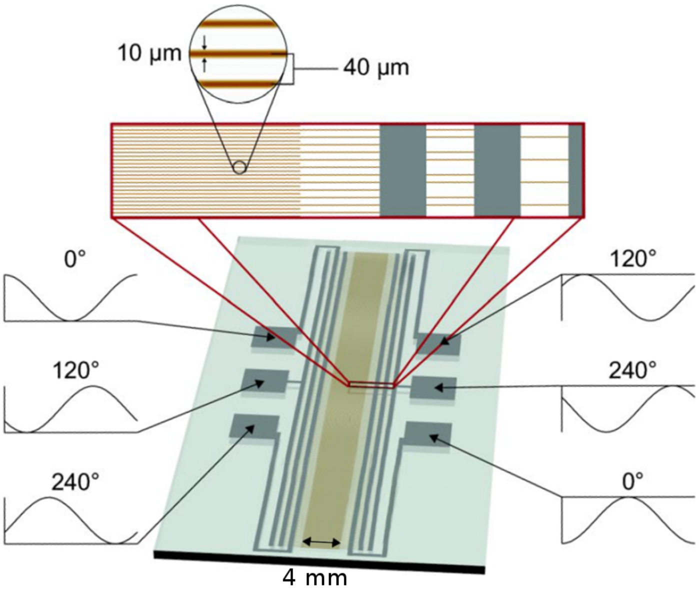

Figure 2.6: The microchip and applied voltages to the electrodes. The center region contains the 4 mm long wires creating the traps. The phase of the voltage waveform is indicated for each of the 6 pads connected to the center wires. The image is adapted from Reference [Meek08].

to the electrodes that are an integer multiple of six positions further, i.e., the electric field repeats itself every 240 μm. A picture of the chip is shown in Figure 2.6. The operation principle relies on the superposition of electric fields created by the electrodes on the chip. When two dipolar fields with different length scales and opposite directions are superimposed, a minimum of the electric field strength is created. The minimum is located at the point where the long-range dipole that dominates far from the surface is canceled by the short-range dipole that dominates close to the surface. When appropriate potentials are applied to the electrodes, these dipole fields are created and an array of tubular electric field geometries is formed. Each tube of the array has a length of 4 mm and a diameter of 20 μm, shows a minimum of electric field strength at a height of approximately 25 μm above the surface and is spaced 120 μm from its neighbors along the Z-direction. Using different sets of voltages these minima can be placed anywhere along the Z-axis. The electric field distribution of one such trap can be seen in Figure 2.7. The figure shows a cut of the trap field in the Y-Z plane using peak-to-peak voltages up to $U_{\text{Chip}} = 240$ V. From the minimum the electric field strength rises in both directions until it reaches the saddle point at 5.6 kV/cm ($Y \approx 46$ μm), determining the effective trap height.

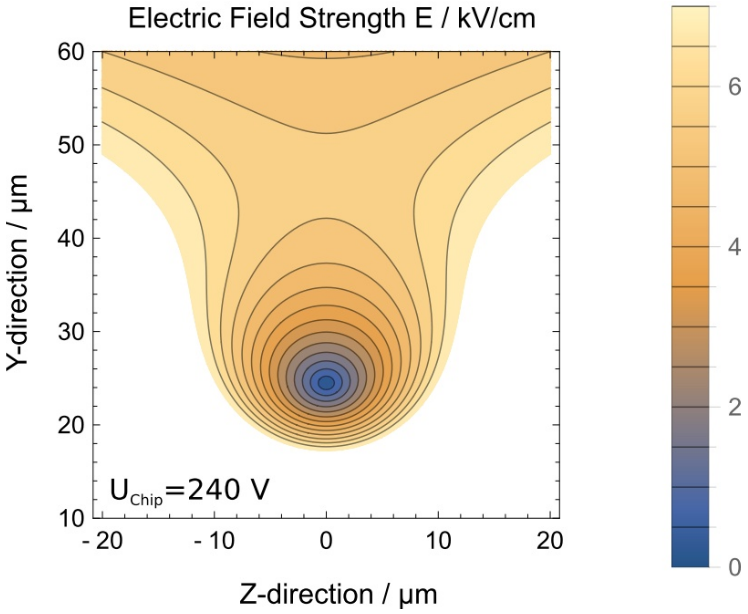

Figure 2.7: Electric field strength of one trap created above the surface of the chip. In addition to the color code, contours are indicated which start from 0.5 kV/cm and have 0.5 kV/cm spacing. The minimum has 0 kV/cm field strength, the saddle point is found at 5.6 kV/cm.

2.3.3 Microtraps for Polar Molecules

In the supersonic beam of either CO or ammonia, only the lowest few rotational levels of the vibrational and electronic ground state are populated. To achieve a reasonably deep trap for these molecules on the chip they need to be in a quantum state with a large enough Stark effect. This is achieved for ^{12}CO molecules by exciting them to the $a^3\Pi_1$ $|v = 0, J = 1, M\Omega = -1\rangle$ level. For ammonia the lowest rotational level with first order Stark effect is the $|\nu_{\text{Inv}} = 1, J = 1, K = 1\rangle$ level in the electronic ground state, which is low-field-seeking. The Stark effect is different for different isotopologues of ammonia in this quantum state though. The electric field distribution on the chip $\vec{E}_{\text{Chip}}$ together with the Stark effect with energy $\mathcal{E}_{\text{Stark}}(\vec{E}_{\text{Chip}})$ defines the trapping potential according to Equations 2.12 and 2.19. In the case for ammonia in the aforementioned quantum state, this yields:

$$\mathcal{E}_{\text{Stark}}(J = 1, MK = -1) \propto \sqrt{\left(\frac{\mathcal{E}_{\text{Inv}}}{2}\right)^2 + \left(\frac{\mu|\vec{E}_{\text{Chip}}|}{2}\right)^2}. \tag{2.22}$$

For the different isotopologues the major difference for $\mathcal{E}_{\text{Stark}}$ is in their inversion splitting $\mathcal{E}_{\text{Inv}}$. This splitting for $^{14}ND_3$ is 1.59 GHz [Fusina86], for $^{15}ND_3$ 1.43 GHz [Fusina91], and for $^{14}NH_3$ 23.7 GHz [Špirko83]. For CO, the same formula holds, but with $M\Omega = -1$ and $\mathcal{E}_{\Lambda}$ instead of $MK = -1$ and $\mathcal{E}_{\text{Inv}}$. The Λ-doublet splitting in the aforementioned state of ^{12}CO is 0.394 GHz [Field72]. With approximately 1.4–1.5 D the electric dipole moments μ of CO and the ammonia isotopologues are similar. A graphical comparison of the resulting Stark energy shift for CO and for two ammonia isotopologues are shown in Figure 2.8(a). As can be seen, the Stark energy shift for ^{12}CO and $^{14}ND_3$ are rather similar, for $^{14}NH_3$ it is relatively weak in fields up to a few kV/cm. The Stark energy curve for the $^{15}ND_3$ isotopologue lies between the ^{12}CO and $^{14}ND_3$ curve because the energy splitting lies between the value of these two (and it has the same dipole moment as $^{14}ND_3$). Since the difference in energy is anyway small between these two isotopologues, it is not shown in the figure. The effective trapping potential for this state of the $^{14}ND_3$ isotopologue as a function of Y and Z is shown in Figure 2.9.

To better visualize the different trap shapes for different species, a cut through the minimum at $Z = 0$ µm of the trapping potential is shown in Figure 2.8(b). For a peak-to-peak voltage of 240 V applied to the chip electrodes, the trap depth is approximately 87 mK for ^{12}CO, 70 mK for $^{14}ND_3$ but only approximately 8 mK for $^{14}NH_3$. Since the trapping potentials for ^{12}CO and $^{14}ND_3$ are relatively similar, also the amount of trapped molecules is expected to be similar for these two species. CO has been shown to work with the chip and with other decelerators before. Even though ammonia was never trapped on the chip before, $^{14}ND_3$ was already successfully manipulated and trapped with electric fields in various experiments [Bethlem00, Bethlem02, vanVeldhoven06, Zieger12]. $^{14}NH_3$ was also trapped [Quintero-Pérez13], even if its Stark effect is smaller. These successes clearly indicate that trapping on the chip of these ammonia isotopologues should be feasible.

Harmonicity of the Traps Figure 2.10 shows the trapping potential for ^{12}CO and $^{14}ND_3$ along lines through the electric field minimum for the highest usable voltage on the chip so far (240 V). In addition, quadratic fits to the bottom of these potentials are shown, which highlight the area where the trap can be treated as rather harmonic. In the area of approximately -4 µm $< Z <$ 4 µm and 18 µm $< Y <$ 28 µm the trap for ammonia is fairly harmonic for the given voltage of 240 V applied to the chip electrodes. For CO the area of approximately -2 µm $< Z <$ 2 µm and 23 µm $< Z <$ 26.5 µm fits well to

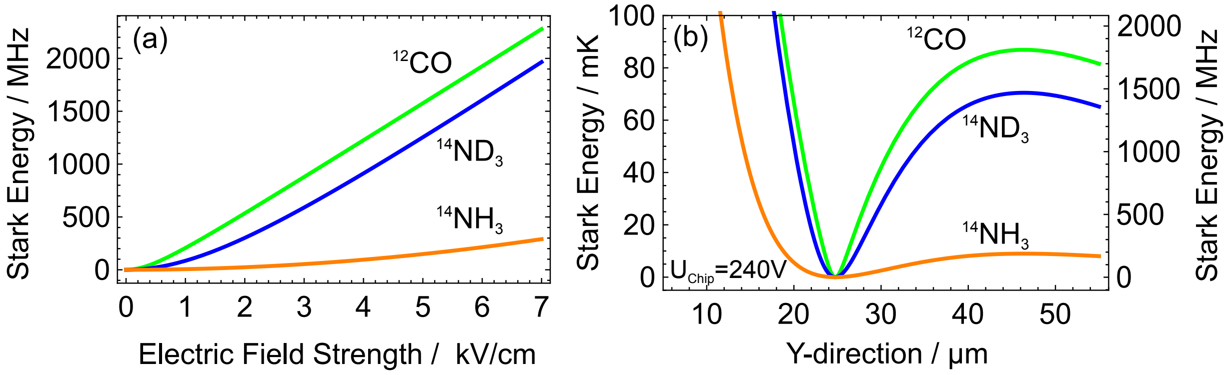

Figure 2.8: Comparison of the Stark effect and trap depths of three different molecules. (a) Stark effect of ^{12}CO $a^3\Pi_1$ $|v=0,J=1,M\Omega=-1\rangle$, ^{14}ND$_3$ and ^{14}NH$_3$ $\widetilde{X}\,|\nu_{\text{Inv}}=1,J=1,MK=-1\rangle$. (b) Cut through the trapping potential at Z =0 µm for the three species. The temperature scale is given as $\mathcal{E}_{\text{Stark}}/k_{\text{B}}$.

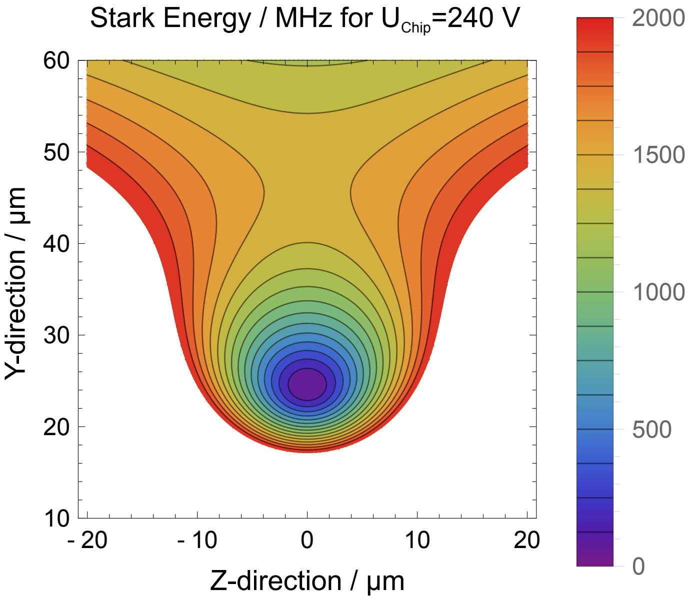

Figure 2.9: Spatial dependence of the Stark energy of ^{14}ND$_3$ molecules in the $\widetilde{X}\,|\nu_{\text{Inv}}=1,J=1,MK=-1\rangle$ state in a trap. The contours are indicated in the legend, start from 125 MHz and are separated by 125 MHz. The minimum is found at approximately Y = 25 µm with 0 MHz, the energy at the saddle point at approximately Y = 45 µm is shifted up to approximately 1468 MHz.

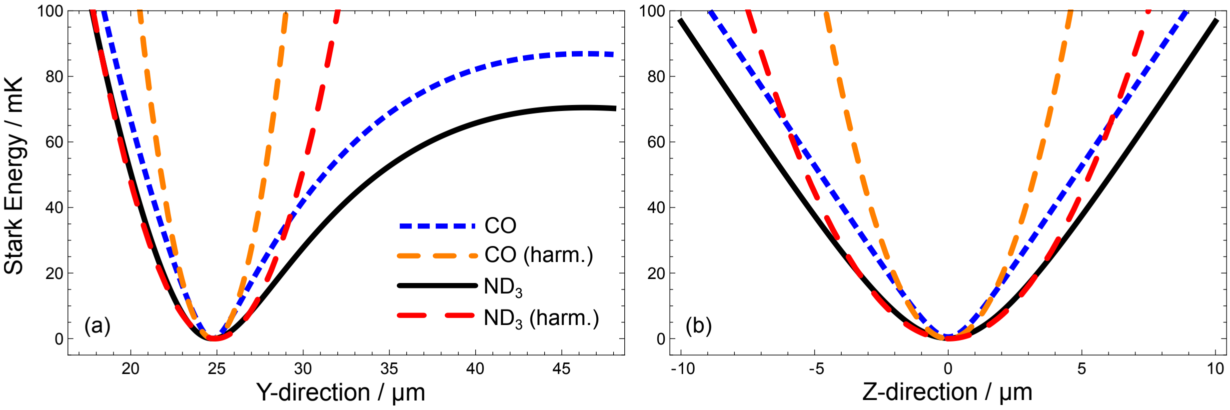

Figure 2.10: Comparison between the calculated and harmonic trapping potentials for ^{12}CO and ^{14}ND$_3$ in lfs states using 240 V waveforms. (a) Stark energy curve along the Y-direction of the trap going directly through the minimum (set to be $Z = 0$ µm). Harmonic potentials are shown which fit the region close to the minimum. Deviations occur for CO on both sides of the minimum, for ammonia only on the side of the saddle point for the shown energy range. (b) Stark energy curve for the Z-direction and through the minimum. The bottom part is fit by different harmonic potentials compared to (a).

the harmonic potential. Outside the harmonic region the trap is quite linear, except close to the saddle point. Since the electric field scales approximately linearly with distance from the minimum the larger doublet splitting in ammonia leads to a larger quadratic distance dependence of the Stark energy, thus the larger harmonic area. The threshold electric field, where the Stark energy scales rather linearly with electric field rather than quadratic is above $|\vec{E}| = \mathcal{E}_{\text{Split}}/\mu$ (μ - electric dipole moment). It is 2.1 kV/cm for ^{14}ND$_3$ and 0.56 kV/cm for ^{12}CO. For lower voltages the harmonic region is getting larger for both molecules because the threshold electric field is reached farther away from the minimum.

Guiding and Deceleration

Previously only DC voltages were considered to create and position the traps. However, these tubular traps can also be moved smoothly over the surface of the chip along the Z-direction, if the voltages applied to the electrodes are varied sinusoidally in time. Three of the six voltages remain always positive, the other three always negative. Typical peak-to-peak amplitudes of these sine waves are on the order of 200 V and reach up to 240 V. The phases of the sinusoidal voltage waveforms are shifted by ±120° relative to the neighboring two electrodes for each polarity set of voltages (positive, negative). With a period length of 120 µm, a frequency of 2.5 MHz will be needed for a trap to travel at a speed of 300 m/s. The chip is oriented such that the molecules from the supersonic beam will fly parallel over the surface but perpendicular to the microtraps. When the traps are moved at the speed of the molecular beam ($\approx$ 300 m/s) some lfs molecules with the right position and velocity can be trapped. If the traveling speed of the traps is unchanged the molecules will be guided smoothly across the surface of the chip. At the very end of the electrode region each trap rapidly opens up and releases the molecules, letting them expand ballistically. To filter out molecules that cannot be trapped at all because their position over the surface is too high(higher than the saddle point), two razor blades are installed, one at the beginning and one at the end of the chip. They allow only heights up to 70 µm over the chip surface. Lfs molecules finding themselves in between the traps or above the saddle point will experience a force away from the chip surface since the fields are getting weaker with distance from the surface. High-field-seekers will be attracted to the high fields at the surface. Non-field-seekers ($M = 0$ states) are strictly spoken weakly high-field-seeking due to higher order effects. Over the whole length of the chip the small forces they will experience will be enough to attract many of them to the chip surface as well. A few will still find their way through the exit slit and will lead to a broad background signal.

Since the velocity of traveling is controlled by the frequency, a continuous sweep towards lower frequencies will lead to smooth deceleration of trapped molecules. The minima themselves keep the same shape during the whole deceleration process. However, for a molecule captured in a trap the effective potential changes during the deceleration because in the accelerated frame of reference of the molecule a pseudo potential $U_{\text{Pseudo}} = -m \cdot a \cdot Z$ is added to the trap potential (m - mass of molecule, a - amount of acceleration, Z - longitudinal position). This pseudo potential distorts the trap seen by the molecule, lowering the trap depth and therewith the number of trapped molecules. It is even possible that the trap does not exist anymore because it opens up if a is too high. Accelerations of approximately $|a| \leq 1\ \mu\text{m}/\mu\text{s}^2 \approx 10^5 g$ can be applied. [Meek10] This makes it possible to bring molecules loaded from a supersonic beam to a standstill after a few cm of flight distance over the chip.

Amplifiers and Waveform Generation

Creating electric fields for static trapping on the chip is an easy task because the needed DC voltages of up to ±300 V can easily be generated by commercially available devices. For the traps to move with a constant velocity the voltage waveforms need to oscillate sinusoidally with a frequency in the range of 0–3 MHz, depending on the chosen velocity. Generating good voltage waveforms in this amplitude range with such frequencies (requiring slew rates up to 5 kV/µs) and driving a capacitive load of approximately 180 pF (the chip and connecting cables) is a nontrivial task though. This problem was approached before and the voltage amplifiers used are briefly described in Reference [Meek10]. Nevertheless the quality of the waveforms was bad at high voltages and frequencies because of the insufficient slew rate and the appearance of harmonics of the fundamental sine wave which distort the sinusoidal waveform. The waveforms started to get rather triangular instead of sinusoidal at higher voltages which leads to increased trap loss due to an increased jittering of the generated traps.

In a new approach better waveforms were generated using a different electronics design by taking transistors as waveform amplifiers. These amplifiers are based on a class A type design, which means that the transistors are held at their operating point for the whole time during operation by applying an offset voltage. Generally this is an energetically inefficient but well performing scheme. Due to the large thermal dissipation in this scheme the use of the chosen power transistors and power resistors would not be possible because the cooling would be insufficient. The fact that the experiments are performed in only a small fraction of time (at most 5–10 ms) during each experimental cycle of 100 ms implies that the amplifiers will be operated with at most 10% on-time, which drastically reduces the heat dissipation.

A schematic overview of the electronic design is shown in Figure 2.11. The amplifiers are basically consisting of a power MOSFET transistor in common source configuration together with a power resistor, and are designed and built by Thomas Zehentbauer of the Fritz Haber Institute's Electronics Workshop. The voltage U_1 represents the offset input voltage, which is initially generated on a computer before it is stored on an Acquitek DA8150 arbitrary waveform generator card (AWG) for output to the amplifier inputs. It provides an output signal between ±1 V, has a resolution of 12 bit and a sampling rate of 150 MS/s for each of its channels. The inputs are amplified up to 300 V peak-to-peak

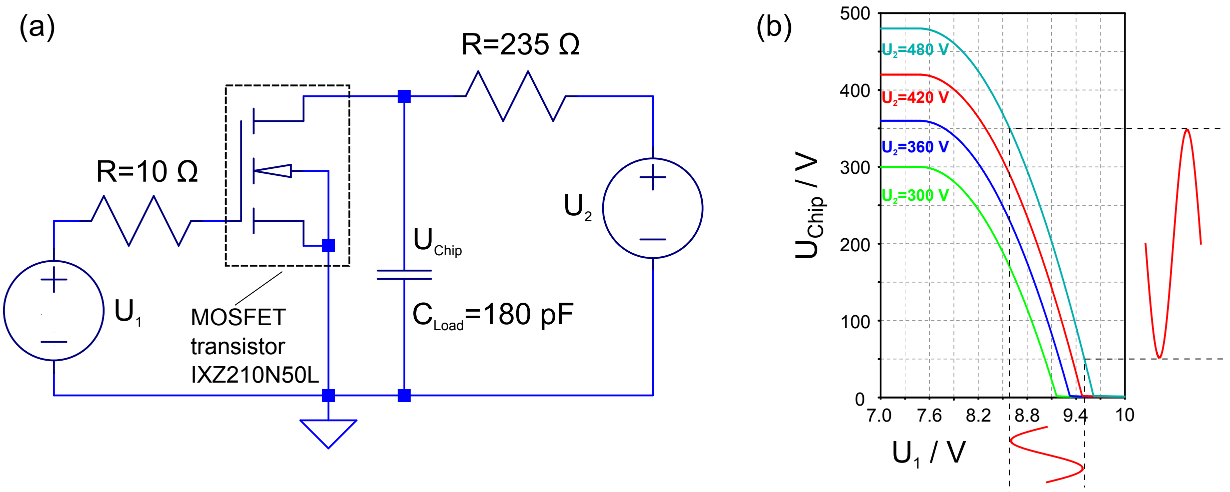

Figure 2.11: Description of the amplifiers used for generating the voltage waveforms for the chip. (a) Simplified circuit diagram of the amplifiers. (b) Relation between the output voltage U_{Chip} and the input voltage U_1 for a range of given supply voltages U_2. The chosen voltage $U_2 = 480$ V shows the largest output voltage range and is reasonably linear. The two sine waves indicate typical inputs and outputs and illustrate the amplification. The simulations in figure (b) are performed by Thomas Zehentbauer.

voltage U_{Chip} by using the supply voltage $U_2 = 480$ V. Since the output will be in the range of $50 \ldots 350$ V, it will be shifted down by -50 V to $0 \ldots 300$ V for the 3 positive channels and by -350 V to the $-300 \ldots 0$ V range for the 3 negative channels, which is not shown in the figure. The usable bandwidth lies between 0 and approximately 5 MHz for an output power drop of up to -3 dB. The harmonic distortion of the signal, due to the appearance of integer multiples of the fundamental frequency in the output signal, is an important quality criterion for the output signal because it is partially responsible for the jittering of the microtraps and in effect for trap loss. The velocity of the trap minimum due to jittering can be substantially larger than the molecular motion inside the trap (≈ 100 m/s compared to ≈ 5–10 m/s). The harmonic distortion, measured in voltage amplitude terms, is at most 1% for input frequencies of up to 3 MHz (360 m/s trap speed) and is better for lower frequencies than for higher ones. This is much better than the approximately 3–7% from the previous amplifier design [Meek11b].

Another version of these amplifiers with the same basic design has been built for the ring chip project, explained in Chapter 6. The voltage output range of this version is increased up to ±600 V for each of its 8 channels by employing a different transistor (STW9N150), but the frequency range needs to extend only up to 600 kHz to reach a trap speed of 360 m/s because the trap period is larger than for the original chip. Due to a lack of functioning ring chip samples it could not be used for experiments so far.

2.4 Detection

For the low number of neutral molecules used in the experiment to produce a measurable signal, a microchannel plate (MCP) detector is used to amplify it. For the MCP to achieve a gain in signal on the order of 10^6 to 10^7 a particle must trigger a cascade of electron emissions inside the MCP after impinging on the surface of its channels. Since a high (kinetic) energy particle is more likely to trigger such an event, accelerated ions or electrons are used which can be obtained from the molecules to be detected.

Metastable CO molecules can be detected in two ways. The first is by electron release via Auger-deexcitation [Penning27, Marbach11] at a metal or semiconductor surface, e.g. inside a channel of the MCP detector, and the second is by ionization via REMPI [Ashfold94] (resonance enhanced multi-photon ionization). The REMPI method is often the better choice primarily due to its quantum-state-selectivity and ionization efficiency. The Auger detection, with an electron release probability of approximately 1% [Meek10] at a gold surface (much less than the typical REMPI ionization probability), has the advantage that the complete arrival time distribution can be recorded in each cycle of the experiment.

The Auger method is relatively straight forward, simply letting the excited CO molecules impinge on a gold surface. The CO molecules have, due to the excitation with the UV laser, an internal energy of approximately 6 eV. One electron will be in a higher orbital than any of the occupied orbitals before excitation. This leaves a lower lying orbital unoccupied. When the CO molecules are very close to the gold surface it is possible that a conduction band electron from the gold surface tunnels into the low lying unoccupied energy level. The energy released by this process can be transferred to the excited state electron, which in turn leaves the molecule with some kinetic energy. It is also possible that the 6 eV excitation energy is transferred to the electrons in the metal. If the energy needed to promote them above the metallic ionization potential (Fermi energy less than 6 eV below ionization point) an electron can be released from there. The released electrons are transferred to an MCP with the help of static electric fields, in which they are multiplied and finally measured. This effectively allows for time-resolved detection of the molecules at the point of the detector surface.

The other possible method for detecting neutral molecules is via REMPI ionization, normally performed with a pulsed laser. The ionization occurs in several steps since the energy per photon is not enough to ionize the molecules directly by single-photon absorption. Therefore, at least two photons need to be absorbed by the molecule for ionization. This may seem like a disadvantage because the subsequent or simultaneous absorption of many photons is less likely than for single-photon absorption. The advantages of using an excitation to an intermediate state in the molecule are that the photon generation is simplified since this is easier for lower energy photons in general. Furthermore, the excitation to a particular state acts as a state selector for ionization which enables quantum state specific detection. Also, the probability of ionization is larger using subsequent absorption of photons compared to simultaneous absorption because the lifetime of the intermediate state allows for the absorption of the following photon(s) for a longer period of time. After the ionization occurred, the molecular ions are transferred to an MCP for their measurement via static electric fields, effectively generating a time-of-flight mass spectrum.

For CO, the metastable molecules are first excited with one photon of 283 nm wavelength on the $b^3\Sigma^+, v = 0 \leftarrow a^3\Pi_1, v = 0$ band. A further photon of the same wavelength (from the same laser) will subsequently ionize the molecule. This (1+1)REMPI process will leave the electron-ion system with an excess energy of approximately 0.8 eV. Details about detection methods for CO can be found in Reference [Jongma97].

The ammonia molecules are ionized via a (2+1)REMPI process directly from the ground state. A first two-photon process excites the ammonia molecules via the transition $\widetilde{B} \leftarrow \widetilde{X}$ [Ashfold88]. The subsequent absorption of a photon from the same laser ionizes the molecules. The resulting cations are measured with an MCP in the same way as the CO ions. To excite a molecule in a two-photon process, the selection rules of an electric dipole transition require that the states connected in the transition have the same parity. In this way molecules in different parity states can be ionized independently. Molecules in the lfs negative parity state in the ground state can be ionized via a rovibrational state $\nu_2 = 5$ with negative parity of the electronically excited $\widetilde{B}$ state. The transition scheme is

$$^{14}\mathrm{ND}_3 \left|\widetilde{X}, \nu_{\mathrm{Inv}} = 1, J = 1, K = 1, (-)\right\rangle \rightarrow \left|\widetilde{B}, \nu_2' = 5, J' = 3, K' = 2, (-)\right\rangle \rightarrow {}^{14}\mathrm{ND}_3^+.$$

REMPI Laser Setup

To generate the UV photons for REMPI detection an Nd:YAG laser at 532 nm (Innolas Spitlight 1200, 300 mJ per pulse, 5 ns long) pumps a dye laser (Radiant Dyes NarrowScan). The dye laser produces 566 nm light using Rhodamine 6G dye, which gets frequency doubled to 283 nm and focused with a 30 cm lens for CO REMPI. For ammonia a 317 nm beam is created in the same way as compared to CO, but using DCM Special dye. The beam gets focused with a 15 cm focal length lens because the (2+1)REMPI process can only be saturated with a higher fluence. Both outputs have an energy of approximately 10 mJ per pulse, are 5 ns long and have a bandwidth on the order of 0.1 cm^{-1}. The narrow bandwidth and high fluence of the focused beams allow for efficient quantum state specific detection.

2.4.1 Ammonia Detection Setup

Time-of-Flight Setup

The REMPI method efficiently ionizes molecules and the detection of these ions is relatively straightforward, which makes this detection method well suited for the detection of neutral molecules. However, because on the chip only a few molecules are trapped, to obtain a high amount of signal it is important to detect as many of them as possible. To achieve this the detection setup needs to account for several constraints.

First, since the density of the molecules is decreased the farther the molecules fly freely after the chip, measurements should be performed as close as possible to its end. Therefore, the TOF plates creating the electric field for extracting the ions were moved as close as possible to this position.

Second, the trap geometry confines the molecules to a thin plane above the chip, being only approximately 20 µm in height in the direction perpendicular to the chip surface. In this direction the size of the laser beam only needs to be on this order of magnitude. This is achieved with an $f = +15$ cm UV fused silica lens. Given the beam size at the lens and assuming it to be Gaussian, the focus should be on the order of 10 µm FWHM. In practice, the beam is not perfectly Gaussian and the focus should be slightly larger, fitting the size of the traps relatively well. The minimum detection distance is 6 mm from the end of the chip making it possible to ionize the molecules approximately 20 µs after leaving the traps

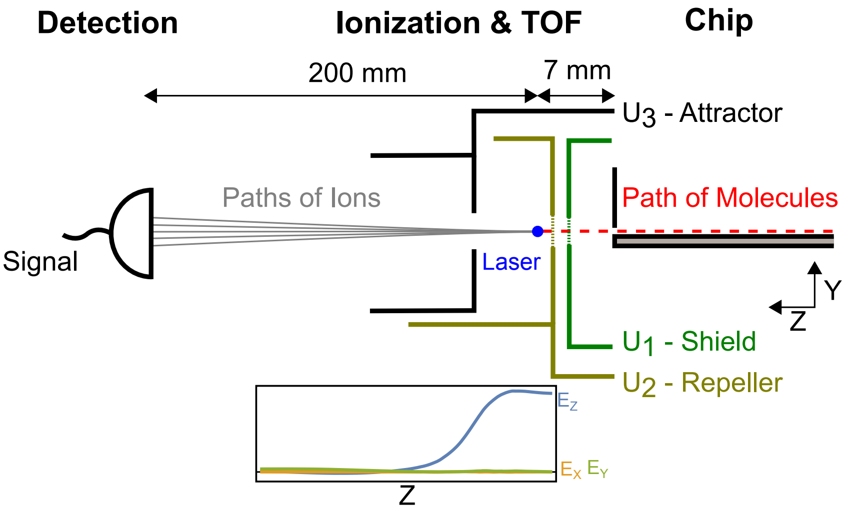

Figure 2.12: Drawing of the TOF setup to detect ammonia molecules. The molecules are flying over the chip surface from the right and pass through the first two plates of this TOF setup ($U_1 = 0$ V, $U_2 = +300$ V, but the exact voltage is not critical). A UV laser, indicated by a blue spot, ionizes the molecules. The ions are accelerated towards the attractor plate ($U_3 = 0$ V) and the MCP detector. The distance to the detector is not drawn to scale. Electric fields are indicated under the setup.

at a typical guiding velocity of 300 m/s. The molecule cloud expands only several tens of µm in 20 µs, giving still a good geometrical match with the ionizing laser. Since the size of the beam is on the order of the size of one trap, the number of molecules measured per cycle will be on the order of the number of molecules per trap, which is about 10 molecules, given a typical number density of 10^7 cm^{-3}.

Third, the first two-photon step in the (2+1)REMPI of ammonia is relatively inefficient compared to a single-photon transition. To achieve a high ionization efficiency a high fluence (laser energy per area) must be achieved, which is obtained using the focusing lens.

To get a homogeneous field distribution in the TOF zone as well as to be able to measure close to the chip, the holes in the TOF plates close to the chip are covered with a wire mesh. The more homogeneous electric field distribution with the meshes comes at the disadvantage that it reduces the number of molecules which will enter the TOF zone and, therefore, at the disadvantage of a slightly reduced signal.

A drawing of the TOF detector is shown in Figure 2.12. Molecules fly over the surface of the chip from right to left and exit through the slit at its end. After a short flight of 6 mm the molecules will be found between the TOF repeller and attractor plates. The laser is positioned very close after the repeller, only approximately 1 mm behind it, to ionize the molecules as early as possible after the chip. The electric field the ions experience points along the positive Z-direction, accelerating the ions towards the MCP detector. In the figure this electric field is indicated under the plates. The Z-component of the electric field is basically constant in the beginning, leading to a constant push on the ions away from the repeller. The field and with it the force on the ions is getting lower towards the attractor and goes almost to zero quickly after the plates. There the ions will drift towards the detector, positioned approximately 200 mm behind from the point of ionization.

Time-of-Flight Profile

The arrival time of an ion in a TOF setup is determined by the quick acceleration of the ion in the electric field and the subsequent drift towards the detector over a length d. Its electric potential energy qU (q - charge, U - electric potential) is converted to kinetic energy. Assuming that the sum of the kinetic and electric potential energy is conserved for the ion during its flight, $\frac{m}{2}v^2 + qU =$ constant holds. Since the initial kinetic energy is much lower than the electric potential energy it can be ignored. Also because the drift time is much longer than the acceleration time, $t \approx d/v$, and the flight time t is given by

$$t = \frac{d}{\sqrt{2U}}\sqrt{\frac{m}{q}}, \tag{2.23}$$

which is on the order of a few µs for light, singly charged ions and a potential on the order of a few 100 V. The signal directly obtained from an ammonia molecular beam is a time-of-flight profile which is shown in Figure 2.13. The TOF profile contains signals from all produced positive ions at various mass-to-charge ratios $\frac{m}{q}$. The information about $^{14}\mathrm{ND}_3^+$ molecules can be extracted at $\frac{m}{q} = +20\ \frac{\mathrm{amu}}{e}$ independently by gating the signal trace around this value. This trace contains only two large peaks. The first peak at time zero is produced from stray light of the laser during ionization, the second peak at 5.3 µs after ionization originates from ionized ammonia molecules. There are also very small peaks present at different masses, as there might accidentally also be other species or fragments present.

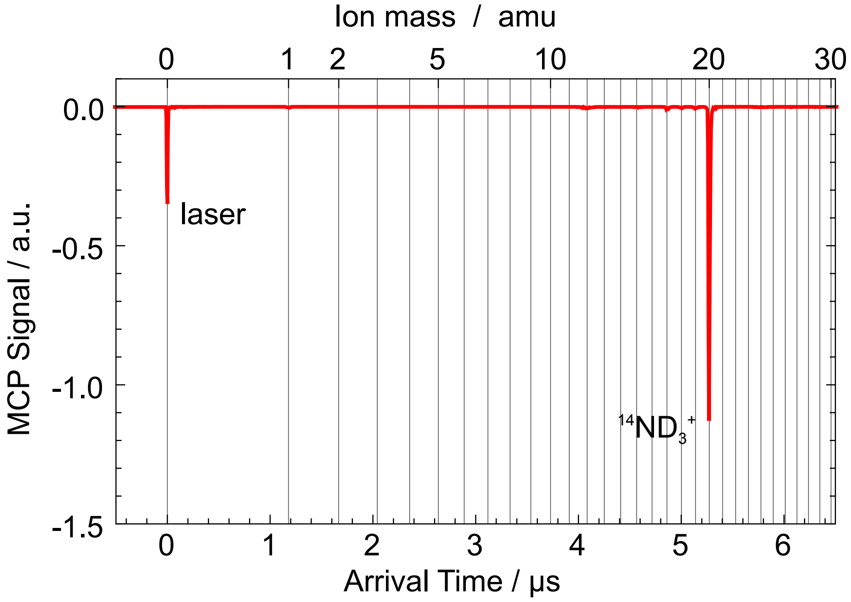

Figure 2.13: MCP signal using the TOF setup. The signal is negative because the MCP generates an electron signal. The ion mass scale assumes that only single ionization occurs.

2.5 Trajectory Simulations

To predict and validate the outcome of the experiments it is helpful to simulate the molecular motion before, on and after the chip. Basically this has been done already by S. Meek [Meek10] and the simulations that are performed use his software with only minor modifications.

The simulation is split in three regions. A region from the laser excitation (CO) to the entrance of the chip, the region of the traps over the chip and the region after the chip until detection. Due to the extreme aspect ratio of the traps the molecules experience almost no force along the X-direction in the trap. In this case a two-dimensional simulation is sufficient to cover the relevant details of the distribution of the molecular cloud. In the first region an initial set of molecules is generated with the size of the laser spot and a Gaussian velocity distribution. Since in free space the molecules fly in straight lines this set can easily be propagated to the entrance of the chip. Molecules that do not fly over the chip surface within the trap region (up to 50 µm over the surface) are discarded from the simulation. In the second region the molecules will be manipulated by the electric fields above the chip. To simulate the molecular trajectories it is necessary to solve the equations of motion for each molecule step by step in time. In this two-dimensional calculation these equations are a set of four differential equations

$$\begin{aligned} \frac{dv_Y}{dt} &= \frac{1}{m}F_Y(Y,Z,t) \\ \frac{dv_Z}{dt} &= \frac{1}{m}F_Z(Y,Z,t) \\ \frac{dY}{dt} &= v_Y \\ \frac{dZ}{dt} &= v_Z. \end{aligned} \tag{2.24}$$

The force on the molecules $\vec{F}$ is calculated from the mechanical potential they experience in the trap $U(Y,Z)$ as $\vec{F} = -\vec{\nabla}U(Y,Z)$ where $U(Y,Z) = U(|\vec{E}(Y,Z)|)$ is assumed to depend only on the magnitude of the electric field. The mechanical potential is known from the Stark effect to be

$$U(|\vec{E}(Y,Z)|) = \sqrt{\left(\frac{\mathcal{E}_{\text{Split}}}{2}\right)^2 + \left(\mu_{\text{eff}}|\vec{E}(Y,Z)|\right)^2}. \tag{2.25}$$

For molecules in lfs states and the force $\vec{F}$ is given by

$$\vec{F} = -\frac{\mu_{\text{eff}}^2|\vec{E}(Y,Z)|\vec{\nabla}|\vec{E}(Y,Z)|}{\sqrt{\left(\frac{\mathcal{E}_{\text{Split}}}{2}\right)^2 + \left(\mu_{\text{eff}}|\vec{E}(Y,Z)|\right)^2}}, \tag{2.26}$$

with the effective electric dipole moment for the individual quantum state $\mu_{\text{eff}} = \mu \cdot MK/J(J+1)$. Given the electric field distribution over the chip the force can be calculated and with the initial values $Y(t_0)$, $Z(t_0)$, $v_Y(t_0)$, and $v_Z(t_0)$ from each molecule, the positions and velocities can be determined at $t_0 + \Delta t$, using an approximation algorithm (the Runge-Kutta method in this case). Repeating this process many times propagates the molecules from the entrance to the exit of the chip. In the last region, after the chip, the molecules experience again no force and will be freely propagated to the detector's position. More details about the simulation can be found in [Meek10].

CHAPTER 3

Vibrational Excitation on a Chip

3.1 Introduction

Molecules on a chip can be coupled to photons over a wider range of frequencies than atoms. The fundamental molecular vibrational modes can be addressed with mid-infrared photons (wavelengths between 3–50 µm), which is why this spectral range is often referred to as the molecular fingerprint region. For example, with organic molecules, a mid-infrared spectrum of an unknown substance might allow the identification of a specific functional group present in the molecule, like O−H, C−H or C−O, C=N or more complex units. The vibrational overtones and combination modes extend into the near-infrared range, with wavelengths in the 0.78–3 µm range.

It was already demonstrated that transitions between adjacent *rotational* levels within a given electronic and vibrational state can be induced above the chip. These transitions were driven with high efficiency using a coherent, narrowband continuous-wave source of radiation with a wavelength of approximately 1.5 mm [Santambrogio11]. However, the frequency shift of the rotational transition for trapped molecules on the chip due to the Stark effect (≈GHz) is much larger than the bandwidth of typical mm-wave sources (≈Hz).

Adapted from:

Vibrationally exciting molecules trapped on a microchip
Mark J. Abel, Silvio Marx, Gerard Meijer and Gabriele Santambrogio
Molecular Physics **110**(15-16):1829 (2012)

Therefore, to address all molecules in the trap, the traps had to be switched off during the excitation.

Vibrational transitions, which are the subject of this chapter, behave differently in an electric field. Vibrational transition frequencies are relatively less sensitive to electric fields, because the energy splitting between them is much larger compared to the rotational levels. Often, transitions can be made between levels that have a similar shift in electric fields, thereby diminishing the Stark broadening. Furthermore, mid-IR radiation is easily obtainable with pulsed lasers and the typical line-widths are on the order of a few GHz. This leads to a much better match between the inhomogeneous broadening of IR transitions in trapped molecules and the laser bandwidth. Thus, molecules can be vibrationally pumped with no need for switching off the trapping fields. Being able to induce such a transition to another internal quantum state in the molecule on the chip is particularly interesting when the molecule remains trapped in the final state as well. Otherwise further manipulation or detection of these molecules would be difficult.

In this chapter, the experimental setup used to excite the vibrational transition $v = 1 \leftarrow v = 0$ in trapped $^{12}C^{16}O$ molecules is presented. In the experiments, the molecules are prepared with a pulsed laser in a single rotational level ($J = 1$) of their first electronically excited, metastable state ($a^3\Pi_1$). Then, the transition is performed using an infrared laser of approximately 5.9 µm wavelength, where molecules are pumped from the $v = 0$ state to selected rotational levels of the vibrationally excited $v = 1$ state. Finally, the molecules are ejected from the chip and fly towards the ionization zone, where they are state-selectively detected using another pulsed laser system.

To characterize the vibrational transitions, IR Stark spectroscopy is initially performed on the free molecular beam. For this purpose, the chip is replaced by a pair of metal plates, which are used to create a tunable and well-defined electric field in the region where the vibrational transitions are induced. A discussion follows about the IR excitation of CO molecules in the miniaturized electric field traps, where the molecules are exposed to an inhomogeneous, rotating electric field. Then, experiments are described in which the pulsed IR radiation interacts with the metastable CO molecules while these are trapped on the chip.

These experiments demonstrate that the pulsed IR radiation can be coupled onto the chip without damaging the chip and that the CO molecules, guided in moving electric field traps to the center of the chip while in the $a^3\Pi_1$ $v = 0$ state, can be pumped to the $v = 1$

state. The vibrationally excited molecules remain trapped in the miniaturized electric field traps, are transported to the end of the chip, will subsequently be detected and the data is analyzed.

3.2 Experimental Setup

The general setup has already been described in Section 2.3. The experimental setup specific to these experiments is shown schematically in Figure 3.1. The experiments start by allowing a mixture of 20% CO in Kr, cooled to 140 K, to expand into vacuum through a pulsed solenoid valve. The expansion is skimmed to form a collimated beam with a mean velocity of 330 m/s which is intersected at right angles by a 206 nm laser pulse exciting the molecules from the ground electronic state to the lowest vibrational level of the lowest metastable triplet electronic state, $a^3\Pi$, as shown in Figure 3.2. The metastable molecules are trapped over the surface of the chip and are guided to its end. In the middle of the chip, the trapped molecules can be excited by an infrared laser to promote them from the $v = 0$ to the $v = 1$ vibrational level. A 190-Gauss offset magnetic field (generated with permanent magnets and pointed along the chip surface in the X-direction) is used to induce a small Zeeman splitting at zero electric field, to suppress nonadiabatic transitions to non-trappable states. [Meek11b] After manipulation on the chip the molecules are detected by ionizing them quantum state-selectively using a UV laser and by counting the ions with an MCP at the end of a TOF mass spectrometer.

IR Laser Setup

The major difference to the general setup, which has been described in Section 2.3, is the use of a tunable, pulsed infrared laser (200 µJ pulses with 4 ns duration and 2.5 GHz bandwidth, Sirah Laser- und Plasmatechnik GmbH). This radiation is created by first generating the difference frequency between the output of a nanosecond dye laser (bandwidth 1.5 GHz and approximately 750 nm wavelength) and part of the fundamental of an injection-seeded Nd:YAG laser (approximately 1064 nm) using a $LiNbO_3$ crystal. This narrowband difference frequency light, with a wavelength of 2.6 µm, is parametrically amplified by a second portion of the Nd:YAG fundamental in a second $LiNbO_3$ crystal, giving rise to 1.8 µm and 2.6 µm beams. Finally, these signal and idler waves are mixed in a $AgGaSe_2$ crystal to generate their difference frequency around the desired 5.9 µm for the

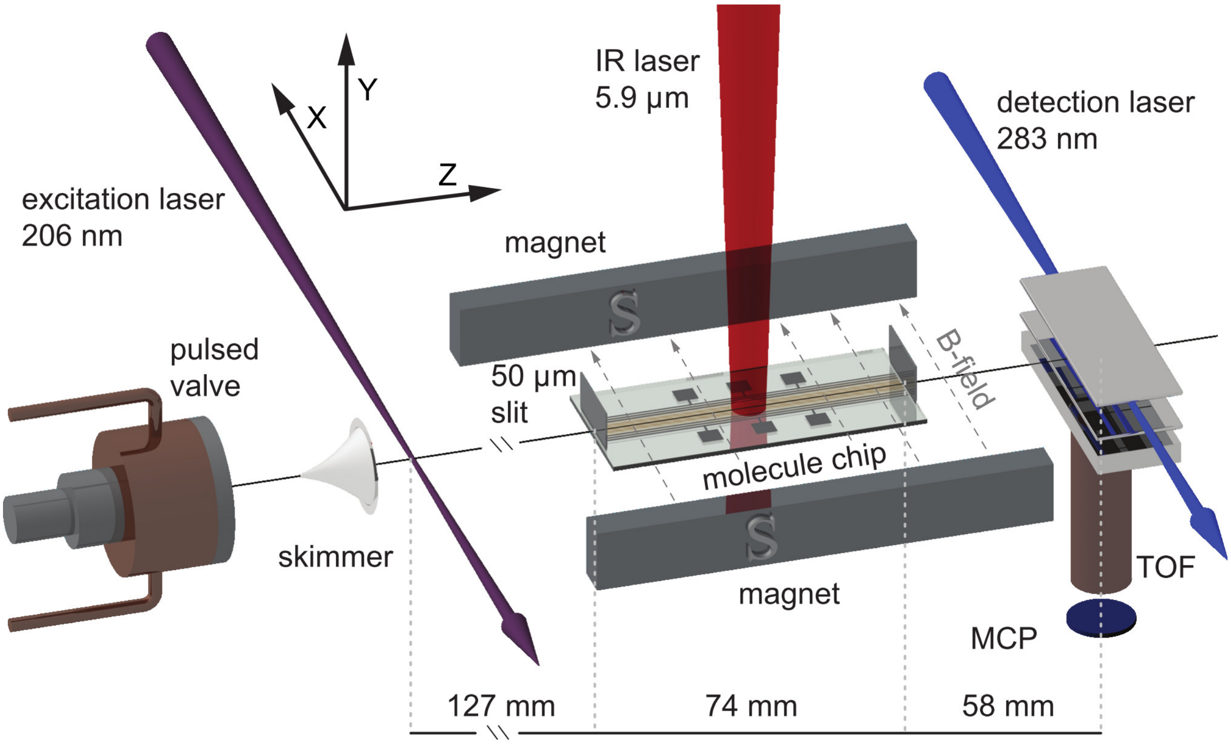

Figure 3.1: Molecular beam machine. After a skimmer, a beam of CO molecules is prepared in selected rotational levels of the $a^3\Pi_1$ $v = 0$ state using 206 nm radiation. The molecules fly 127 mm to the chip entrance. If they pass through a 50 µm slit and above the molecule chip, they can be trapped in electric field minima. In the center of the 74 mm long chip, they can be vibrationally excited by an infrared laser with a wavelength near 5.9 µm. After being ejected from the chip, the molecules fly 58 mm to a time-of-flight (TOF) detector where they are state-selectively ionized and detected. A 190-Gauss magnetic field prevents nonadiabatic losses from the traps.

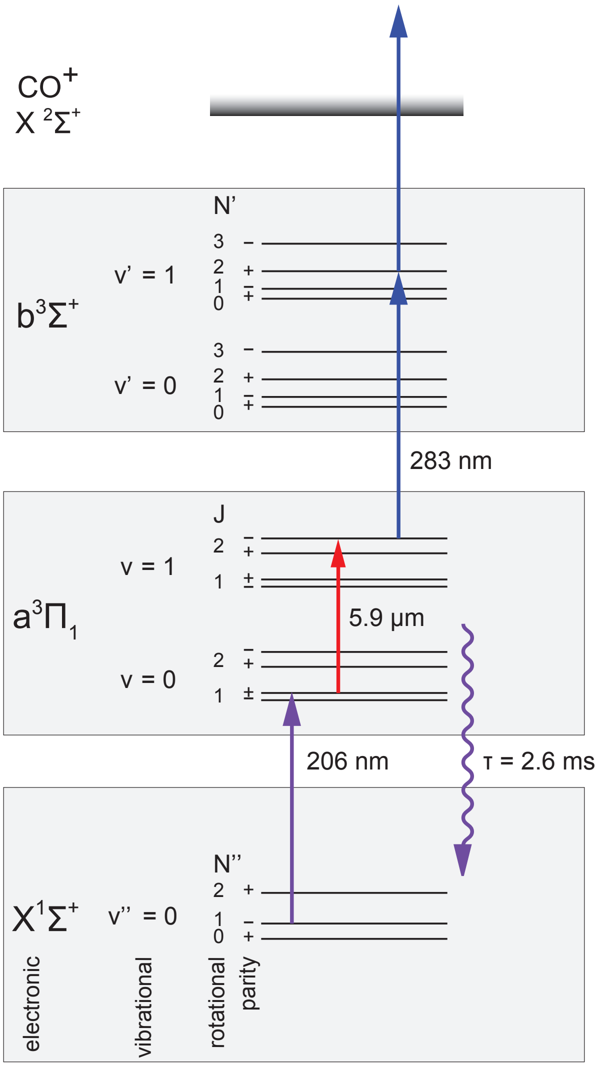

Figure 3.2: Partial energy level scheme of CO. Molecules are pumped with 206 nm radiation from the ground electronic state ($X^1\Sigma^+$) to the upper Λ-doublet component in the $v = 0$, $J = 1$ level of the lowest-lying triplet state $a^3\Pi_1$. Either the $J = 1$ or the $J = 2$ Λ-doublet can be selectively accessed in this way. Molecules in the $v = 0$, $J = 1$ levels are excited by mid-IR light near 5.9 µm to the $v = 1$ level. The $v = 0$ or 1 vibrational levels in the $a^3\Pi_1$ state can be state-selectively ionized in a two-photon process via the $v = 0$ or 1 levels, respectively, in the $b^3\Sigma^+$ state. One possible vibrational excitation (5.9 µm) and one possible REMPI transition (283 nm) for detection, originating from the $v = 1$, $J = 2$ level of the $a^3\Pi_1$ state, is indicated.

excitation of the C-O stretch vibrational mode. [Gerhards04] Long-duration frequency stability of the mid-infrared output requires that the seeder frequency of the Nd:YAG laser is stabilized, for which a molecular iodine reference and a feedback loop with an approximately 1 second response time is used. Also, the 2.5 GHz linewidth that is measured is an average over typically a few thousand of laser shots. The width therefore reflects not only the inevitable spectral broadening and temporal narrowing accompanying nonlinear conversion, but also the variation of the dye laser output wavelength from shot to shot. This wavelength fluctuates randomly, switching between about three longitudinal modes of the dye laser resonator. To achieve a significantly narrower linewidth it would be necessary to either insert a tunable etalon into the laser oscillator, or to seed the dye amplifier with CW light. Neither of these approaches were attempted; in fact, as will be seen below, the bandwith of 2.5 GHz is close to an optimal value for the experiments describe here. The spot of the IR beam on the chip is more or less round, with 2 mm diameter (FWHM).

3.3 IR Stark Spectroscopy of CO in the $a^3\Pi_1$ State

To test the IR laser setup and to understand the interaction of the laser with the trapped molecules, spectroscopy experiments were performed and were compared to numerical simulations of these experiments.

Energy Levels and Transitions

For rovibrational excitations with the IR laser certain selection rules [Davies90] need to be obeyed. For vibrational transitions in a harmonic potential $\Delta v = \pm 1$, so only the $v = 1$ level can be readily accessed. Only transitions in the $\Omega = 1$ ($\Delta\Omega = 0$) spin-orbit manifold are considered. Furthermore, electric dipole selection rules allow $\Delta J = 0, \pm 1$ and $\Delta M = 0, \pm 1$. Since in the $\Omega = 1$ manifold the lowest level is the $J = 1$ level, only two rovibrational transitions are allowed from the CO $a^3\Pi_1$, $v = 0$, $J = 1$ level. These are the transitions to the $J = 1$ (Q-branch) and $J = 2$ (R-branch) levels in the excited $v = 1$ level, with frequencies of 1714 cm^{-1} and 1721 cm^{-1}, see References [Davies90, Field72]. The parity selection rule implies that the parity must change in one-photon transitions at zero electric field ($+ \rightarrow -$ and $- \rightarrow +$).

The rotational states split into different substates when an electric field is applied. This Stark splitting originates mainly from mixing between the closely spaced, opposite-parity components of the same Λ-doublet. The electric-field-dependent energies of these Λ-doublet levels can be described by

$$\mathcal{E}_{\text{Stark}}(|\vec{E}|) = \pm\sqrt{\left(\frac{\mathcal{E}_\Lambda}{2}\right)^2 + \left(\mu|\vec{E}|\frac{M\Omega}{J(J+1)}\right)^2}, \tag{3.1}$$

given by Equation 2.12 in Subsection 2.2.1. In this equation, $\mathcal{E}_\Lambda$ is the magnitude of the Λ-doublet splitting, which for the two lowest energy $J = 1$ levels is 394 MHz ($v = 0$) and 385 MHz ($v = 1$), and for the $J = 2$ levels it is 1151 MHz ($v = 0$) and 1125 MHz ($v = 1$) [Wicke72]). The factor $\mu M\Omega/J(J+1)$ is the magnitude of the projection of the body-fixed dipole moment $\mu = 1.375$ Debye [Wicke72] on the electric field, $\vec{E}$.

The Stark curves calculated using Equation 3.1 for electric field strengths from 0 to 20 kV/cm are shown on the right in Figure 3.3(a). As already mentioned, after excitation by the 206 nm laser only the upper Λ-doublet component with positive parity of the $v = 0$, $J = 1$ level is populated. Due to the parity selection rule, molecules excited in a Q-branch transition ($\Delta J = 0$) always end in the lower Λ-doublet component of the $v = 1$, $J = 1$ state with negative parity. By contrast, in R-branch transitions ($\Delta J = +1$) at zero field, only transitions to the upper component of the $v = 1$, $J = 2$ Λ-doublet are allowed (negative parity).

As the external electric field increases, the parity of the eigenstates progressively mixes and M ceases to be a good quantum number. When the dipole term dominates the Λ-doubling term in Equation 3.1, the parity of the eigenstates is totally mixed and both Λ-doublet components can be reached during vibrational excitation. In such a strong field, the product $M\Omega$ is well-defined for each eigenstate. Note that parity and M are always well-defined for the $M = 0$ levels because to first order they experience no Stark effect.

The vertical arrows in Figure 3.3(a) show the allowed transitions when the infrared laser polarization is either parallel or perpendicular to the applied electric field, and correspond to the experimental situation in which only the upper component of the Λ-doublet of the $v = 0$, $J = 1$ level is populated. When the laser polarization and applied electric field are parallel, transitions with $\Delta M = 0$ are allowed, whereas when the polarization and field are perpendicular the laser drives $\Delta M = \pm 1$ transitions. The two cases are achieved by rotating the laser polarization relative to the fixed field. Also shown are the allowed transitions in the field-free case.

To test the infrared laser setup and to observe the actual electric field dependence of

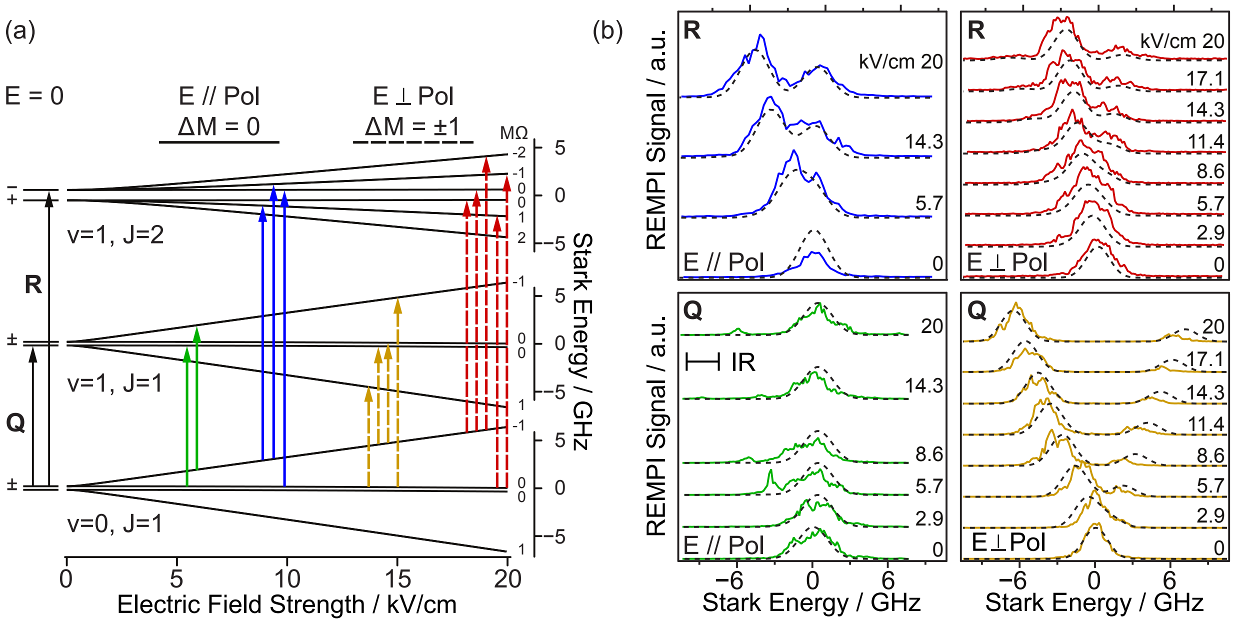

Figure 3.3: Stark shifted rotational states in the ^{12}CO $a^3\Pi_1$ $v = 0$ and $v = 1$ manifolds. (a) Calculated Stark curves for all the components of $v = 0$, $J = 1$ and $v = 1$, $J = 1$ and 2 states. The arrows indicate allowed transitions in the Q- and R-branches when the laser polarization is either parallel (solid) or perpendicular (dashed) to a strong applied electric field. On the left-hand side are the field-free energy levels and transitions, while on the right-hand side the quantum numbers of the mixed eigenstates are given. (b) Four series of Stark spectra for increasing electric field, the same four cases as indicated with arrows in (a). In these spectra, the solid curves are the measured data and the dashed curves are the simulation. The solid line labeled IR indicates the infrared laser's bandwidth of 2.5 GHz (FWHM).

the (ro-)vibrational transitions, Stark spectroscopy experiments were performed. For spectroscopy, the setup is changed by removing the chip from the vacuum chamber and installing a pair of metal plates, which allow the creation of a homogeneous electric field. The infrared excitation of the CO molecules in the free molecular beam is then carried out by scanning the laser's frequency for different electric fields. For detection, ionization through the $b^3\Sigma^+$, $v = 1$, $N' = 2 \leftarrow a^3\Pi_1$, $v = 1$, $J = 1$ or 2 state is used to probe the population after Q- or R-branch excitation, respectively. The linewidth of the ionizing laser is less than one wavenumber, sufficient to resolve individual rotational transitions. For further information about the REMPI detection see Section 2.4. The resulting absorption spectra are shown in Figure 3.3 (b) for the cases of the IR light polarized parallel and perpendicular to the applied field, and for field strengths between 0 and 20 kV/cm. The overlap between the absorption lines in any of the four cases up to 5 kV/cm and the IR laser's bandwidth (the solid line labeled IR) is large. Since 5 kV/cm is the highest field strength in the traps, this indicates that for all cases most of the trapped molecules can be addressed with the laser and promoted to either the $v = 1$, $J = 1$ or the $v = 1$, $J = 2$ levels, although possibly with a different intensity than that observed in the situation of a homogeneous field. Only for higher electric fields the shifts exceed the bandwidth significantly and the excitation would no longer be guaranteed.

Simulation of the Stark Spectra

To simulate the Stark spectra for the $v = 1 \leftarrow v = 0$ transition, a Hamiltonian describing the initial and final state energies needs to be set up and diagonalized. From the resulting energy levels the energy differences for the particular transition can then be determined as a function of electric field and compared to the measurements. Since all transitions are carried out in the same electronic state, its energy contribution can be omitted. Since the vibrational part of the Hamiltonian leads to a constant offset in all spectra, it is omitted as well. Then, the rotational contribution to the Hamiltonian and the Stark interaction play the dominant role for calculating the spectra. The Hamiltonian

$$\hat{\mathcal{H}} = \hat{\mathcal{H}}_{\mathrm{SO}} + \hat{\mathcal{H}}_{\mathrm{SS}} + \hat{\mathcal{H}}_{\mathrm{NR}} + \hat{\mathcal{H}}_{\mathrm{SOCD}} + \hat{\mathcal{H}}_{\Lambda} - \vec{\mu} \cdot \vec{E} \tag{3.2}$$

is used to describe the energy levels of the molecule in an electric field $\vec{E}$ for each vibrational level. It contains the Stark Hamiltonian but has also contributions from interactions like spin-orbit(SO), spin-spin(SS), nuclear-rotation(NR), centrifugal distortion(SOCD) and lambda doubling (Λ). For further information about the individual contributions see References [Brown03, Meek10] This Hamiltonian is then diagonalized for each electric field strength used in the measurement to obtain the energy eigenvalues of the individual quantum states. To obtain the frequency of the possible transitions, the difference in energy of the final to the initial state is calculated. The eigenfunctions of $\hat{\mathcal{H}}$,

$$|\Phi\rangle = |J, \Omega, M\rangle \tag{3.3}$$

are used to determine the relative intensity of a transition I_{fi}. To a good approximation $I_{\text{fi}} \propto S_{\text{fi}}$, the line strength of a transition, which can be calculated for an electric dipole transition as

$$S_{\text{fi}} = \sum_{\Phi', \Phi''} \sum_{A=X,Y,Z} \left| \langle \Phi' | \, \hat{\mu}_A \, | \Phi'' \rangle \right|^2 . \tag{3.4}$$

The functions Φ' and Φ'' are the eigenfunctions corresponding to the eigenenergies $\mathcal{E}'$ (final) and $\mathcal{E}''$ (initial), respectively. The summation over them takes into account possible degeneracies. Operator $\hat{\mu}_A$ is the transition dipole moment component in the space-fixed frame. The matrix elements $\langle \Phi' | \, \hat{\mu}_A \, | \Phi'' \rangle$ according to Reference [Bunker06] are given by

$$\begin{aligned} \langle J', \Omega', M' | \, \hat{\mu}_Z \, | J'', \Omega'', M'' \rangle = & \mu (-1)^{M' - \Omega'} \sqrt{(2J''+1)(2J'+1)} \times \\ & \begin{pmatrix} J'' & 1 & J' \\ -\Omega'' & 0 & \Omega' \end{pmatrix} \begin{pmatrix} J'' & 1 & J' \\ -M'' & 0 & M' \end{pmatrix} \end{aligned} \tag{3.5}$$

and

$$\begin{aligned} \langle J', \Omega', M' | \, \hat{\mu}_X \, | J'', \Omega'', M'' \rangle = & \frac{\mu}{\sqrt{2}} \sqrt{(2J''+1)(2J'+1)} \begin{pmatrix} J'' & 1 & J' \\ -\Omega'' & 0 & \Omega' \end{pmatrix} \times \\ & \left[(-1)^{M' - \Omega' - 1} \begin{pmatrix} J'' & 1 & J' \\ -M'' & 1 & M' \end{pmatrix} - \right. \\ & \left. (-1)^{M' - \Omega' + 1} \begin{pmatrix} J'' & 1 & J' \\ -M'' & -1 & M' \end{pmatrix} \right] \end{aligned} \tag{3.6}$$

These matrix elements can directly be evaluated numerically. Here, the Z-component of μ is considered to be parallel to the static electric field $\vec{E}$. As has been said before, when the laser polarization is parallel to Z, $\Delta M = 0$ transitions can be driven. This can be seen from the fact that the sum of a 3-J-symbol's lower row must vanish in order for the 3-J-symbol to be nonzero. On the other hand, the X-component is perpendicular to the electric field. When the laser polarization is parallel to X (perpendicular to Z), $\Delta M = \pm 1$ transitions can be driven.[1] The component $\hat{\mu}_Y$ does not need to be taken into account because the laser propagates along the negative Y-direction, so there is no field component to drive transitions along $Y (\hat{\mu}_Y \cdot E_{\mathrm{IR},Y} = 0)$. For the calculation it is assumed that the initial state is the $v = 0$, $\Omega = 1$, $J'' = 1$, $M'' = \{0, -1\}$, which are the states of the upper Λ-doublet component. The resulting "stick spectra" are convolved with a Gaussian function of 2.5 GHz width, corresponding to the experimentally measured linewidth of the IR laser.

The calculated frequencies and intensities of the resonances are in good agreement with the measurements, whose major limitation is the uncertainty in the purity of the laser polarization and thereby in the direction of the laser polarization with respect to the electric field. This will lead to contributions in the spectra from nominally forbidden transitions; these contributions are particularly evident in the Q-branch spectra for the case when the polarization is nominally parallel to $\vec{E}$. Since the energetic shift of the transitions in the trap field is on the order of the laser bandwidth almost all molecules can undergo a transition.

3.4 Excitation of Molecules in Traps

Important for the modeling of the experimental results is that the electric field vectors that form the trap have a distorted quadrupole geometry. As the voltages are modulated and the traps move, the electric field vectors and thus the axes of the quadrupole rotate relative to the (moving) center of the trap in the Y-Z plane at 3/2 the frequency of the sinusoidal waveforms. The trapping potential itself does not depend on the direction of the electric field vectors creating the trap, but the excitation efficiency for the trapped molecules is strongly time- and position-dependent given the dependence of the transition intensity on the relative orientation of the laser polarization to the electric field vector. The details and

---

[1] In the experiment the electric field points along the axis denoted X, and Z denotes the perpendicular direction, but for convention the axis parallel to an external field is called Z. To avoid confusion with the convention the axes labeling has been adjusted.

implications of this fact will be considered in this section.

Spatial Distribution in the Trap before Excitation

The electric field in the region of a trap above the chip is shown in Figure 3.4(a) for one instant in time, which also shows the equal-field-strength contours. Also shown is the egg-shaped rim of the trap, the contour where the electric field strength is equal to the strength at the saddle point. To find the density distribution of molecules in the trap in the center of the chip where the infrared excitation takes place, classical trajectory simulations are performed (like described in Section 2.5). The density distribution of metastable CO molecules guided to the center of the chip in the $v = 0$, $J = 1$, $M\Omega = -1$ levels is shown in Figure 3.4(b). Note that the simulated distribution is not evenly spread through the trapped portion of phase space, particularly the spread of Y positions is smaller than that of a totally filled trap. This results from the under-filling of the v_Y dimension of phase space at the entrance of the chip inherent to the current setup of the molecular beam machine, presented in Reference [González-Flórez11]. After the free flight of the molecules to the entrance of the chip, the position Y and the velocity component v_Y are correlated. Since the chip samples only a small portion of possible Y values, it samples also only a small portion of possible v_Y values. The different translational degrees of freedom are coupled to each other in the trap, leading to a randomization of positions occupied by the molecules. Nevertheless, the trapped phase space distribution is not completely randomized by the time the molecules arrive at the center of the chip because of a lack of time.

Infrared Laser Orientation

Now the infrared transitions of trapped $v = 0$, $J = 1$, $M\Omega = -1$ molecules are considered in the presence of a variable quantization axis against which the fixed polarization of the IR laser must be compared. For an IR beam traveling in the negative Y-direction, there are two polarization directions of the IR laser that could be used: along the X- and Z-direction. No matter how they rotate, the electric field vectors of the trap always lie in the Y-Z plane, making them always perpendicular to the electric field of X-polarized light. In this case, Q-branch excitation is possible, but does not lead to trapped final states, see Figure 3.4(a). If the light is Z-polarized, however, the fields will be parallel in some regions of the trap and perpendicular in others. For this case, excitations in both the Q-branch and the R-branch can end in trappable states, and it is this case that is considered in detail next.

Distribution after Excitation in a Trap

Combining the simulated phase space density with the spectroscopic calculations, the spatial variation of the excitation efficiency into each rotational level and sublevel in the $v = 1$ state can be predicted. As for the case of the Stark spectroscopy experiments on the free beam, the energy levels and eigenstates of the molecule in the electric field on the chip are calculated by diagonalizing the molecular Hamiltonian, but now generating different eigenfunctions and transition probabilities at each point in space.

The relative spatial distribution of trapped final state molecules, $\rho_{\mathrm{f}}(Y,Z) = \rho_{\mathrm{i}}(Y,Z) \cdot P_{\mathrm{Trap}}(Y,Z)$ is calculated starting from the spatial density $\rho_{\mathrm{i}}(Y,Z)$ of molecules in the initial state times the relative transition probability $P_{\mathrm{Trap}}(Y,Z)$ of exciting and trapping these molecules for each point in space. The relative transition probability $P_{\mathrm{Trap}}(Y,Z) = \rho_{\mathrm{Depth}}(Y,Z) \cdot P_{\mathrm{BW}}(Y,Z) \cdot S_{\mathrm{fi}}(Y,Z)$, consists of three factors.

The first factor $\rho_{\mathrm{Depth}}(Y,Z)$ takes into account the fact that the trap depth for the final state can be different from the initial trap depth. So even if a transition occurred, the molecule might have too much energy and is able to leave the trap simply because the trap is shallower. Therefore, only the fraction $\rho_{\mathrm{Depth}}(Y,Z) = v_{\mathrm{max,f}}(Y,Z)/v_{\mathrm{max,i}}(Y,Z)$ of the molecules will be trapped. In fact, only the $v = 1$, $J = 1$ level has the same trap depth as the initial $v = 0$, $J = 1$ level, so $\rho_{\mathrm{Depth}}(Y,Z) = 1$ in that case. All these molecules will be stably guided to the end of the chip and will therefore be detected. However, the Stark interaction decreases by 1/3 upon excitation to the $J = 2$, $M\Omega = -2$ levels and by 2/3 upon excitation to the $J = 2$, $M\Omega = -1$ levels (see Equation 3.1) and so some formerly trapped molecules are lost after IR excitations in the R-branch and $\rho_{\mathrm{Depth}}(Y,Z) < 1$.

The second factor $P_{\mathrm{BW}}(Y,Z)$ takes into account the bandwidth of the laser of $\Delta = h \cdot 2.5$ GHz (FWHM) and assumes a Gaussian shaped electric field profile of the laser in frequency space. Therefore, $P_{\mathrm{BW}}(Y,Z) = 2^{-(\mathcal{E}(Y,Z)-\mathcal{E}_{\mathrm{min}})^2/(\Delta/2)^2}$. The parameter $\mathcal{E}(Y,Z) - \mathcal{E}_{\mathrm{min}}$ is the spatial variation of the energy shift in the trap relative to the minimum. This factor favors the molecules in the center of the trap because the center laser frequency is tuned to the IR transition for molecules in zero field.

The third factor is the line strength S_{fi}, which has been explained previously. Since the molecular orientation will follow the electric field direction of the trap[2], the dipole moment μ parallel and perpendicular to the IR laser's electric field $\vec{E}_{\mathrm{IR}}$ (along Z) is determined by the trap electric field $\vec{E}_{\mathrm{Chip}}$. The parallel component is $\mu_Z = \mu \cos \Theta$, with Θ the angle between $\vec{E}_{\mathrm{IR}}$ and the $\vec{E}_{\mathrm{Chip}}$. For the perpendicular direction, $\mu_{\mathrm{Y}} = \mu \sin \Theta$. Therefore, S_{fi} will have a component of $\cos^2 \Theta$ for $\Delta M = 0$ and $\sin^2 \Theta$ for the $\Delta M = \pm 1$ transitions.

Figure 3.4(c) shows the distribution of CO molecules excited to the $v = 1$, $J = 1$, $M\Omega = -1$ state immediately after the IR laser pulse. Since the trap shape does not change during this IR excitation, all these molecules remain trapped and will be stably guided to the end of the chip and will therefore be detected. Figures 3.4(d) and (e) show the subset of molecules just after the IR laser pulse arrives that are both excited to the $v = 1$, $J = 2$, $M\Omega = -2$ and $M\Omega = -1$ levels, respectively, and that will arrive at the detector. Due to the previously mentioned difference of the trap depth for the $J = 2$ states, the overall amount of molecules is less than for the excitation to $v = 1$, $J = 1$.

The distributions from Figures 3.4(c)–(e) are shown for one particular instant in time and therefore show only one possible field vector orientation. When the trap fields rotate during guiding, the total excitation probability into each excited state can change by up to ±20% because neither the trap nor the molecule distribution are symmetric under rotations in the Y-Z plane. In the guiding experiments described below, it is made sure that the IR laser timing is scanned in steps incommensurate with the waveform period to average over trap field rotations.

It is known from guiding experiments in the $v = 0$ state that in the present experimental configuration approximately 5% of the signal is due to metastable CO molecules in the $M = 0$ states [Santambrogio11]. Some of these molecules are probably excited to the trappable $M\Omega = -1$ state by the IR laser; when the laser fires some of them will find themselves at the right position to be trapped and subsequently guided off the chip. This small fraction of molecules is neglected in the calculations.

---

[2] It was noticed later, that in the calculations it is assumed that the molecular dipole moment is aligned completely parallel to the trap electric field. In fact, the alignment depends on the electric field strength and a parallel orientation is only approximately true for large electric fields. Also, the electric field strength depends on the position in the trap and is not perfectly constant due to imperfections in the applied waveforms. Therefore, in reality, the spatially dependent transition probability will be less pronounced as shown in Figure 3.4 because always parallel and perpendicular components are present.

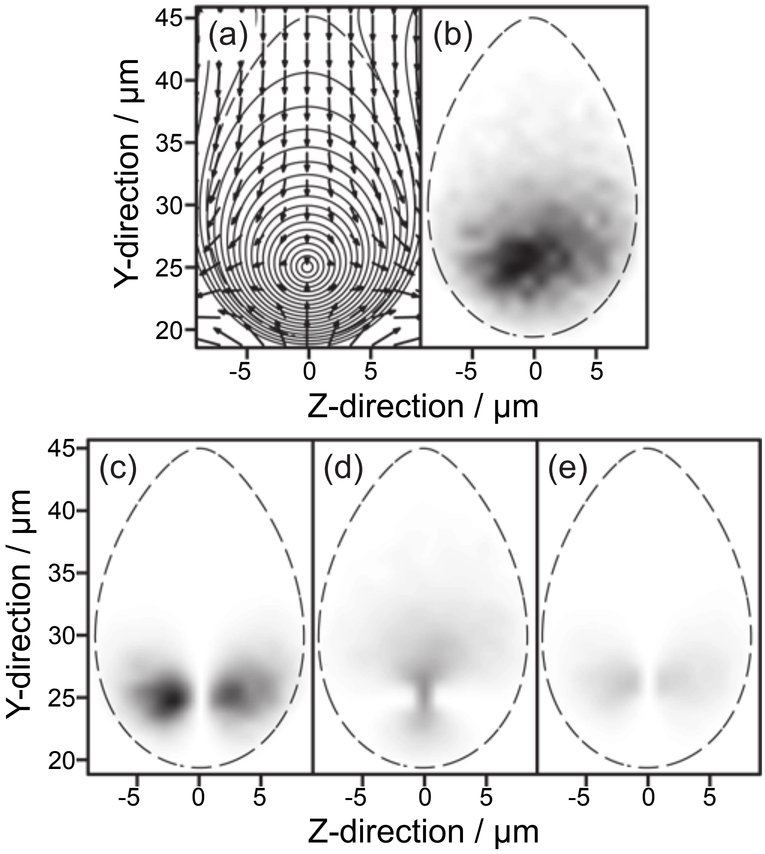

Figure 3.4: Spatial distributions of molecules in the traps. (a) One configuration of electric field in the trap is shown, together with contours of equal electric field strength (solid curves). The dashed contour line is the limit of the trap; outside of this spatial region the molecules cannot be trapped. (b) Trajectory simulations yielding the relative density of trapped molecules in the $v = 0$, $J = 1$ state, 495 µs after the 206 nm laser fired. This corresponds to molecules in the center of the chip. The boundary of the trap is again shown by the dashed curve. The relative densities of molecules excited to (c) $v = 1$, $J = 1$, $M\Omega = -1$; (d) $v = 1$, $J = 2$, $M\Omega = -2$; and (e) $v = 1$, $J = 2$, $M\Omega = -1$ are shown together with the boundary of the trap. While panels (c), (d), and (e) are plotted with the same linear intensity scale, they are not directly comparable to the scale of panel (b) because the absolute excitation probability of the molecular transition and the overall efficiency of the IR laser are unknown.

3.5 Guiding Experiments

When the chip field is turned off, the free-flying molecules have a wide velocity distribution. The arrival time distribution of the molecules at the REMPI detector, measured by scanning the Q-switch trigger time of the ionizing laser, is shown in Figure 3.5(a). This distribution, centered at 790 µs with 55 µs FWHM, corresponds to a velocity of 330 m/s with 20 m/s FWHM. Due to the existing velocity spread of the excited packet, the initial 2 mm packet (given by the 206 nm laser spot size) spreads considerably during its flight through the machine. In the middle of the chip the packet is 8 mm long, and by the time it reaches the REMPI detector it is roughly 14 mm long (FWHM) – if flying freely. Since the IR and REMPI laser spots are approximately 2 mm and 1.2 mm, respectively, these two lasers together act as a velocity filter. Only when they are timed to address the same portion of the expanding packet, one can detect vibrationally excited molecules. To address the entire packet of free-flying molecules with both lasers the IR and the REMPI lasers are scanned together with two different timesteps. The timestep used to scan each laser is proportional to the size of the packet of molecules at the position of that laser beam. This measurement, shown in red in Figure 3.5(a), is virtually identical to that of the free-flying molecules in the $v = 0$ state.

When the chip waveforms are turned on with a frequency of 2.75 MHz, molecules with velocities different from 330 m/s are selectively repelled from the chip surface, resulting in a dramatically narrowed arrival time distribution. For example, molecules guided in the $v = 0$, $J = 1$ level, that is, with no IR radiation present, are shown overlaid on the free-flying signal in Figure 3.5(a). Note that because the molecule chip manipulates the forward velocity of the CO molecules as they traverse the experiment, there is no straightforward conversion between arrival time to molecular velocity unless the chip is turned off.

The phase space acceptance of the chip decelerator for molecules in trappable states is strictly related to the trap depth: for deeper traps a larger portion of the incoming velocity distribution will be accepted in each trap and a larger number of traps will be filled. This, in turn, manifests itself in a wider time of flight distribution at the REMPI detector because the packet of molecules leaving the chip is both longer and spreads more during its flight to the detector. This fact is used as an experimental probe of the trap depth by validating the trajectory simulation results (convolved with the 1.2 mm FWHM ionization laser spot size) against the measured data. Figure 3.5(b) shows the measured

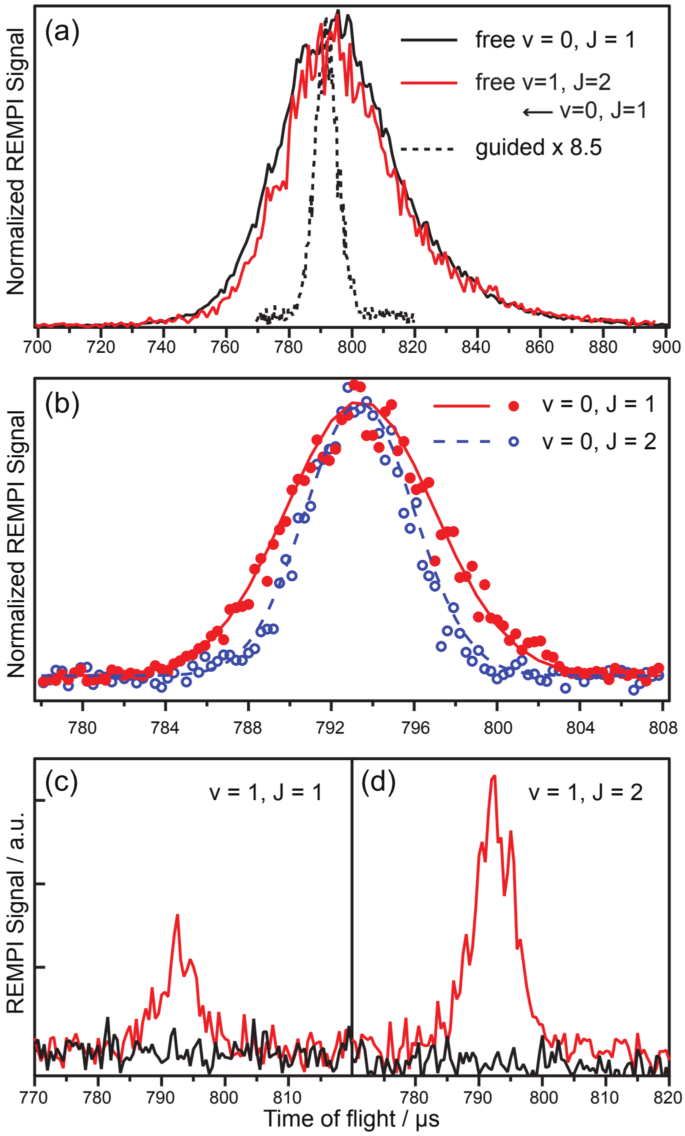

Figure 3.5: Arrival time distributions of CO molecules, guided and unguided. (a) Arrival time distributions of free-flying and guided $v = 0$, $J = 1$ molecules with normalized peak intensity. (b) Experimental measurement (markers) and trajectory simulations (lines) of $v = 0$, $J = 1$ (red disks) and $v = 0$, $J = 2$ (blue circles) molecules guided at 330 m/s. The arrival time distributions of guided molecules in the $v = 1$, $J = 1$ and $J = 2$ levels pumped from the $v = 0$, $J = 1$ level with (red) and without (black) the IR laser are shown in panels (c) and (d), respectively.

and simulated arrival time distribution of molecules guided at 330 m/s when the 206 nm laser is used for preparation in the $v = 0$, $J = 1$ or 2 levels. The background level is related to molecules in the $M = 0$ levels. Since they interact only very weakly with the chip fields (they are weakly hfs), few of them are hitting the chip surface but most molecules fly unhindered across the chip even when the waveforms are on and arrive at the detector with the same arrival time distribution as unguided molecules. In the guided peaks of Figure 3.5(a) and (b), one can see that molecules in the $M = 0$ levels contribute very little to the observed signal: the unguided background is at most only a few percent of the guided peak.

When the IR laser is used to promote the trapped molecules to either $J = 1$ or $J = 2$ in the $v = 1$ level from $J = 1$, $v = 0$, the arrival time distributions shown in Figure 3.5(c) and (d) result. The red lines show the relative number of vibrationally excited molecules arriving at the detector when the IR laser is present; the black curves show what happens when the IR laser is blocked, indicating that there is no contamination of the vibrationally excited signal by metastable molecules in the $v = 0$ level. These data clearly show that trapped $v = 0$ molecules may be excited by infrared radiation while flying close to the surface of the microchip. The combined efficiency of the excitation and guiding off the chip is estimated to be approximately 10%.

Trajectory simulations indicate that molecules promoted to the $M = 0$ levels have only one tenth the probability of reaching the detector as those promoted to low-field-seeking levels. For the case of a Q-branch transition, the relative probability of excitation in the trap to $M = 0$ levels is approximately 50%. Therefore, it is concluded that the signal consists of less than 10% $M = 0$ molecules. This number is reduced to approximately 0.5% for R-branch transfer. Additionally, molecules that are promoted to low-field-seeking states but that are not trapped are repelled from the chip surface. They are blocked by the 50 µm slit and do not contribute to the measured signal. Molecules promoted to high-field-seeking states are attracted to the chip, crashing into the surface.

Alternative Excitation Scheme

So far, only one-photon transitions of molecules trapped on the chip have been considered. Now, an alternative approach to populate low-field-seeking states will be presented, which has ultimately not been used for experiments. As discussed in Section 3.3, in a strong electric field the selection rules for excitation of various M-states depend on the angle between the polarization of the laser and the electric field. In the middle of the trap, however, the field is weak (or nonexistent) and the parity of the upper and lower portions of the Λ-doublet are not totally mixed or not mixed at all. In this spatial region only a two-photon transition can connect the low-field-seeking positive-parity levels of $v = 0$, $J = 1$ and $v = 1$, $J = 1$. This two-photon scheme could be achieved, e.g., by the absorption of two IR photons or by the excitation to another state and the subsequent emission of a photon. One possible way to do this is to use an optical transition to an electronic state that fluoresces quickly on the timescale of the trap motion. A good candidate is the $b^3\Sigma^+$ state, which has a lifetime of approximately 86 ns and decays primarily by fluorescence back to the $a^3\Pi_1$ state [Schwenker65]. If the transition $b^3\Sigma^+, v = 0 \leftarrow a^3\Pi_1, v = 0$ is saturated, and assuming a Franck-Condon factor of 0.23 [LinodaSilva06] to the $a^3\Pi_1, v = 1$ level, approximately 11% of the excited molecules will be distributed over various rotational levels in the $v = 1$ manifold. Exciting to the $N' = 1$ level in the $b^3\Sigma^+$ state ($J' = 2$ since $N' = J' - S'$ and $S' = 1$), which has negative parity, means that only $J = 1$ and $J = 3$ ($\Delta J = \pm 1$) are populated by fluorescence in the field free region at the center of the trap, while $J = 2$ ($\Delta J = 0$) is also populated in the parts of the trap where a field is present. An overall transition efficiency of few percent could be hoped for. This scheme was briefly tested but as about an order of magnitude fewer molecules were obtained in the vibrationally excited $J = 1$ level than with direct IR pumping, no further experiments have been performed in this way.

Influence of the Magnetic Field

Finally, it is worth considering the effect of the 190-Gauss magnetic field across the chip. While the Zeeman shift from this field is small compared to the Stark shift in the edges of the trap, in the middle of the trap it is larger than the (vanishing) Stark shift. Therefore, molecules at the middle of the trap actually experience a different quantization axis than those at the edge of the trap, changing the appropriate choice of basis set and the selection rules. The Zeeman shift is 0.466 MHz/Gauss for ^{12}CO $a^3\Pi_1$, $v = 1$, $J = 1$ [Meek11b], amounting to a splitting of 89 MHz in this setup. It is estimated that the Zeeman interaction is more important than the Stark interaction only within a 1.1 µm radius about the trap center, containing approximately 4.5% of the total trapped molecules. Therefore, aside from preventing nonadiabatic transitions, the magnetic field is not expected to have a measurable effect on the experiments described here.

3.6 Conclusion

In these experiments, the vibrational excitation of molecules trapped on a microchip has been studied. While in the traps, CO molecules are vibrationally excited by a narrowband infrared laser and subsequently guided off the chip for state-selective detection via REMPI. For understanding the transitions of the trapped molecules, the interplay between the pumping field and the trapping field needs to be taken into account. For this purpose, first the spectroscopy of free-flying CO molecules in the $a^3\Pi_1$ state in a homogeneous electric field has been studied. Then the model of the Stark spectra in a homogeneous field was extended to the more complicated case of the inhomogeneous, rotating field of the microtraps. Depending on the polarization direction of the laser, different transitions can be addressed. The population transfer between trapped states in different vibrational levels has been demonstrated using two of these transitions.

CHAPTER 4

Imaging of Molecules on a Chip

4.1 Introduction

Imaging detection of ultracold atoms is arguably the fundamental diagnostic technique of the ultracold world. For this purpose, an atomic cloud is illuminated with a laser beam, which is tuned to a closed, two-level, optical transition. A closed transition has the property of leaving the atom in the same quantum state after one photon has been absorbed and then reemitted, or scattered. In this way, the process can be repeated many times and, thus, many photons are scattered. Either the fluorescence is observed or the shadow that is cast by the atomic cloud. [Ketterle99, Bücker09, Ockeloen10, Smith11] By releasing the atomic cloud from its trap and recording multiple fluorescence images at different times, it is possible to determine, for example, the temperature of the atomic gas. [Weiss89]

Generally, molecules lack closed two-level transitions, which are essential for efficient fluorescence or absorption imaging. Moreover, typical number densities of molecular clouds

---

Adapted from:

Imaging Cold Molecules on a Chip
Silvio Marx, David Adu Smith, Mark J. Abel, Thomas Zehentbauer, Gerard Meijer and Gabriele Santambrogio, *Physical Review Letters* **111**:243007 (2013)

Measuring and Manipulating the Temperature of Cold Molecules Trapped on a Chip
Silvio Marx, David Adu Smith, Giacomo Insero, Samuel A. Meek, Boris Sartakov, Gerard Meijer and Gabriele Santambrogio, *Physical Review A* **92**(6):063408 (2015)

are much lower than for atoms, further complicating the detection process. Finally, the chip environment poses yet another challenge because the presence of a physical structure so close to the molecular sample introduces scattering or laser-induced fluorescence from the chip surface. Instead, Resonance Enhanced Multi-Photon Ionization (REMPI) [Ashfold94] is a generally applicably method, is state selective, extremely sensitive, and intrinsically background-free. Once the molecules are ionized, they can be collected and counted with great efficiency, and also ion imaging is straightforward. This method has been already successfully employed in the past for off-chip detection. [Santambrogio11, Abel12b, Meek11b]

In the experiments presented in this chapter, REMPI is used for the first time for on-chip detection. On-chip imaging detection allows one to follow the ballistic expansion of a molecular cloud, which is used here to determine the translational temperature of the molecules with a purely experimental method. In contrast to the experiments on ultracold atoms, where the typical densities are high enough to guarantee thermalization of the ensemble, in these experiments the densities are much too low. However, a nearly Maxwell-Boltzmann energy distribution is observed. Therefore, a discussion of the origin of the phase-space distribution that is found in the experiments and in the calculations is provided below.

4.2 Experimental Setup and Detection

The experiments are performed in the same vacuum chamber that has been used for the vibrational transitions on the chip, which has already been presented in Section 2.3. The excitation laser has a spot size of roughly 1 mm and by the time the metastable molecules reach the chip's entrance 40 mm downstream, their phase-space distribution shows a strong correlation between position and velocity in the Z-direction. The faster molecules have moved toward the front of the packet while the slower have lagged behind, so that by the time the packet reaches the chip's entrance it is roughly 4 mm long and its local average velocity in the Z-direction changes by 9 m/s every mm. Over the 20 µm size of each microtrap, any correlation between position and velocity of the molecular ensemble is negligible, and a uniform distribution in phase-space can be assumed: The distribution of the captured molecules is limited in all directions by the acceptance of the microtraps, except for the velocity component in the Y-direction, for which the microtraps are slightly underfilled. Once the traps are turned on and the molecules are captured, the distribution of the ensemble undergoes a minor rearrangement by oscillating around in the trap, that leads to the filling of the whole available phase space in the traps.

In all the experiments presented in this chapter, molecules are immediately decelerated by -1 µm/µs^2 upon arrival on the chip down to a velocity between 207–138 m/s. This deceleration is sufficient to separate the trapped molecules from the background of untrapped molecules. Since the trap depth would change going from constant speed to deceleration, the molecules enter the chip experiencing the shallower, decelerating trap already from the very beginning on the chip. Typically a series of approximately 10 microtraps is filled, which may be reaccelerated if a different final velocity is desired. The molecules are detected using (1+1)REMPI ionization via the $b^3\Sigma^+$, $v = 0$, $N = 1$ state using 0.8 mJ/mm^2 of laser light at 283 nm that propagates parallel to the chip surface. The molecular density is 10^7/cm^3 in the traps, which corresponds to approximately five molecules per microtrap. The high sensitivity of REMPI allows one to work under such conditions.

For the simplest implementation of on-chip detection (i.e. no imaging) the molecules in the region of the microtraps are ionized after switching the traps off. All microelectrodes are switched to 0 V and, additionally, a rectangular ring electrode parallel to the chip surface, but offset above the chip by 4 mm, is held at -100 V. The exact voltage applied to this rectangular ring electrode for non-imaging detection is not critical. In this way the microelectrode array acts as an anode for the newly generated cations and the rectangular ring as a cathode, see Figure 4.1. After flying through the cathode, the cations are then collected by a microchannel plate (MCP) detector. In this way the number of ionized molecules can be determined for a given set of parameters, allowing, e.g., the optimization of ionization timing or manipulation sequences on the chip. In addition to a simple determination of the ion number, spatial and velocity map imaging [Eppink97] can be performed with this setup. However, with the present ionization scheme, ion recoil energies are of the order of tens of mK, i.e., comparable with the trap depths, which makes velocity map imaging imprecise for the analysis of the velocity distributions inside the microtraps. Therefore, measurements are only done using spatial imaging. For imaging detection (Figure 4.1), the molecules are released from the microtraps in the Z-direction and they expand ballistically for a variable time duration, so that various snapshots can be taken at different expansion times. This allows for the interrogation of their phase-space distribution in the X-Z plane. The release of the microtraps occurs sequentially: upon arrival at the end of the microtrap array each trap rapidly opens up.

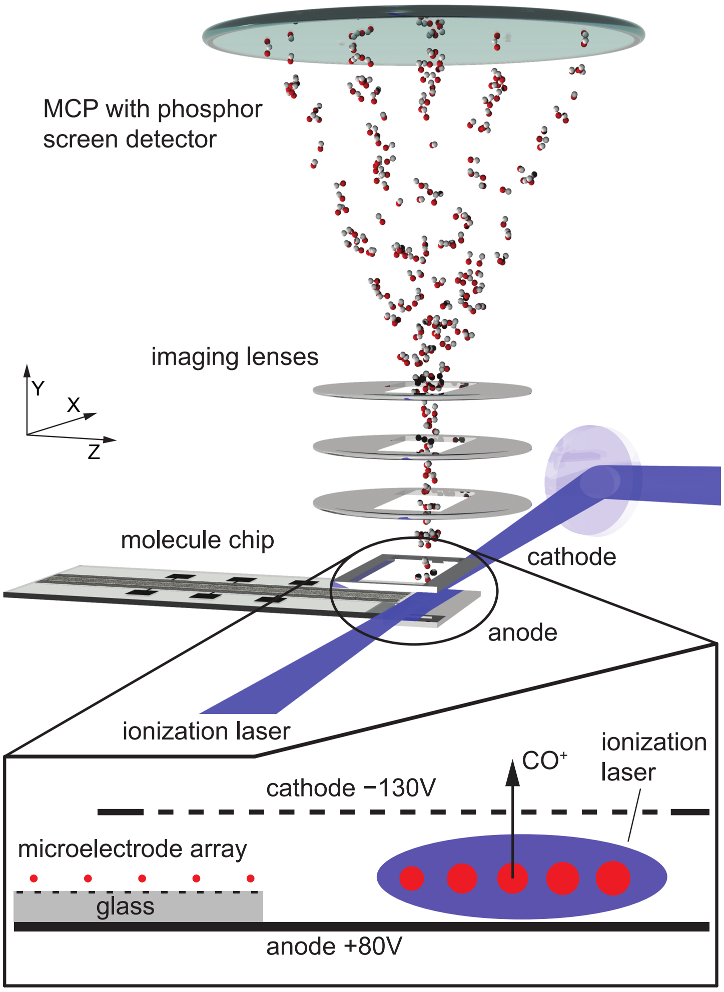

Figure 4.1: On-chip detection setup. The figure schematically shows the spatial imaging of five molecular clouds. Metastable CO molecules on the molecule chip are ionized via REMPI using a pulsed 283 nm laser. The detection region is composed of two electrodes: an anode and a cathode. The cathode is a rectangular ring. Together, the two electrodes protect the cations from stray fields in the region of the chip. Ion optics are then used to form an image on an MCP detector backed by a phosphor screen. A CCD camera (not shown) is used to record the image of the molecules from the phosphor screen. A sketch of the detection region is shown in the inset, not to scale. In the bottom part, two points in time are shown: on the left, when the molecules are still trapped above the microelectrode array; on the right, after ballistic flight, upon reaching the axis of the imaging lenses.

The electric field homogeneity achievable above the microelectrode array, however, is not sufficient for spatial imaging. Therefore, an extra anode directly behind the microtraps region is added (Figure 4.1), wider than the microtraps in the X-direction and 10 mm long in the Z-direction. This anode is held at +80 V. The molecules expand ballistically while they fly above the anode after being ejected from the microtraps. Moreover, the molecules would quickly collide with the chip surface because they are trapped only approximately 20 µm over its surface, which is the reason why this electrode is recessed by 2 mm under the plane of the traps to leave enough space for the expansion. As a cathode the same rectangular ring is used as for the non-imaging detection (Figure 4.1). For imaging, the cathode is held at −130 V. Together the anode and cathode reduce the inhomogeneity of the electric field and therefore any associated imaging aberrations. The ions generated by REMPI are imaged using ion optics onto an MCP detector with phosphor screen situated 40 cm above the chip surface and recorded using a fast CCD camera. The ion optics for the experiment are a standard set of three asymmetric ion lenses located 26 mm from the chip surface, spaced by 10 mm and all held at −400 V. The openings in the centers of the ion lenses of 22 by 72 mm provide magnification factors at the MCP of 2 and 58, in the direction of the tubular trap axis and the direction of the trap movement, respectively. This asymmetric magnification is chosen because of the large aspect ratio of the tubular microtraps (200).

An example image of molecules, taken using the aforementioned setup, is shown in Figure 4.2(a). This is the sum of approximately 10^5 experimental cycles. Each dot in the image represents a count detected with the MCP, phosphor screen and camera. Since the MCP is gated around the arrival time of the CO ions, almost all of the counts represent measured CO ions. The individual traps can be clearly resolved. The dynamics of the molecules along the 4-mm length of the microtraps (X-direction) is negligible for the experiments presented in this chapter because the molecules almost never experience a force in that direction during the relatively short time they spend on the chip. Therefore, the signal is integrated along the X-direction (vertical axis of the image) and the analysis concentrates on the perpendicular direction, as shown in Figure 4.2(b). Each microtrap releases its molecules upon reaching the end of the microelectrode array, i.e., the clouds are released sequentially, each time at the same position. Numerical simulations show that each trap rapidly opens up upon arrival at the end of the microelectrode array. This happens within hundreds of nanoseconds, i.e., instantaneously for the molecules. The

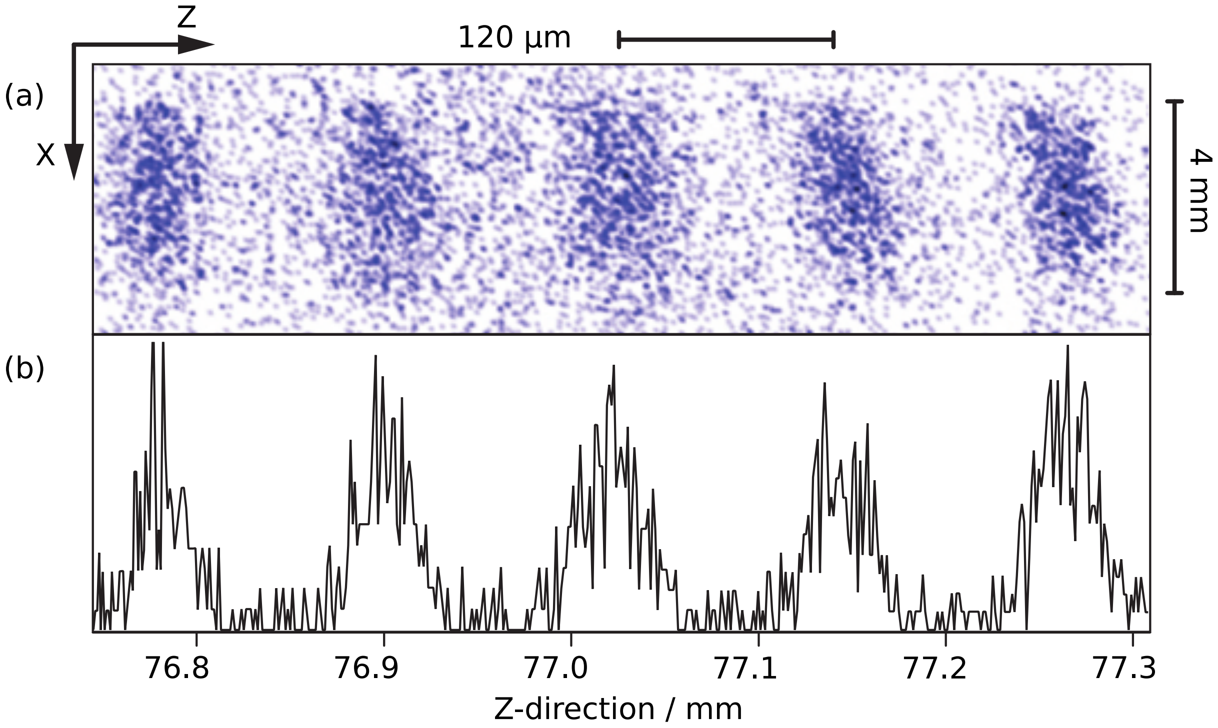

Figure 4.2: Measured spatial image of previously trapped molecules on the chip. (a) 2D image of molecules from 5 individual traps after an expansion time of 9 µs. (b) Line profile resulting from the vertical integration of an image like in (a). The vertical direction is along the length of the microtrap, X. The extreme aspect ratio of the microtraps, X:Z = 200:1, is reduced to approximately 7:1 by the asymmetric magnification factors of the lenses. Some ion-optics aberrations can be observed on the right hand side of the image, in particular at shorter expansion times. The experiment runs at a rate of 10 Hz and the images are the sum of approximately 10^5 experimental cycles. Approximately 1–2 counts/s are recorded. The resolution of the imaging system in the Z-direction is 0.78 pixel/µm.

fields disappear with a monotonic decrease in the electric field strength gradient. For each individual molecular cloud, the distance between release from the microtrap and detection is fixed. Therefore, the control of the expansion time, determining the cloud width, is done by controlling the velocity at which the molecular clouds are ejected from the microtraps, i.e., by defining the speed at which the microtraps move over the chip surface just before being released. Therefore, a lower velocity of the microtraps gives a longer time for ballistic flight. The ballistic expansion times are given for the central cloud in each image. With the signal-to-noise ratio of these experiments, any difference in cloud size between the rightmost and leftmost clouds (due to slightly differing expansion times) was undetectable.

4.3 Measurement of the Temperature of Trapped Molecules

In this section, the phase space distribution of trapped molecules is investigated. Trapped ensembles of molecules with different velocity distributions can be created, which can be verified using the imaging technique. Comparison of the measured images with results from trajectory simulations allow the assignment of an effective temperature to the trapped samples. The reason why the assignment of a temperature in the absence of thermalization is still a reasonable approach is made clear by analyzing the energy distribution from molecule ensembles from traps of different shape. Finally, the ballistic expansion of a trapped ensemble is observed over time using the imaging technique and an analytic model is used to extract the temperature directly from the data.

4.3.1 Molecules in Traps of Different Depth

Figure 4.4 shows four different measurements of molecular distributions after trapping in microtraps of different depth but otherwise similar shape. All measurements are taken after a ballistic expansion time of 15 µs, after decelerating the molecules to 207 m/s, see Figure 4.3. The depth of the microtraps is controlled by the amplitude of the voltage waveforms applied to the microelectrodes on the chip surface, which for these measurements was, respectively, 120, 160, 200, and 240 V. After the initial deceleration phase to separate the trapped molecules from the background gas, the microtraps were made to move uniformly for the final phase of the manipulation sequence. Both from an analytical

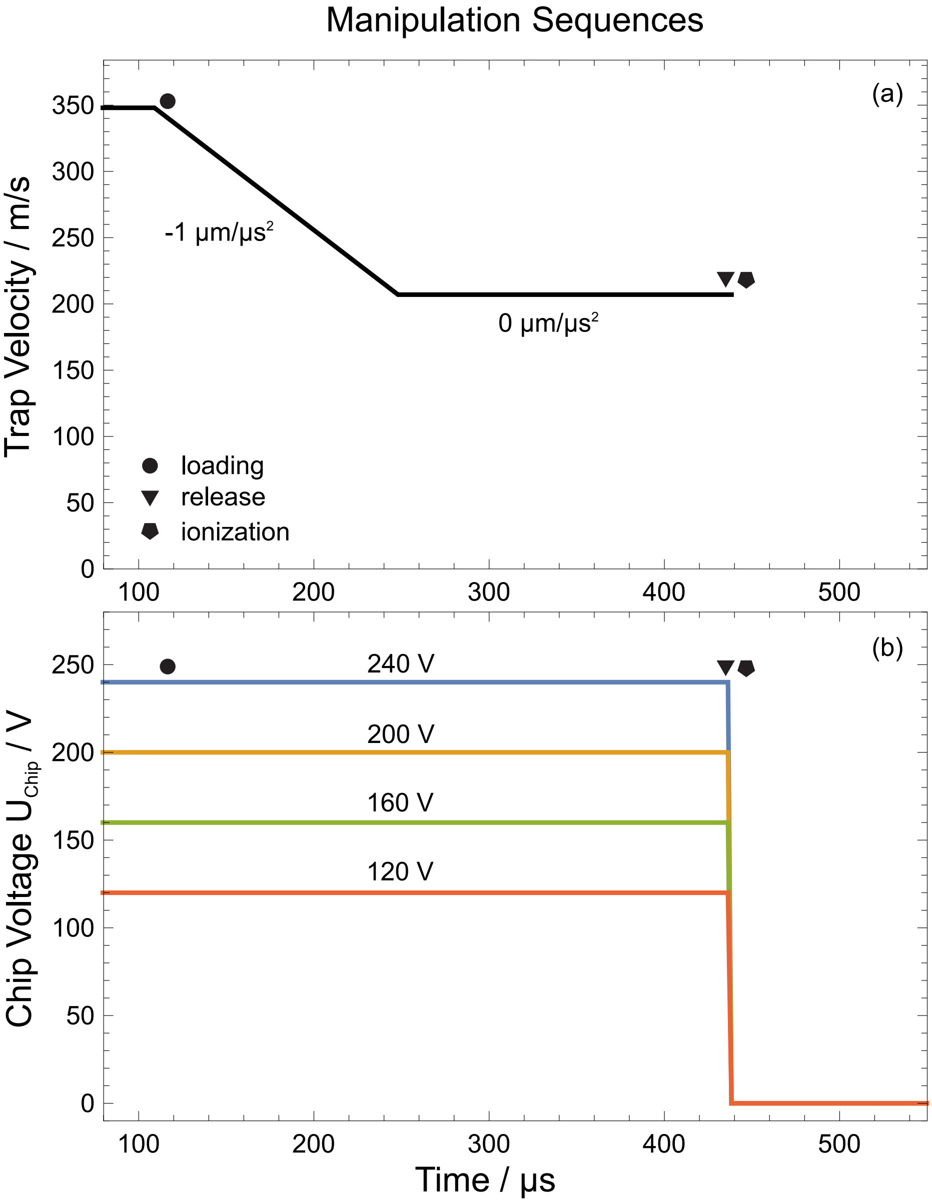

Figure 4.3: Manipulation scheme on the chip for trapping and detecting molecules in traps of different depths. Velocity of the traps (a) and voltages applied to the chip (b) as a function of time. The velocity scheme is the same for all measurements. Symbols mark the time of loading the molecules on the chip (circles) release at the end of the chip (triangles) and ionization (pentagons).

description of the electric field of the microtraps and from finite element simulations, the trap depth for the chosen amplitudes of the applied voltage waveforms, defined as the difference between the minimum and the saddle point of the trapping potential, is known. The depths under deceleration are 10, 28, 46, and 65 mK, respectively for the four voltages, and 39, 55, 71, and 87 mK, under uniform motion.

The spatial distribution of the molecules in the Z-direction was calculated from numerical trajectory simulations. These results are also shown in Figure 4.4 and compare well to the measured experimental data. From the simulations, information about the phase-space distribution of the molecules is extracted. In Figure 4.4(b) the computed speed distributions for the measurements shown in (a) are plotted together with the best-fit Maxwell-Boltzmann curves

$$f(v) = \left(\frac{m}{k_{\mathrm{B}}T}\right) v e^{-\frac{mv^2}{2k_{\mathrm{B}}T}}. \tag{4.1}$$

Since the low number density in the microtraps ($10^7/\mathrm{cm}^3$) rules out any thermalization of the sample, a good fit to a Maxwell-Boltzmann distribution cannot be expected in general. However, when observing the speed distributions given by the trajectory simulations, it is found that they approximate two-dimensional Maxwell-Boltzmann distributions. To understand how such a distribution arises, it is helpful to reflect on the expected distribution of the kinetic energy of an ensemble of particles when they are released from a trap with a certain shape.

Comparison of the Energy Distributions of Ensembles in Different Trap Shapes

It is assumed that the ensemble of molecules confined in the microtraps is an ergodic system, i.e., that the time spent by the system in some region of the phase-space of microstates with a given energy is proportional to the volume of that region. The experimental data are acquired by averaging over many measurement cycles, so the measured phase-space distribution is an ensemble average and is proportional to the time spent by the system in that configuration. Thus, from the bare knowledge of the shape and depth of the microtraps, it must be possible to derive the expected kinetic energy distribution in the chip microtraps when they are opened.

More specifically, the relative probability density $\rho(\mathcal{E}_{\mathrm{Kin}})$ for a specific kinetic energy $\mathcal{E}_{\mathrm{Kin}}$ captured by a trap from the molecular beam can be determined as follows. Since the chip traps have a very small volume, the number density and energy density within the whole

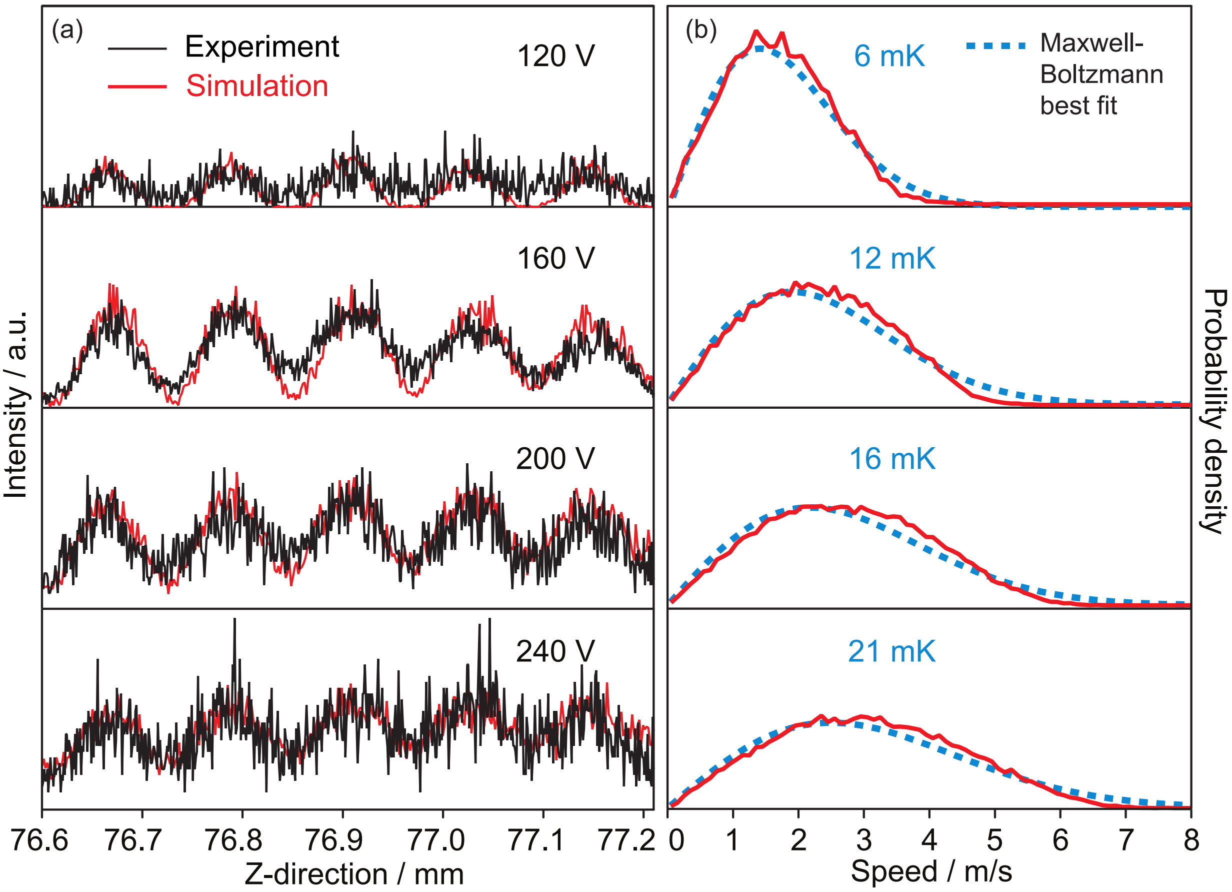

Figure 4.4: Analysis of integrated images of traps of different depths. (a) Integrated line profiles (black) from images of molecules for different microelectrode voltages, i.e., differing trap depths, along with the results of numerical trajectory simulations (red). The maximal relative speed $v_{\text{max}} = \sqrt{2\,U/m}$ of stably trapped molecules (given by the trap depth U under deceleration) was 2.4, 4.0, 5.1, and 6.1 m/s, respectively. (b) Corresponding speed distributions (red) extracted from the trajectory simulations, along with the best-fit Maxwell-Boltzmann curve (blue dashed line), labeled with the best-fit temperature. Speeds are given relative to the mean forward velocity of the molecular cloud.

volume which a trap occupies can be assumed to be homogeneous, as has been explained at the beginning of Section 4.2. Then, the relative probability density of one specific kinetic energy component captured in the trap is determined from the relative volume which can be occupied by molecules with this energy: $\rho(\mathcal{E}_{\text{Kin}}) \propto V(\mathcal{E}_{\text{Kin}} + \mathcal{E}_{\text{Stark}} \leq \mathcal{E}_{\text{max}})$. Since to a very high degree the form of the potential is independent of X, the problem is effectively two-dimensional and $V = Ad$, with a trap length of $d = 4$ mm along X. Therefore, it is only necessary to determine the area, A, of the trap where $A(\mathcal{E}_{\text{Stark}} \leq \mathcal{E}_{\text{max}} - \mathcal{E}_{\text{Kin}})$.

Since the trapping potential is known analytically, the area A can simply be determined by integrating all positions of the trap where the above mentioned condition holds. By normalizing the integral of the obtained distribution of $A(\mathcal{E}_{\text{Kin}})$ for a given trap depth $\mathcal{E}_{\text{max}}$ to unity, the relative kinetic energy distribution is obtained. Because the maximum trap depth not only depends on the chosen chip voltage, but also on the deceleration and the time given for the transiently trapped molecules to escape the trap, the effective trap maximum $\mathcal{E}_{\text{max}}$ is not known *a priori* and needs to be fitted to data obtained from simulations. The integration for a microtrap in uniform motion with an amplitude of the applied potentials of 160 V is shown in Figure 4.5(a) together with the distribution obtained from trajectory simulations for the same conditions of the measurement shown in Figure 4.4 at 160 V. This simple result reproduces correctly the energy scale of the distribution and the overall shape of the curve. However, the distribution from trajectory simulation is colder than the result of integration. This reflects the history of the trapped molecules that proceed from the shallower decelerated traps. The best match between the two distributions is obtained when a cut-off energy of 40 mK is introduced in the integration of the available trap volume (shown in the figure as a dashed line), which is an intermediate value between the depth of the uniformly moving (55 mK) and the decelerated (28 mK) trap. This observation is attributed to the fact that the deceleration phase is not long enough to allow the system to reach a stable condition, i.e., the molecules are still transiently trapped at the end of the deceleration phase. This explanation is corroborated by the numerical trajectory simulations that show that many molecules are still escaping from the traps at the end of the deceleration phase.

These results can be compared with the energy distributions expected from potentials with a more regular shape. For simple geometries such as a conical (linear) trap the probability distribution is obtained by assuming $\mathcal{E}_{\text{Stark}} \propto r$. Since $A = \pi r^2$, $A \propto \mathcal{E}_{\text{Stark}}^2 = (\mathcal{E}_{\text{max}} - \mathcal{E}_{\text{Kin}})^2$, a parabola with the minimum at energy $\mathcal{E}_{\text{max}}$. Another rele-

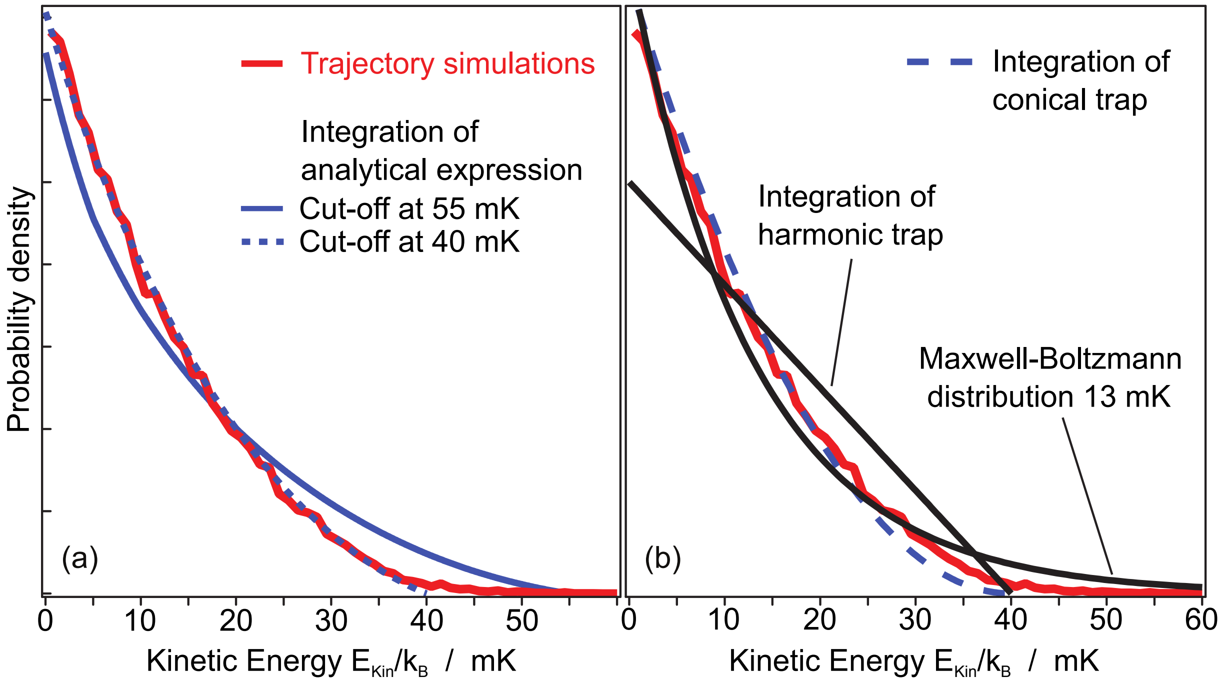

Figure 4.5: Energy distributions from trajectory simulations and from different analytical models. (a) Energy distribution from trajectory simulations, calculated for the same conditions as in Figure 4.4 for the 160 V case (solid red line). In blue, the energy distributions obtained by integrating the analytical expression of the trapping potential are shown, for the cut-off values of 55 and 40 mK. (b) Comparison with the distribution obtained from the traps with more regular shapes: a conical, a harmonic, and a logarithmic trap. All distributions are normalized.

vant example is a harmonic (quadratic) trap shape. There, $\mathcal{E}_{\text{Stark}} \propto r^2$, implying that $A \propto \mathcal{E}_{\text{Stark}} = \mathcal{E}_{\text{max}} - \mathcal{E}_{\text{Kin}}$, which is just a straight line with the minimum at $\mathcal{E}_{\text{max}}$. Both cases are shown in Figure 4.5(b) for comparison by normalizing the integral of the distributions to 1. The harmonic potential is found to be a poor approximation for the trap. Instead, a conical potential gives an excellent approximation of the actual potential with only minor differences. For both the conical and the harmonic case, the trapping potentials are abruptly terminated 40 mK above the minimum, following the findings in the treatment of the exact potential from figure (a). An interesting potential is the one with a logarithmic shape. The integration of such a potential returns an exponential distribution for the kinetic energy, $\rho(\mathcal{E}_{\text{Kin}}) \propto e^{-\mathcal{E}_{\text{Kin}}/(k_{\text{B}}T)}$, which is precisely the Maxwell-Boltzmann distribution for a thermal ensemble in two dimensions. The comparison with this potential, however, is somehow more complex because there is no minimum from which to calculate the 40 mK. However, the Maxwell-Boltzmann distribution that results from the integration of the potential for the comparison can directly be used. The best fit for the temperature of the Maxwell-Boltzmann distribution is found at $T = 13.0 \pm 0.4$ mK, where the fitting error corresponds to 2σ. The major discrepancy with the other curves is of course in the high-energy tail that the infinitely deep logarithmic trap makes possible.

From this it is concluded that the similarity of the phase-space distributions of the molecules trapped on the chip to Maxwell-Boltzmann distributions is due to the shape of the microtraps and not to any sort of thermalization process. The shape of these microtraps can be well approximated by a conical one and a trap with a logarithmic potential would return a distribution that resembles perfectly a thermal one. Hence, although the temperature is not strictly defined, the characterization of the molecular ensemble using a temperature is useful and a thermal distribution captures the main features of the molecular ensemble.

4.3.2 Mapping the Ballistic Expansion

The above results show that one can trap a molecular ensemble with a given temperature, defined by choosing the depth of the microtraps on the molecule chip, and that one can model the system accurately using numerical trajectory simulations. The ability to take snapshots at different times in the ballistic time-of-flight evolution of the molecular ensemble can also be used to advantage. For this, the experiment is repeated at an electrode voltage of 160 V, recording multiple images during the ballistic expansion of the molecule cloud to follow the evolution of the system. This, of course, is only meaningful if the initial conditions are the same for each measurement. It was made sure, therefore, that the molecules experienced the same trap depth and shape for every measurement. The scheme for achieving the different expansion times is shown in Figure 4.6. Different microtrap velocities are achieved at the point of release by applying a fixed deceleration of -1 µm/µs^2 (-10^6 m/s^2) for different time durations and, in one case, followed by an acceleration of the same magnitude. A waveform amplitude of 160 V peak-to-peak applied to the microelectrodes creates 28 mK deep traps for CO molecules in the low-field-seeking component of the $a^3\Pi_1$, $v = 0$, $J = 1$ level under this acceleration. Upon reaching the desired final velocity, the motion is made uniform, increasing the trap depth to 57 mK while the trap diameter increases from 4 to 20 µm.

Four images are shown in Figure 4.7. They show molecules ejected from the microtraps toward the detection region, after a ballistic expansion time t_b of 9, 15, 19, and 22 µs. For these ballistic expansion images, the molecules were released when traveling uniformly at 336, 207, 162, and 138 m/s, respectively. They flew the approximately 3-mm distance between the point of release from the microtraps and the axis of the imaging lenses in the detection region, which defined the time the REMPI laser was fired. One can clearly distinguish the single traps and follow the ballistic expansion of the molecular clouds. At a still relatively short time of flight of 22 µs the resolution of the individual microtraps is almost completely washed out. This highlights the importance of on-chip detection for spatial imaging to preserve a maximum of information.

In Figure 4.8(a) the integrated line profiles for the measurements using four different ballistic expansion times are shown. The ballistic expansion of each individual molecular cloud, each from an individual microtrap, can be seen with increasing expansion time. However, for times t_b >20 µs, it becomes increasingly difficult to discern the individual microtraps as the individual clouds expand into one another. These measurements are shown together with the results of numerical trajectory simulations. Experiment and simulations show good agreement, demonstrating that both the ballistic expansion and the ion imaging process are not significantly hindered by stray electric fields. The analysis of these trajectory simulations shows that this trapped ensemble of molecules does not have a perfectly thermal speed distribution. However, a comparison of the molecular velocities to a Maxwell-Boltzmann distribution remains helpful for understanding the order of magnitude of the observed phenomena, as has been seen already in Subsection 4.3.1. In Figure 4.8(b),

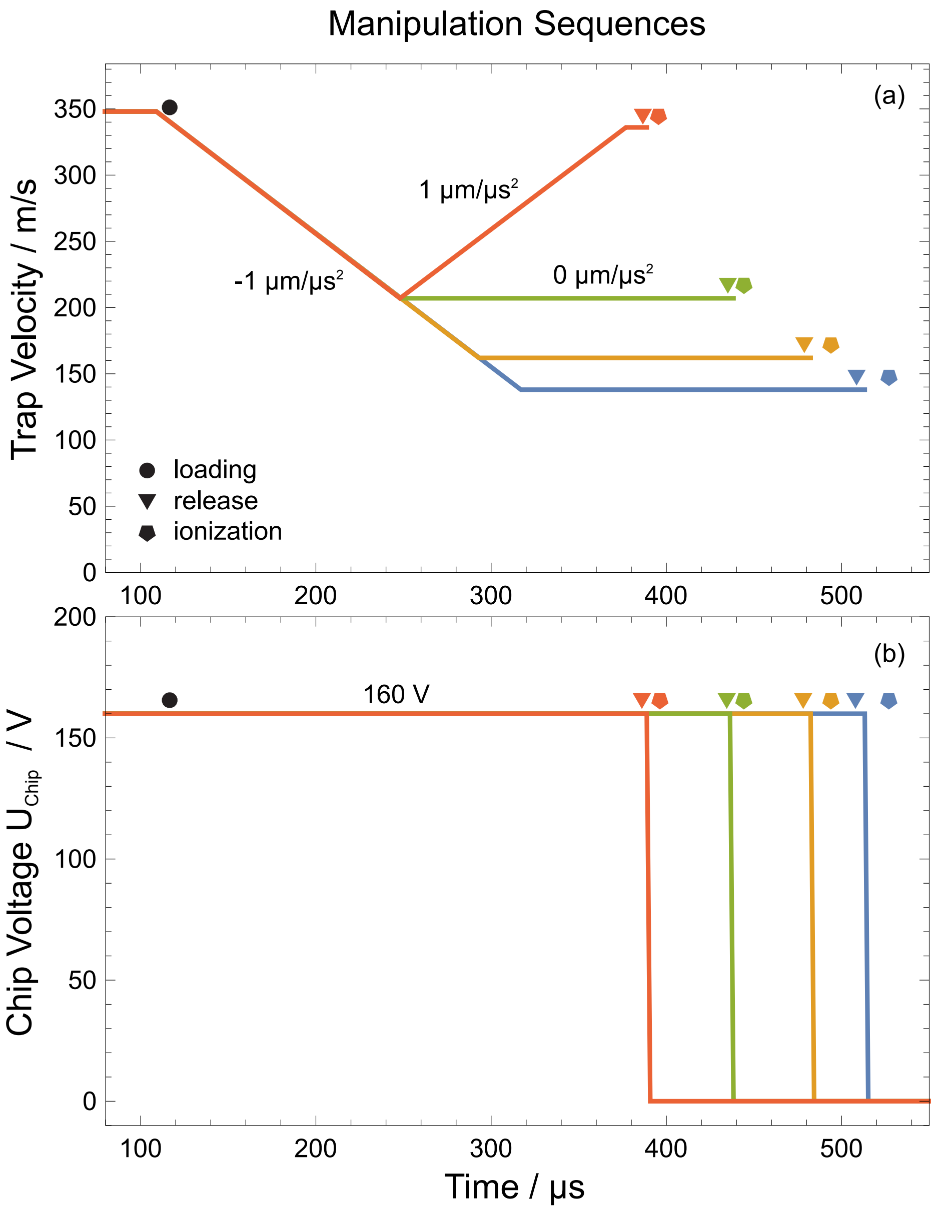

Figure 4.6: Manipulation scheme on the chip for mapping the ballistic expansion. Equivalently to the manipulation scheme shown before, the velocity of the traps (a) and voltages applied to the chip (b) as a function of time are shown. The loading of the molecules on the chip (circles), the release at the end of the chip (triangles) and the ionization (pentagons) are marked. The molecules experience the same trap depth until they are guided to the end of the chip.

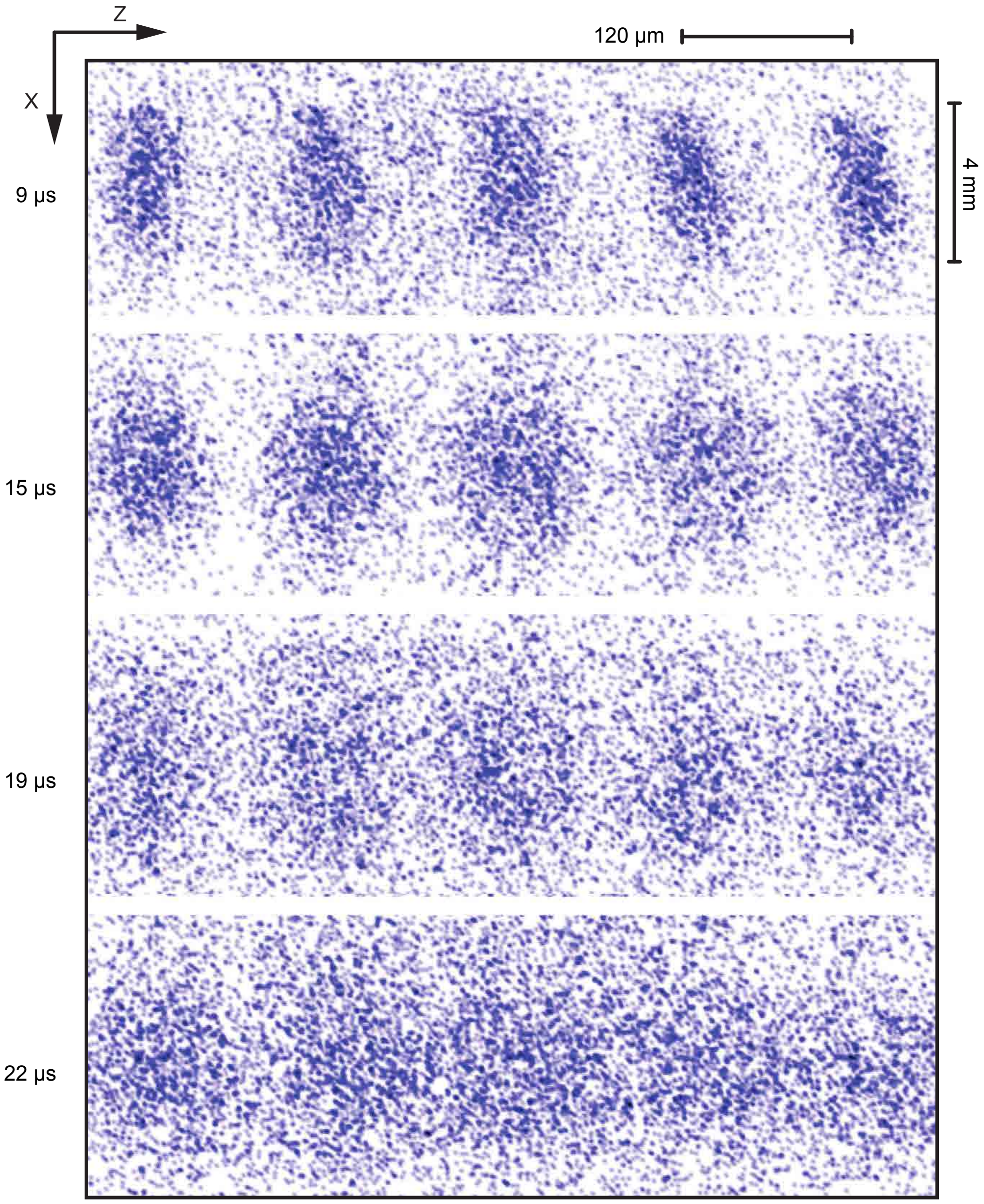

Figure 4.7: Two-dimensional spatial imaging of CO molecules. Molecules are imaged for different ballistic expansion times, making it possible to follow the evolution of the system.

the calculated speed distributions in the Y-Z plane, extracted from each simulation, are shown together with two-dimensional Maxwell-Boltzmann speed distributions, showing that the molecular clouds have a best-fit temperature of 11 ± 1 mK.

Ballistic Expansion Model

The method of ballistic expansion imaging is widely used in ultracold atom imaging to determine the temperature of a trapped sample. The density of atoms in a magnetic trap is high enough to assure thermalization, giving rise to a Maxwell-Boltzmann distribution of the velocities, represented by a Gaussian function. In the noninteracting ensemble of CO molecules used here, however, a Gaussian velocity distribution cannot be assumed *a priori*, but the analysis presented above suggests that a Gaussian distribution is nevertheless a fair approximation. Thus, the same analysis used for ultracold atoms is applied here to the cold molecules based on time-of-flight imaging. If the expansion of the atomic or molecular ensembles is dominated by the translational temperature, i.e., the velocity distribution of the particles, then the expansion can be described as [Weiss89]:

$$\sigma^2(t_\mathrm{b}) = \sigma_i^2 + \frac{k_B T}{m} t_\mathrm{b}^2, \tag{4.2}$$

where σ is the cloud standard deviation at ballistic expansion time t_b, σ_i is the initial cloud standard deviation, m is the mass of the particle and T is the temperature. This analysis functions on the premise that the clouds are Gaussian in form both in their position and velocity distributions [Weiss89]. However, Equation (4.2) remains a good approximation even in the case when the initial spatial distribution is not Gaussian, if $\sigma_i \ll \sigma(t_\mathrm{b})$, which is the case here. Each of the line profiles in Figure 4.8(a) is fitted with a sum of seven Gaussian functions, including the five clouds seen in the image and the contributions from their next-nearest neighbors on either side of the image. Using Equation (4.2), a least-squares fit is then carried out to $\sigma^2(t_\mathrm{b})$ against t_b^2 and a temperature of $T = 13 \pm 3.5$ mK is subsequently extracted, where the error is given here by the 95% (2σ) confidence bounds of the least-squares fit (see Figure 4.8(c)). The extracted temperature compares well with the 11 ± 1 mK found using trajectory simulations.

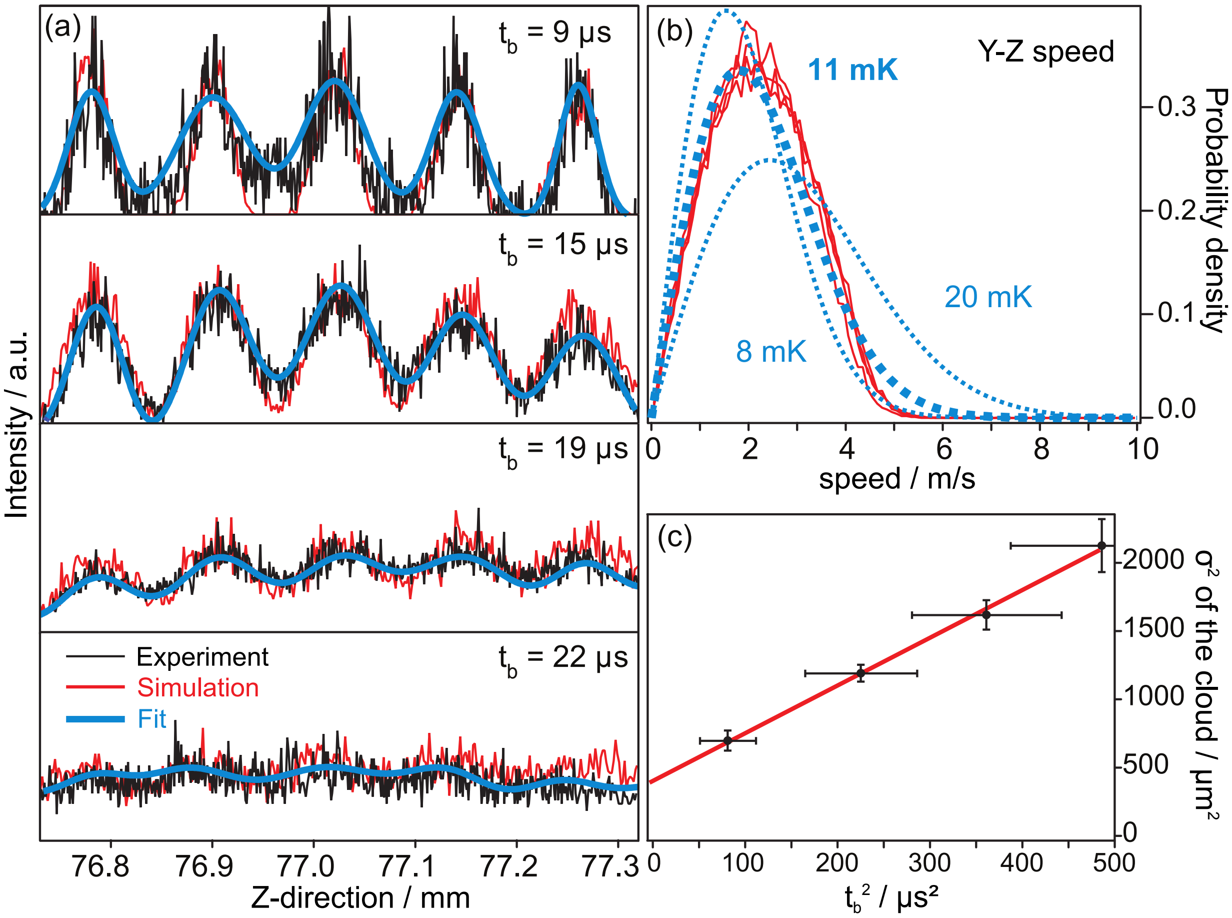

Figure 4.8: Analysis of different expansion times of molecule clouds. (a) Integrated line profiles (black) extracted from images (as in Figure 4.2) for various expansion times. For each expansion time, the blue line is the result of fitting a multi-Gaussian profile (see text for details), the red line is the result of trajectory simulations. (b) Speed distributions calculated from trajectory simulations for all four experimental conditions (red) and calculated Maxwell-Boltzmann distributions (blue), with the best fit given by a thick line. (c) The square of the mean Gaussian standard deviation from the fit in (a) plotted against the ballistic expansion time squared. The slope is proportional to the temperature of the gas (Equation 4.2).

4.4 Manipulation of the Temperature of Trapped Molecules

Potential developments for future molecule chips include the integration of, for example, optical traps [Padgett11], as well as cooling techniques to reach ultracold temperatures and the implementation of high-resolution spectroscopy. [Carr09] If the molecule chip were to be used as a molecular source for high-resolution spectroscopy, the molecules would need to be ejected at low velocity from the chip with a narrow velocity distribution so that the packet of molecules remains together for the longest possible time. [Quintero-Pérez13] Indeed this is one of the main goals of cold-molecule research. As a demonstration of the new on-chip detection system, it is now used to analyze the effect of a phase-space manipulation sequence to compress the velocity distribution without losing molecules.

To do this experimentally, molecules are captured and decelerated using waveforms with 200 V amplitude. Then, the amplitudes of the waveforms are linearly ramped down to 50 V in a time t_a, while guiding the molecules at constant velocity over the molecule chip surface. This procedure expands the volume of the traps in the Y- and Z-direction and the trap depth is lowered from 71 mK to 13 mK, leading to an adiabatic expansion of the trapped molecules on the chip. The manipulation scheme is explained in Figure 4.9.

Figure 4.10 shows integrated experimental imaging signals along with corresponding trajectory simulations for $t_\mathrm{a} = 0$, 10, 25, and 188 µs. The data show that the best-fit temperature is reduced from 16 mK to 5 mK for an expansion time $t_\mathrm{a} = 188$ µs (slow compared to the trap frequencies of hundreds of kHz). For shorter expansion times, however, cooling is less effective, as can be seen from Figure 4.10(b).

These claims stem from the results of trajectory simulations and are supported by the good agreement of the calculations with the experiments. Unfortunately, images were recorded only at a single ballistic expansion time ($t_\mathrm{b} = 15$ µs) and an accurate experimental determination of the translational temperature of the cloud is thus impossible for this set of measurements. However, the size of the cloud at the beginning of the expansion can be estimated and Equation 4.2 can be applied. Of course, such an approach is not a rigorous treatment and is only intended for showing the order of magnitude of the phenomenon. The results of this treatment are shown in Figure 4.10(c), where the translational temperature of the clouds is plotted against the estimated initial size of the clouds upon release from the traps. By assuming a σ_i^2 of approximately 400 µm^2 from Figure 4.8(c) it is found that this

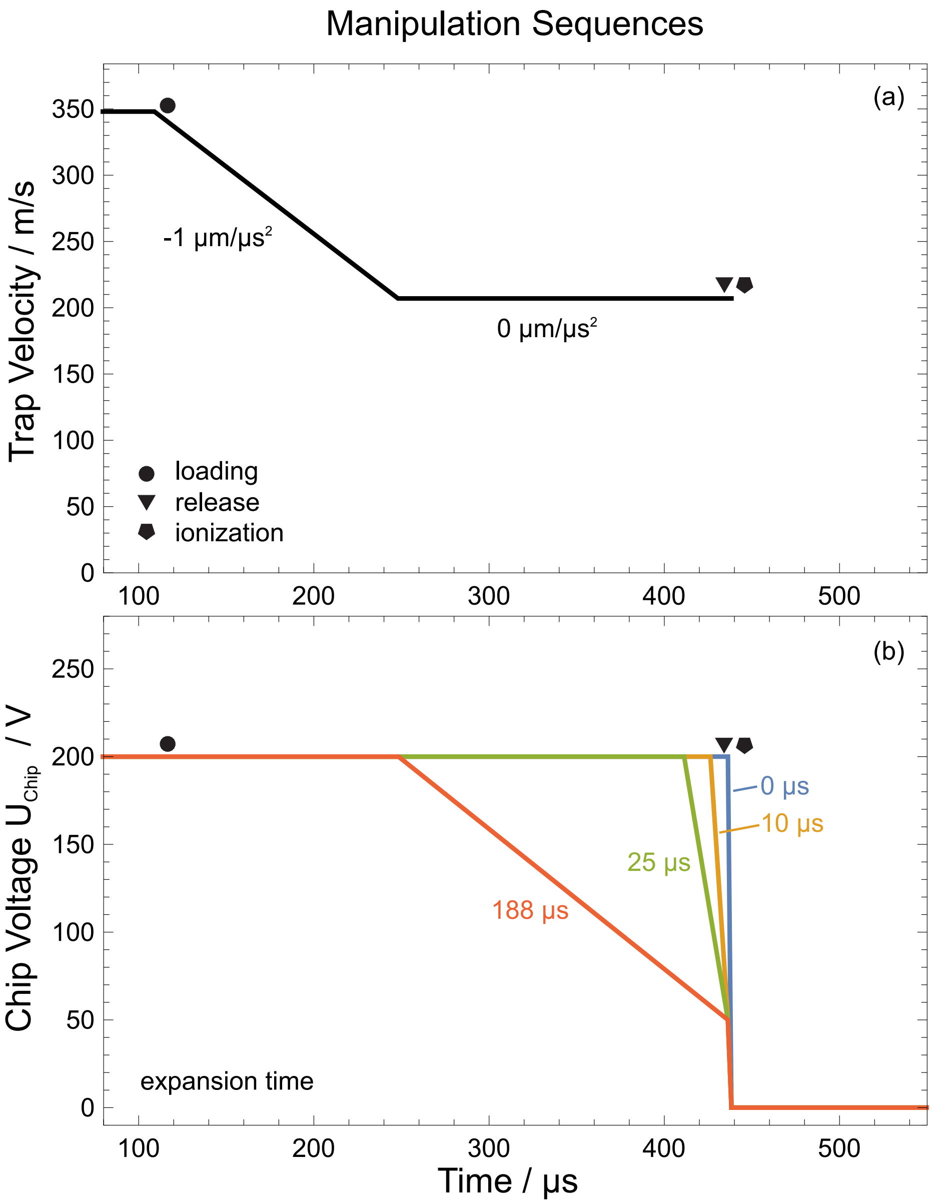

Figure 4.9: Manipulation scheme for adiabatic expansion of trapped molecules on the chip. Velocity of the traps (a) and voltages applied to the chip (b) as a function of time. The velocity scheme is the same for all measurements. Again, as before, the loading of the molecules on the chip (circles), the release at the end of the chip (triangles) and the ionization (pentagons) are marked. After deceleration, the molecule clouds are allowed to expand in the trap for a variable amount of time because the trap electric field gradient is reduced by lowering the chip voltage. This means a specific Stark energy is reached further away from the minimum, allowing the molecules with a given energy to reach positions further away from the minimum. The adiabatic expansion times are indicated in (b).

method overestimates the temperature with respect to trajectory simulations. However, trajectory simulations yield smaller values for σ_{i}^2 (shown as red circles in Figure 4.10(c)) which makes the discrepancy even larger.

The poor knowledge of the ballistic expansion time t_{b} is a possible explanation for such a discrepancy. t_{b} depends on the position of the ionization laser beam, which is difficult to measure. An offset of a few microseconds in t_{b}, corresponding to a spatial offset of the order of hundreds of microns, would be within the error bars of Figure 4.8 and would yield the dashed lines of Figure 4.10. Another possible explanation is that the molecules in the traps are simply slightly warmer than expected due to imperfections in the applied waveforms.

Model: Harmonic Potential

A simple way to rationalize the results of experiments and trajectory simulations is to approximate the trapping potential with a harmonic one, so that it becomes $U = k(Y^2 + Z^2)/2$. The lowering of the trapping potential for the adiabatic cooling corresponds therefore to a reduction of the initial k_{i} to a final k_{f}, which results in a reduction of the trap frequency $\omega = \sqrt{k/m}$, where m is the mass of a molecule. If the transformation is adiabatic, the total energy of the oscillator remains proportional to the frequency [Landau93]. Therefore, the final energy of the ensemble will be given by $\mathcal{E}_{\mathrm{f}} = \mathcal{E}_{\mathrm{i}}\,\omega_{\mathrm{f}}/\omega_{\mathrm{i}} = \mathcal{E}_{\mathrm{i}}\sqrt{k_{\mathrm{f}}/k_{\mathrm{i}}}$. Furthermore, if the system is treated quantum mechanically, the energy is given by $\mathcal{E} = (n + \frac{1}{2})\hbar\omega$ and the adiabaticity condition implies that each molecule remains in the same n-level during the process. This gives the same dependence of the energy change on the trapping potential as in the classical case.

As mentioned above, the microtrap potentials on the chip are only harmonic at the center of the microtrap. Therefore, the central 10 µm of the potential is taken, where the vast majority of molecules are situated, and fitted with a harmonic function $U = (k_Y Y^2 + k_Z Z^2)/2$. This gives a trapping frequency ω of approximately 1300 kHz at 200 V and approximately 500 kHz at 50 V, which leads to a reduction in temperature to approximately 40% of the initial temperature, i.e., from 16 mK to 6 mK. The main source of error in this treatment is the harmonic approximation of the trapping potential. Moreover, the rate of change of the trapping potential, and therefore of the trap frequency, must be slow enough for the process to be adiabatic: $d\omega/dt \ll \omega^2$. [Landau93] As the oscillation period is $\tau = 2\pi/\omega$, one can rewrite the adiabaticity condition as $d\tau/dt \ll 1$. In the above

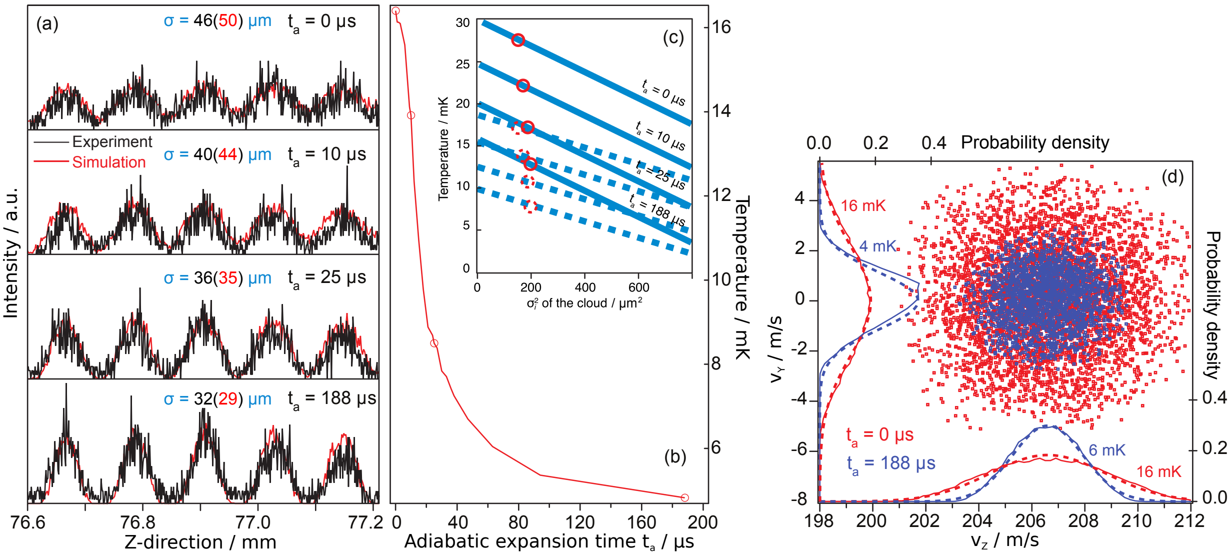

Figure 4.10: (a) Experimental integrated line profiles of molecules for various manipulation times, along with the corresponding numerical trajectory simulations. By fitting a multi-Gauss function to the experimental data, values of σ for all four measurements are obtained; the values for the calculated data are shown in parentheses. The relative uncertainty on the determination of σ is 10%. (b) Decrease in temperature with manipulation time from trajectory simulations. Circles denote the times for which experimental measurements were performed. (c) Translational temperature of the clouds for the different expansion times t_a as a function of the estimated initial cloud size, obtained from experimental data using Equation 4.2. The uncertainty due to the error in the determination of σ is represented by the thickness of the lines. Solid lines show the results for $t_\mathrm{b} = 15$ μs; dashed lines show the results for $t_\mathrm{b} = 18$ μs. The red circles show σ_i^2 from trajectory simulations. (d) Two-dimensional velocity distribution and projections. The distributions in the Y- and Z-direction after phase-space manipulation are different, showing that the phase-space manipulation does not act isotropically. Trajectory simulations (solid lines) and Maxwell-Boltzmann distributions for the best fit temperatures (dashed lines) are shown. Simulations show a number loss of approximately 5% during the phase-space manipulation.

mentioned case, the initial trap period was 0.8 µs (for 1300 kHz) and the final trap period was 2.0 µs (for 500 kHz). Taken simply as a change in trap period of $\Delta\tau = 1.2$ µs in the adiabatic expansion time of 10, 25, and 188 µs (Figure 4.10), leads to $\Delta\tau/\Delta t_{\mathrm{a}} = 0.1$, 0.05, and 0.007, respectively. One can see the validity of the adiabatic condition in Figure 4.10(b), where only in the latter case ($t_{\mathrm{a}} = 188$ µs), the temperature approaches the asymptotic limit, i.e., when $\Delta\tau/\Delta t_{\mathrm{a}} = 0.007$.

Model: Expansion of an Ideal Gas

The adiabatic expansion can be modeled in terms of an ideal gas as well. The adiabatic condition that PV^{γ} is constant and the ideal gas law $PV \propto T$ can be used to show that $TV^{\gamma-1}$ is also constant, where P is the pressure, V is the volume, T is the temperature and $\gamma = 1.67$ is the ratio of specific heats for an ideal gas. Knowing the initial temperature T_{i} and the ratio of the initial and final volumes $V_{\mathrm{i}}/V_{\mathrm{f}}$ would allow to calculate an estimate of the final temperature T_{f} after the adiabatic expansion.

To calculate the volume of the molecular ensemble one needs to consider the process of how the molecules are trapped and decelerated. The molecules are trapped by microtraps being already decelerating by -1 µm/µs^2, which have a depth of 46 mK to the saddle point of the potential at an electrode voltage amplitude of 200 V, less than their depth at a constant speed of 81 mK. The switch between deceleration and subsequent constant speed is instantaneous. Thus the volume of the decelerated trap is taken as the initial volume of the trapped molecule ensemble which is calculated to be $V_{\mathrm{i}} = 159$ µm^2 × 4 mm with an error of approximately 10%, given by how close spatially to the saddle point of the potential it is integrated. Subsequently, as long as the microtraps are moving at constant speed, the amplitude of the voltage applied to the electrodes is then decreased linearly to 50 V in the manipulation time t_{a} to achieve the adiabatic expansion. The final trap at 50 V has a saddle point at 13 mK. However, it is observed from the numerical trajectory simulations that few molecules are located near the saddle point of the trap, both for the 200 V trap under deceleration and for the 50 V trap under constant speed. In fact, as has been said before, a loss in the number of molecules of only approximately 5% is observed for the whole manipulation sequence, indicating that the molecules have insufficient time to find the saddle point and leave the trap, and hence are metastably trapped. To calculate a final volume V_{f}, therefore, the volume of the 50 V trap is taken up to the maximum possible energy of the molecules in the trap (46 mK), since these molecules have experienced the whole expansion sequence inside the trap, but with the constraint that any part of the volume situated spatially beyond the saddle point is excluded, since any molecules there would be ejected from the trap. In this way, a final volume of $V_\mathrm{f} = 1552\ \mu\mathrm{m}^2 \times 4$ mm can be estimated with an error of approximately 20%. Using the ideal gas equation given above, for the initial temperature $T_\mathrm{i} = 16$ mK (Figure 4.10(a)), this leads to a final temperature $T_\mathrm{f} = 3.5 \pm 0.8$ mK, a value within 2σ of that seen in the observations in Figure 4.10 (5 mK). It is stressed here that these calculations are very approximate, since it is difficult to precisely estimate the volume that the molecules explore in the trap. However, it is instructive to show that the ideal gas theory can be applied to model the adiabatic cooling process and give the correct order of magnitude for the final temperature of cold molecules in a single quantum state trapped and manipulated on the molecule chip.

4.5 Summary

With the ability to trap molecules [Meek09b], to manipulate their internal [Santambrogio11, Abel12b] and external [Meek08, Meek09a] degrees of freedom and now to produce time-resolved images with a fully integrated detection system [Marx13], the molecule chip is being developed into a complete toolkit for the investigation of cold molecular ensembles and a wide range of quantum phenomena and molecular processes.

The chief advantage of on-chip detection is the ability to probe the system at short evolution times. This allows for the detection of short-lived quantum states. Moreover, it maximizes spatial resolution and increases the signal-to-noise ratio, as it minimizes the ballistic expansion of the molecules on their way to an external detector. One of its main advantages is its general applicability, through the use of the REMPI process, making it not only quantum-state-selective, but applicable to virtually every molecule.

It was shown that this toolkit can be used to measure the temperature of the trapped molecules through ballistic time-of-flight imaging. Using a sequence of time-resolved images, the free expansion of the molecular ensemble was measured, from which a temperature was extracted using an analytical approach commonly used in the ultracold atom community. Numerical trajectory simulations were then used to show the validity of the analytical approach. The simulations offered deeper insight into the dynamics of the molecular ensemble and were subsequently used to investigate the effect of trap depth on the temperature of the molecules trapped on the molecule chip. This analysis allowed then to demonstrate that a phase-space manipulation scheme can significantly reduce the temperature of the trapped molecules, in this case to a third of its initial value.

CHAPTER 5

Ammonia

5.1 Introduction

The ammonia molecule (NH_3) has a wide range of applications and has played a key role in various scientific discoveries. Plants, for example, need a nitrogen source for their growth, but with rare exceptions they cannot make use of the bare N_2 molecule present in the atmosphere. Only a small class of plants can fixate free nitrogen thanks to symbiosis with bacteria at their roots. Fertilizers based on ammonia provide a nitrogen source that is usable by plants and consume approximately 80% of the industrial production of ammonia [Erisman08]. Moreover, ammonia plays a dominant role as a precursor for the production of other substances, such as explosives (nitroglycerin and TNT), is used as refrigerant due to its large heat of vaporization, and as cleaning substance.

On the scientific side, ammonia was the first molecule to be studied with microwave spectroscopy [Cleeton34]. The first maser, a coherent microwave source, was based on a beam of ammonia [Gordon54, Gordon55], and this achievement paved the way for the subsequent development of lasers, with their diverse applications. [Milonni10]

Its importance in the study of interstellar space is paramount. The molecule possesses many different transitions in the infrared and microwave region. The observed spectra of interstellar ammonia are rotational transitions from states that are excited by collisions with H_2. These transitions, which have spontaneous decay rates in the range between 10^{-2} and 10^{-9} Hz, provide information about interstellar densities on different time scales. Due to the broad frequency coverage it can be detected with telescopes in various spectral ranges. Furthermore, ammonia was the first polyatomic molecule detected in space. [Ho83]

Ammonia is used for the search for a possible variation of μ_{pe}, the proton-to-electron mass ratio. The analysis of the inversion line spectrum of ammonia is a very sensitive probe for the value of μ_{pe}. [vanVeldhoven04] The observation of molecular transition frequencies at significantly different times of the universe gives a constraint on the temporal variation of μ_{pe}, whereas observations from different sky directions probe for spatial variations. Moreover, measurements within our galaxy can test whether μ_{pe} depends on the local matter density. [Henkel12]

Large scale production of ammonia was made possible by Fritz Haber and Carl Bosch in the beginning of the 20th century via a process nowadays known as the Haber-Bosch process, which allows for the synthesis of ammonia directly from nitrogen and hydrogen. Fritz Haber was awarded the Nobel Prize in chemistry in 1918 “for the synthesis of ammonia from its elements”. Almost 90 years passed until the precise explanation of the catalytic reactions by Gerhard Ertl at the Fritz Haber Institute earned him a Nobel Prize in chemistry in 2007 [Ertl08]. It seems that ammonia is inseparable from to the FHI and, thus, I felt obliged to take the challenge upon me and try to trap it on the microchip.

Until now, only metastable CO has been trapped on the microchip. Trapping of ground state molecules with a large Stark effect, like ammonia, would allow to prolong the time available for experiments, perhaps up to many seconds. Interactions with the surface via black-body radiation or with induced dipole forces are interesting phenomena that could be studied with ammonia trapped on the chip. A cold, slow, and dense sample of ammonia molecules might be used in high-resolution spectroscopy experiments to search for the aforementioned possible change of the fundamental constants.

Ammonia has been decelerated before in conventional switched decelerators [Bethlem00] and in traveling-wave ring decelerators [Quintero-Pérez13]. Thus, the prospects for trapping ammonia on the chip were good. However, no evidence for trapping could be observed and this chapter will therefore present a negative result. Here, all experimental details are described and the cause of the difficulties with ammonia is identified in too large nonadiabatic losses.

5.2 Experiments

5.2.1 Spectroscopy

The REMPI spectrum of the $|\nu_{\mathrm{Inv}} = 1, J = 1, K = 1\rangle$ lfs state of ammonia is complex and for the detection of trappable lfs ammonia molecules in the experiment it is crucial to know which peaks actually correspond to this lfs level. Therefore, first, a REMPI spectrum was recorded with all electrodes of the chip grounded and the REMPI laser positioned a few mm after the chip. A sketch of the setup used for the spectroscopy experiments is shown in Figure 5.1. The data from spectroscopy are shown in Figure 5.2(a) and are compared with spectra measured by van Veldhoven et al. [vanVeldhoven06]. The spectrum shows a group of several peaks, which were assigned according to their transition from the ground to the intermediate state in the (2+1)REMPI process using information from References [vanVeldhoven06, Bertsche14, Bunker04]. The peaks match well with respect to their position and relative intensity. Five major peaks have been identified in the measurements originating from the $|\nu_{\mathrm{Inv}} = 1, J = 1, K = 1\rangle$ lfs state. Other peaks originate mainly from $|\nu_{\mathrm{Inv}} = 1, J = 1, K = 0\rangle$. The final states of the two-photon process are the lowest rotational levels of the $\widetilde{B}(\nu_2 = 5)$ excited vibronic state. Since the initial and final levels in the transition are connected with a two-photon process, the symmetry of both states needs to be the same. Therefore, the lfs states with E' symmetry in the ground state are only connected to states of E' symmetry in the excited state. The equivalent is true for the $K = 0$ levels of A1" symmetry.

In a second step, the ionization laser was slightly moved away from the center of the molecular beam, position [b] in Figure 5.1, and two more REMPI spectra were recorded in this configuration, Fig. 5.2(c). The first spectrum was recorded with positive and negative voltages applied to the electrodes on the chip in an alternating way (+100 V, −100 V, +100 V, ...), in order to create a mirror for molecules in lfs states [Schulz04]. At short distances from the chip surface, this voltage configuration produces an exponentially decreasing electric field strength. In contrast to lfs molecules, hfs would be attracted to the surface, whereas nfs molecules, such as the $K = 0$ states, are almost unaffected. As a reference, the other REMPI spectrum was recorded with all electrodes grounded. In part (d) of the figure, data from Reference [vanVeldhoven06] are plotted for comparison. In that work ammonia molecules in lfs states were focused with an electrostatic hexapole into the detection area, also increasing their relative signal compared to all other states. Be-

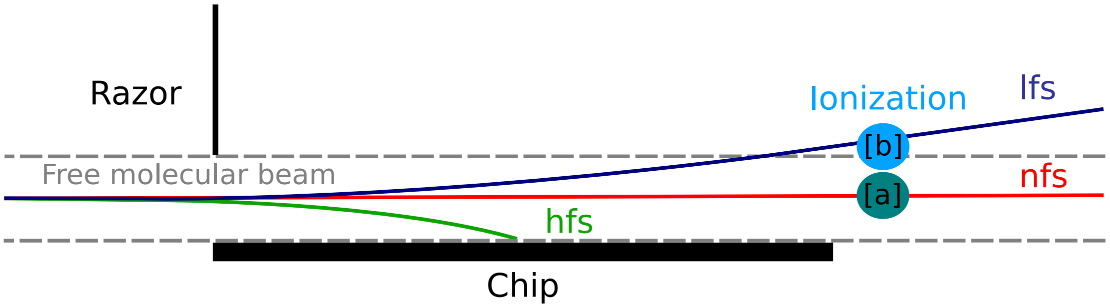

Figure 5.1: Setup for spectroscopy on $^{14}ND_3$. The molecules fly over the surface of the chip within the area labeled by “Free molecular beam” when the electric fields are switched off. The REMPI laser is positioned at [a] to record a normal spectrum. With the REMPI laser at position [b] the signal due to molecules in lfs states is enhanced when an alternating potential is applied to the microchip. This facilitates the assignment of the spectrum.

cause of the good agreement between the two different and independent measurements, the identification of transitions related to lfs states in the electronic ground state is considered reliable. Only the widths of the peaks are much different, which is a result of the details of the two setups. For further measurements of trapped molecules, the highest intensity lfs transition at 31511 cm^{-1} has been chosen for detection in the experiments.

5.2.2 Characterization of the Molecular Beam

The ammonia molecular beam was prepared by expanding a 20% mixture of ammonia in Xe through the pulsed valve. The backing pressure of the gas mixture was 2 bar and the valve was kept at a temperature of 203 K (see Section 2.3). For an accurate determination of the beam velocity several values need to be known: the position of the nozzle, the exact opening time of the valve, and the position of the detector, which in this case is given by the ionizing laser beam. The measurement of these three values is not trivial. However, the chip allows for a simple and accurate method to calibrate the measurement of the beam velocity, if it is used to guide the molecules at a given velocity. From the chip geometry and the frequency of the applied waveforms, the velocity of the moving microtraps is known very accurately. Thus, the measurement of a group of molecules that are guided at a defined speed calibrates the setup.

A beam of CO molecules was produced originating from a similar 20% mixture of CO in Xe, kept at the same backing pressure and temperature, to calibrate the setup. By the

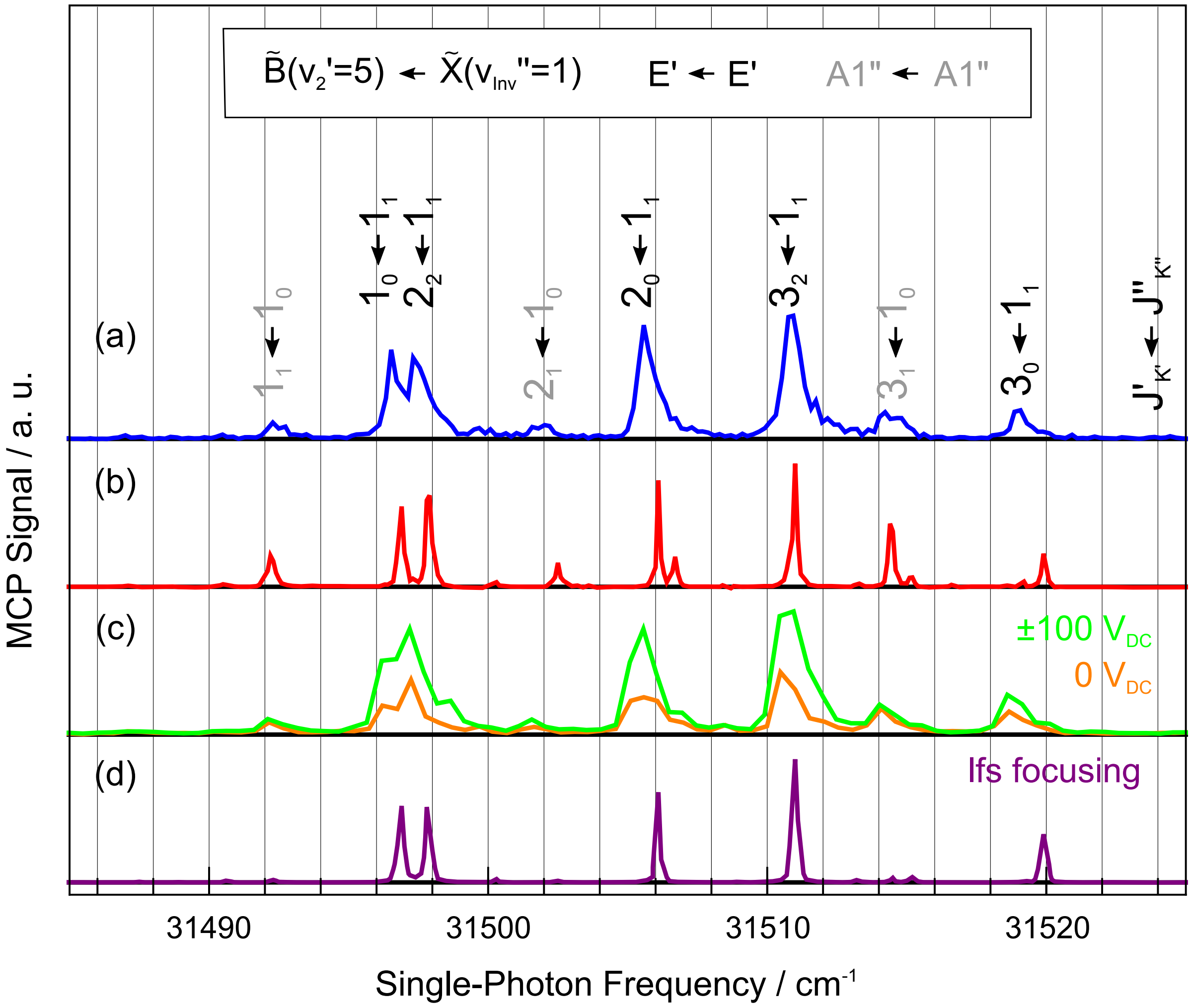

Figure 5.2: Spectroscopy of $^{14}ND_3$. (a) Ammonia REMPI spectrum on the free molecular beam. (b) Data from Reference [vanVeldhoven06] for comparison. (c) REMPI spectrum with displaced laser position. The spectrum recorded with alternating DC voltages applied to the chip is plotted in green, while the spectrum with no voltages is plotted in orange. (d) Reference measurement for the determination of transitions originating from lfs states, the data is taken from Reference [vanVeldhoven06]. The frequency of the lines with increased intensity in the measurements with ± 100 V_{DC} in (c) and the peaks from the reference measurement in (d) match well, indicating transitions originating from molecules in lfs states. Selection rules for this (2+1)REMPI transition are $\widetilde{B}(\nu_2 = \text{odd}) \leftarrow \widetilde{X}(\nu_{\text{Inv}} = 1)$, $\Delta J = 0, \pm 1, \pm 2$, $\Delta K = \pm 1$, while the rovibronic symmetry stays the same (E'←E', A1"←A1"). [Schleipen92]

time the molecules arrive at the chip, the forward velocity and position are correlated, because the faster and the slower molecules had enough time so separate in space. This implies that only molecules with a particular velocity reach the chip entrance (and later the detector) at a given time. As a result, the velocity and its spread can be extracted from measured beam profiles. The arrival time profile of the CO molecular beam is shown in Figure 5.3(a), having a mean speed of 342 m/s, with a FWHM of approximately 15 m/s. This is known from the arrival time profiles of guided CO molecules. Guiding is shown for 336 m/s together with a background measurement (240 m/s) below the curve of the free molecular beam.

The ammonia beam profile in time is shown in Figure 5.3(b). The temporal distribution of the ammonia molecules is much broader than for CO, which is the result from detecting ground state ammonia molecules instead of the laser-excited metastable CO molecules. The metastable CO molecules represent only a fraction of the ground state distribution because of the small laser volume in which ground state CO molecules are pumped to the excited metastable state. Despite the difference in width, the curves from the free molecular beams have a similar mean velocity, which is the result of the similar mass of the mixtures. The ammonia beam is found to have a mean velocity of 318 m/s and a HWHM on the lower velocity side of approximately 50 m/s. The guiding curve in the figure shows the signal when guiding with 312 m/s, whose expected guiding peak position is indicated with an arrow.

5.2.3 Efforts to Trap Ammonia

Trying to trap and guide ammonia on the chip, the guiding speed was varied in a large range between 180–330 m/s and the detection time was adapted correspondingly; moreover, a series of detection timings was always tried to account for possible errors in the determination of the distances of the molecular beam. However, no signal was measured that can be attributed to trapping and guiding of ammonia. A large velocity range was tried because of the wide velocity distribution of the ammonia beam. Moreover, in another attempt, an appropriate deceleration of the trapped molecules was applied to separate them from the free beam. This reduces the background signal at the cost of a lower number of trapped molecules. It was not clear whether such an experiment would improve the signal-to-noise ratio, because it is hard to do predictions for an experiment that is not working, but is was

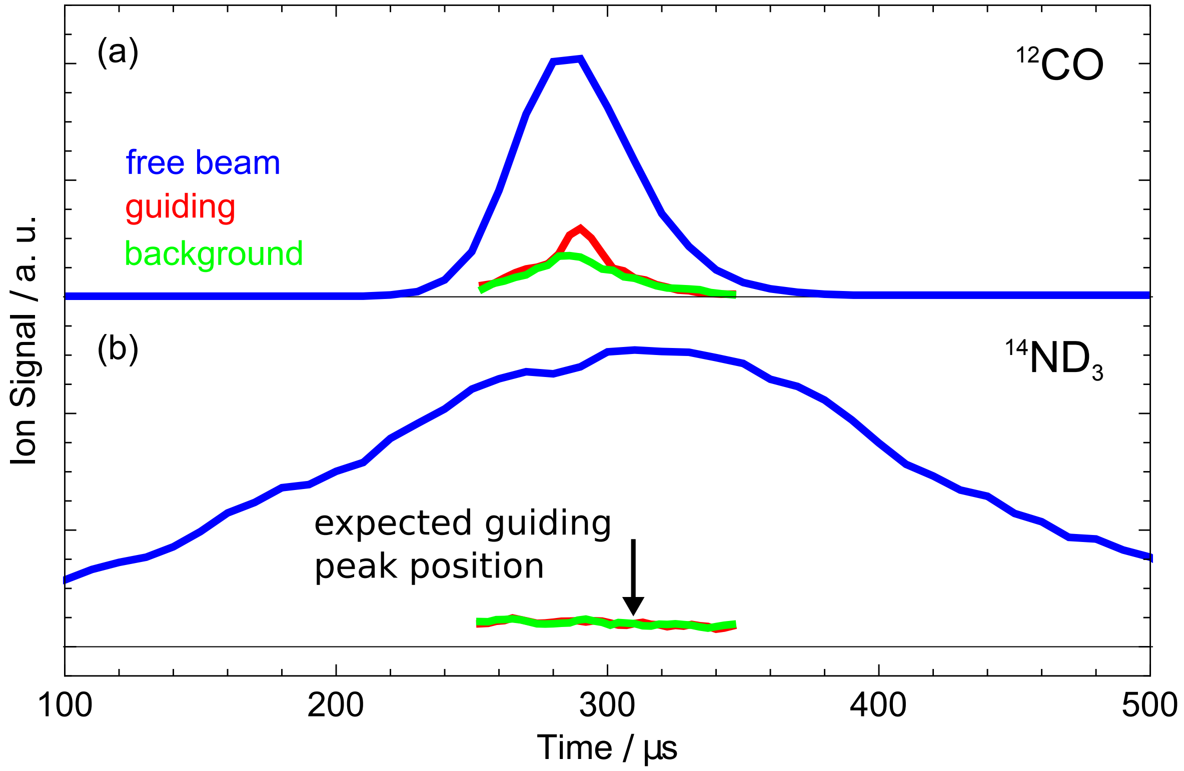

Figure 5.3: Time-of-flight profiles of CO and ND_3 molecular beams. (a) CO free beam and guiding signal. The guided molecules are visible as the difference between the guiding (red) and the background curve (green). Guiding was done at 336 m/s. To measure the background, a guiding speed of 240 m/s was used. (b) The equivalent measurement for $^{14}ND_3$. Guiding is tried at 312 m/s and the expected arrival time is indicated by the arrow. Uncertainty in the laser position (less than 3 mm) translate to an uncertainty of less than 10 µs in the arrival time, which is covered by the measured data.

tried nonetheless.

A further issue with the detection of trapped ammonia molecules is arising from the poor spatial overlap between the molecule packets and the laser spot size. The trapped molecules fill many traps, which together occupy a few millimeters. Yet a (2+1)REMPI process requires a large fluence to guarantee a good efficiency for the two-photon process, so the laser beam is tightly focussed to a 10 µm spot-size. To reduce this size mismatch space-bunching acceleration sequences [Meek10] were tried. Unfortunately, none of these methods lead to the detection of trapped ammonia molecules. All experiments were repeated for $^{14}NH_3$, $^{14}ND_3$, and $^{15}ND_3$.

5.3 Nonadiabatic Transitions

The adiabatic theorem of quantum mechanics states that if one enumerates the energy eigenstates of a quantum mechanical system in order of increasing or decreasing energy, and the system is initially found in the nth eigenstate, the system will remain in the nth state during an adiabatic process, i.e., a process in which the Hamiltonian changes "sufficiently slowly". [Born27, Born28] The energy eigenstates of the trapped polar molecules on the chip are such a quantum mechanical system. The description of their eigenstates is based on the approximation that the energy of a polar molecule in an electric field depends only on the electric field strength, which is usually a good approximation, so $U \approx U(|\vec{E}|)$. This is justified because the orientation of the molecules in space follows the direction of the electric field adiabatically around in the trap, if the field changes "slowly enough". These adiabatic states can be quantized along the field vector and are assigned a projection quantum number M. However, this approximation breaks down if the field vector changes too quickly. In this case nonadiabatic transitions to other M-states can occur. Therefore, additional interaction terms need to be considered in the potential $U = U(|\vec{E}|) + \Delta U(\partial \vec{E}/\partial t) + \dots$ for the complete description.

The probability of a nonadiabatic transition to happen between two levels is related to the ratio of the rate of electric field change $f_{\vec{E}}$, in magnitude or direction, to the frequency separation between these levels $f_{\mathcal{E}} = \Delta\mathcal{E}/h$. The probability is significantly high if $f_{\vec{E}} \gtrsim f_{\mathcal{E}}$. If the change in electric field is too fast, the molecules experience an electric field with spectral components able to drive the aforementioned transitions. For trapped molecules in lfs states, this is particularly problematic if the new state is not or only weakly lfs, because molecules will be lost from the trap.

The equivalent effect for atoms in magnetic traps is known as Majorana or spin-flip transitions. Both the Majorana transitions for atoms trapped in magnetic quadrupole traps [Petrich95] and the nonadiabatic transitions in molecules trapped in electric quadrupole traps [Kirste09] have been studied. The trap losses can be significantly reduced by increasing the spacing between levels $\Delta\mathcal{E}$ or by preventing the particles to encounter these rapidly changing fields. One relatively simple solution is to add an offset magnetic field [Fortàgh07] or an offset electric field [Kirste09] to raise the minimum energy difference from the trappable to the other states. For the chip this is difficult, however, because at the position of the traps, close to the surface, an external electric offset field will be screened by the metallic electrodes generating the trap.

The level splitting, and therefore $\Delta\mathcal{E}$, can also be increased in ^{12}CO by applying a magnetic field in addition to the electric trapping fields, which again leads to a reduced loss rate [Meek11b]. For ^{14}ND$_3$ in the electronic ground state $\widetilde{X}$, however, the spin is 0 and the effective magnetic moment will not have components from electrons. Neglecting hyperfine structure, which is on the order of a few MHz in ^{14}ND$_3$ at zero field [vanVeldhoven06], the Zeeman effect of a symmetric top molecule can be expressed according to [Kukolich73] as

$$\mathcal{E}_{\text{Zeeman}}(J,K,M) = -\mu_{\text{N}} g(J,K) M H - \frac{\chi(J,K) H^2 (3M^2 - J(J+1))}{3(2J-1)(2J+3)}, \tag{5.1}$$

with $g(J,K) \approx 0.5$ and $\chi(J,K) \approx 10^{-5}$ J/T^2/mol ≈ 25 kHz/T^2. [Hüttner74] The second term can be neglected if $H \ll 100$ T, and then the splitting scales roughly with the nuclear magneton $\mu_{\text{N}} \approx$7.6 MHz/T. The approximately 23 MHz splitting formerly used to suppress nonadiabatic transitions in trapped ^{12}CO [Meek11b] was achieved by using an $H = 5$ mT field. This was possible because the splitting of electronically excited CO scales roughly with the Bohr magneton $\mu_{\text{B}} \approx 14$ GHz/T $\approx 2 \cdot 10^3 \mu_{\text{N}}$ due to the contributions from the electron (L and S) to the magnetic moment. For ^{14}ND$_3$, however, only energy shifts much below 1 MHz are achievable with reasonably accessible magnetic fields, which is not expected to significantly suppress nonadiabatic losses from the microtraps.

Instead of changing the trapping field with offset fields, also the energy difference to other states ($\Delta\mathcal{E}$) can be changed directly by taking advantage of isotopic effects. For ammonia, the isotopologue ^{14}ND$_3$ shows a larger level spacing at low field strengths as compared to the ^{15}ND$_3$ version and also shows a longer trapping time [Kirste09]. Equivalently, by using the ^{13}CO instead of the ^{12}CO isotopologue, the energy separation between trapped and untrapped states at vanishing electric field is raised from zero to approximately 50 MHz, which reduces the likelihood of a transition and therefore increases trapping time. [Meek11b]

Since the likelihood of nonadiabatic transitions is determined from the ratio of the frequency of the electric field change $f_{\vec{E}}$ to the frequency associated with the energy difference to other states $f_{\mathcal{E}}$, a low likelihood can also be achieved by lowering $f_{\vec{E}}$ instead of acting on the energy difference. In a static, non-moving trap, the rate is determined from the electric field gradient of the trap and the velocity of the molecule. Since the traps on the molecule chip are generated from the difference of two fields, which change due to imperfections of the applied waveforms, the trap minimum will jitter around. This jittering can be much faster than the molecular motion and leads to a quickly moving trap which increases the rate of change of the electric field experienced by the molecules. Moreover, the "dangerous" area close to the minimum is effectively increased and more molecules will be exposed to the problematic conditions there. An attempt to reduce the imperfections of the waveforms showed that indeed the nonadiabatic transitions can be reduced. A reduction in anharmonicity of these waveforms from 7% to 3% showed that for CO the loss rate was reduced by 10%. [Meek11b] Improving the waveforms much further is in general a difficult task, because waveforms in the range of 3 MHz down to DC are needed with an amplitude of 200 V.

In the case of CO, a thorough analysis of the nonadiabatic losses from the chip and their prevention has been made [Meek11b]. For ammonia no such study is available, and an experimental comparison between nonadiabatic transitions in ammonia and CO has not been performed. The frequency of nonadiabatic losses from an electrostatic trap for ammonia with the diameter of approximately 2 mm has been quantified to be on the order of 1 Hz. [Kirste09] Since the frequency of the transitions scales quadratically with distance from the electric field minimum [Kirste09], and the diameter of the microtraps is reduced to approximately 1% (20 µm) of the diameter of the former trap, the loss rate on the chip is expected to be on the order of 10 kHz. This amounts to the loss of approximately 90% of the trapped molecules over the roughly 200 µs of the guiding experiments. A signal originating from 10% of the molecules that are loaded into the microtraps arises no particular concern. This result, however, does not take the trap jitter into account, which is known to be the most critical aspect in the chip setup. At the beginning of this project, it was believed that a measurable signal would be available despite these losses.

Of course, it would be desirable to extend the analysis carried out for CO to ammonia, but without a measurable signal to start with this is a great challenge. Therefore, in a set of experiments aimed at tracking the loss of molecules from trappable states, the traps were switched on only for a short time period when the molecules approach the end of the microstructure. Trapping times as short as a few µs were tried. It was expected that while the broad distribution of free-flying molecules was progressively suppressed with increasing trapping time, a sharp feature due to guided molecules would appear in the recorded signal, which would be reduced for longer trapping times due to nonadiabatic transitions. This effect could be observed for ^{12}CO but unfortunately no condition was found for which such result could be obtained for ammonia.

5.3.1 Chip with Offset Electric Field

Since an offset magnetic field is not helpful to reduce nonadiabatic transitions in ammonia, an additional electric field is considered here. In particular an electric field perpendicular to the plane of the trapping field vectors is studied. The main difficulty arises because the metallic electrodes of the chip shield the field components parallel to their surface.

Design

The setup designed to apply this additional electric field is shown in Figure 5.4. On the two sides of the chip along the X-direction, metallic plates are mounted. A positive voltage is applied to one of the electrodes and a negative voltage to the other. Thus the chip is in a parallel-plate capacitor field, which is relatively homogeneous between the plates. The plates have a length of 89 mm, a height of 25 mm, are 0.5 mm thick and are separated by 50 mm. Voltages of up to ±4.5 kV can be applied in the current setup without electric breakdowns. Since metallic parts between the plates would further complicate the electric field, the metallic razors and razor holders at the beginning and end of the chip have been exchanged with nonmetallic versions. The 6 clamps bringing the voltage to the chip pads have been redesigned to have a minimal amount of material between the traps and the capacitor plates. The six groups of microelectrodes are connected with buses running along the Z-direction. These buses are slightly higher than the center of the microtraps above the chip surface, extending over the glass surface up to approximately $Y = 35$ µm. To try to reduce the possible shielding of these metallic buses and the shielding of the

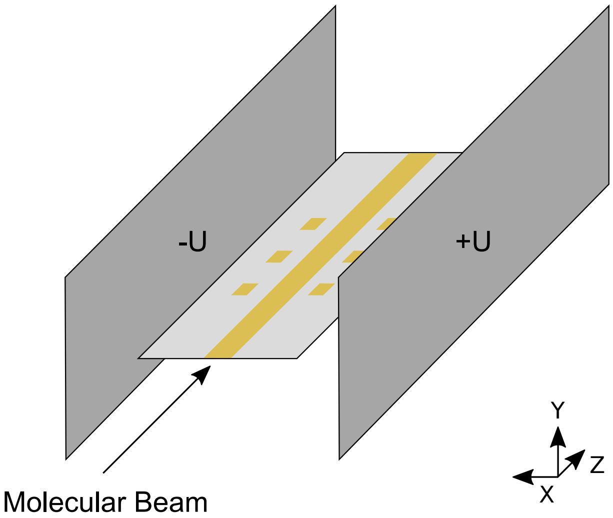

Figure 5.4: Molecule chip between two metallic plates to apply an additional electric field along the X-direction. The TOF detection setup at the end of the chip has been omitted for simplicity.

microelectrodes the parallel plates can be tilted around the Z-direction by 0, 2 or 10 degrees.

Simulation of the Electric Field

With this capacitor an additional electric field is created over the chip along the X-direction. The voltages are applied symmetrically on the plates ($+U$ on one plate, $-U$ on the other). Since electric components between the two capacitor plates will distort the homogeneous electric field, the presence of the metallic electrodes has to be included in the simulation. To evaluate the electrostatic field in the region of the traps, a three-dimensional unit cell of the electrode array is simulated, which comprises one electrode. To include the effect of neighboring electrodes periodic boundary conditions along the Z-direction are applied. The unit cell is chosen to be 12 mm × 6 mm × 40 µm (in X, Y, and Z). The electrode is 4 mm long ($X = -2 \ldots 2$ mm), 1.5 µm high ($Y = -1.5 \ldots 0$ µm), 10 µm wide and centered in the unit cell ($Z = -5 \ldots 5$ µm). The periodicity is 40 µm along Z. The metallic plates at the two sides along X create a field of 1.8 kV/cm (using ±4.5 kV) if no chip with electrodes is inserted between them; the chip electrode itself is grounded.

The results of this simulation can be seen in Figure 5.5. Generally, only the X-component of the electric field is considered because this is the important field axis in this case.

Other components only shift the trap around on the Y-Z plane. Figure (a) shows the magnitude of the X-component of the electric field on the $Z = 0$ µm plane (centered on a microelectrode). The electrode itself cannot be seen because it is too thin on the chosen scale. The grounded electrode will be polarized in the field, leading to two spots with very high electric field strength at the electrode's ends. The field between the electrode's ends is reduced, approaching zero close to the surface. Far from the electrode the field approaches the 1.8 kV/cm field strength, which would be present without the electrode. The color-coded range is clipped at 3 kV/cm to increase the visibility of areas with low field strength. Figure (b) shows the electric field along the molecular beam axis Z, centered on the electrode (at $X = 0$ mm) for different heights, chosen to be close to the trap height ($Y \approx 19 \ldots 45$ µm). Close to the electrode the shielding of the electric field is strongest, as can be seen especially for the 0 µm curve by a reduction to 0 kV/cm. The field is approximately homogeneous along the Z-direction in the region where molecules fly and it amounts to 0.02–0.04 kV/cm. Figure (c) shows the distribution along the electrode axis, X. In the central part of the electrode ($X = -1 \ldots 1$ mm) the field is relatively constant; further outside it rises quickly. At $X = \pm 1$ mm the field has increased to approximately 0.038–0.076 kV/cm, at $X = \pm 1.5$ mm it has increased to 0.085–0.17 kV/cm. Figure (d) shows the distribution along the axis normal to the chip surface (Y). Along this direction the field is almost linearly increasing with increasing distance from the surfaces for the region where the traps are.

In conclusion, the electric field of 1.8 kV/cm, created with plate voltages of ±4.5 kV, is strongly reduced by the microelectrode to values of approximately 1–10% (0.024–0.17 kV/cm) for most of the molecules that are within 75% of trap length, between $X = \pm 1.5$ mm. Since the normal trap electric field (0–5.6 kV/cm) created by the microelectrodes quickly dominates the additional field when moving away from the trap center, the additional field is important only at the trap center around its 0 kV/cm field minimum. There, at approximately 25 µm height, the field strength is increased to approximately 0.03–0.11 kV/cm (for positions X between ±1.5 mm).

Energetic Splitting

Using the precise energy level calculations performed in Reference [Kirste09] for ammonia in low electric fields, the energetic splitting can be accurately determined. They are shown in Figure 5.6 for three ammonia isotopologues. These calculations include hyperfine splittings

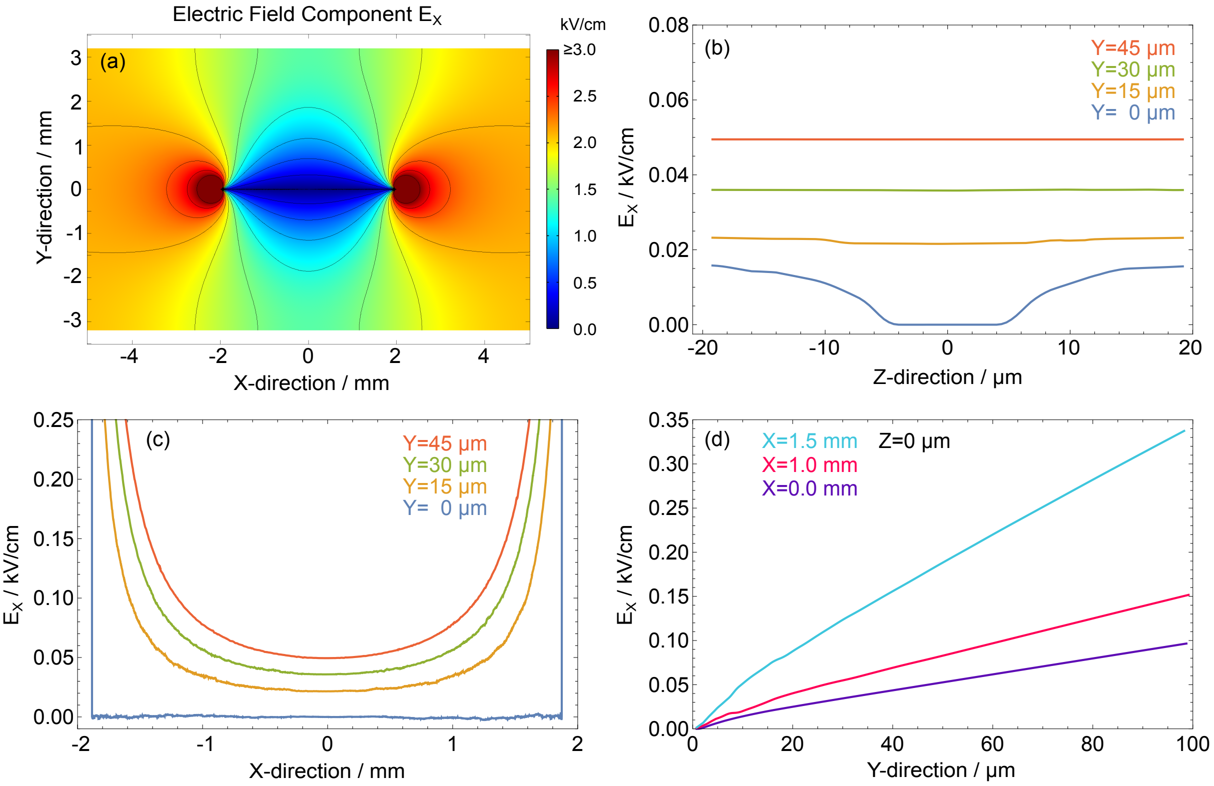

Figure 5.5: Electric field distribution E_X around a microelectrode when the chip is placed between two parallel plates. The electric field without the chip would have a homogeneous magnitude of 1.8 kV/cm. The microelectrode extends between $X = -2 \ldots 2$ mm, $Z = -5 \ldots 5$ µm, and its upper surface is found at $Y = 0$ mm. (a) Electric field strength on the $Z = 0$ µm center-plane. The electric field is low around the electrode, except for the regions at the two ends. (b) Field along the Z-direction for different heights Y above the electrode surface. It is relatively homogeneous, except very close to the surface (below the trap region of $Y \approx 19 \ldots 45$ µm). (c) Field along the X-direction for the same heights above the surface as in (b). (d) Electric field along the Y-direction for different positions along the electrode axis X.

of the $|\nu_{\mathrm{Inv}} = 1, J = 1, K = 1\rangle$ energy levels due to the presence of an electric quadrupole moment of the ^{14}N nucleus (the splitting in three groups labeled with the quantum number $F_1 = I_{\mathrm{N}} + J$ due to the nonzero quantum number I_{N}) and due to the spins S of the hydrogen atoms (the smaller splittings; $S = 1$ for deuterium and $S = 1/2$ for each of the hydrogen atoms H). In general the behavior of the energy levels in an electric field is complex because of the many different states with their individual hyperfine splittings. However, certain groups can be identified which behave rather similarly. They have been labeled by roman numbers and are discussed below. The additional field experienced by the trapped molecules E_{X}, which is shown in Figure 5.5, is roughly on the order of 0.02–0.2 kV/cm over the trap area. In particular, at the center of the trap it shifts up the minimum field from 0 kV/cm to 0.03–0.11 kV/cm as has been mentioned earlier.

For ^{14}ND$_3$ shown in figure (a), at low field strength the splitting due to the quadrupole moment is dominating, which is approximately 0.63 MHz between the $F_1 = 1$ and the $F_1 = 2$ states. For the majority of lfs levels (the $F_1 = 1$ group or “I”), the splitting to the nearest nfs levels of group III amounts to approximately 0.63–1.7 MHz for the fields of 0.03–0.11 kV/cm. Group II lfs levels have a splitting of up to approximately 1.4 MHz to group III nfs. Unfortunately, for molecules in group I the levels of group II are separated by only 0.3 MHz, which come even closer to the nfs levels at low fields.

For ^{15}ND$_3$ shown in figure (b), a nuclear quadrupole moment is missing, leading to a much closer approach of the lfs (group I) to the nfs states (group II) at low field. At 0 kV/cm the energy separation between the different levels are on the order of 0.1–0.2 MHz, which is increased to approximately 1.2 MHz (0.11 kV/cm).

In figure (c) the situation is shown for ^{14}NH$_3$. The splittings in low electric fields is similar to the situation of ^{14}ND$_3$, except for its lower Stark effect due to the larger inversion splitting and that it is less complex because of the lower spin of hydrogen atoms compared to that of the deuterium atoms. An energy splitting between the F_1 and F_2 lfs and nfs is dominated by the quadrupole splitting of approximately 0.6 MHz, which is not changing much up to the 0.11 kV/cm field present closer to the edges of the electrodes.

These increased splittings seem not to be significantly large to suppress nonadiabatic transitions from lfs to nfs in any of the discussed isotopologues.

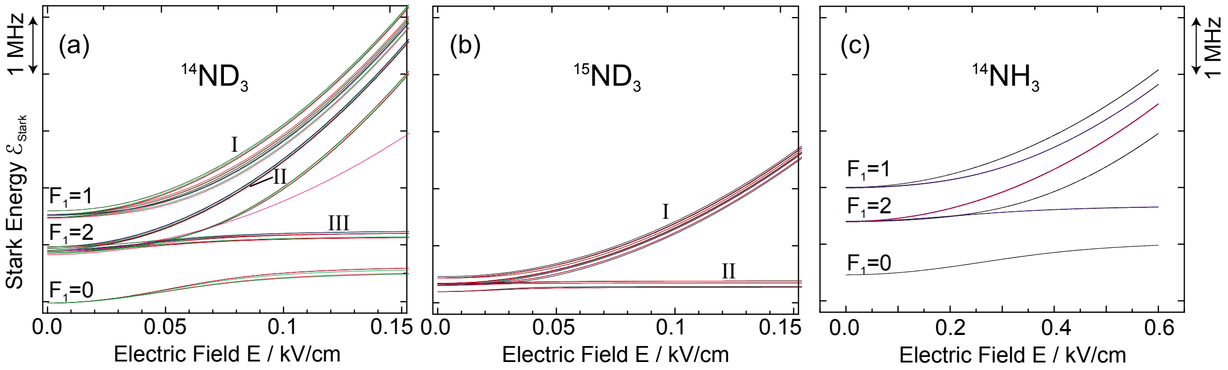

Figure 5.6: Stark effect of the ground state $|\nu_{\rm Inv} = 1, J = 1, K = 1\rangle$ of different ammonia isotopologues in a low electric field. The presence of an electric quadrupole moment of the ^{14}N nucleus (leading to a nuclear spin $I_{\rm N}$) causes the observed splitting in three main groups, labeled with the quantum number $F_1 = I_{\rm N} + J$. Smaller splittings occur due to the presence of the nuclear spins of the hydrogen and deuterium atoms. Note that the electric field range is larger in figure (c). The data is taken from Reference [Kirste09].

5.3.2 Experimental Tests

On the capacitor plates voltages up to ±4.5 kV were applied, leading to energy splittings between lfs and nfs of up to 1.7 MHz for the majority of trapped molecules (75% of trap volume), as has been described above. No signal could be observed using the different isotopologues. Also various combinations of tilting of the capacitor plates, guiding, deceleration and reduced trapping time were performed. To exclude a possible charging of the chip dielectric, the capacitor plates were turned on only for the time the molecules were above the chip.

5.3.3 Other Possible Loss Mechanisms

The density of the molecular beam is similar for ammonia and for CO, as is their collision cross section with background gas. Transitions induced by blackbody radiation at 295 K from the $|J = 1, K = 1\rangle$ state of ^{14}ND$_3$ (^{14}NH$_3$) have a rate of 0.23 Hz (0.14 Hz) [Hoekstra07], much too low to be relevant in these experiments.

In principle, long-range interactions of molecules with fluctuating fields from a thermal surface might lead to heating and therefore to trap losses. For atoms and ions this effect has been investigated [Henkel99]. It was found that for ions above a metal surface the effect is particularly large and gives rise to a transition rate on the order of 1 Hz for distances of approximately 10 µm to the surface. Since the molecules will not get closer than 20 µm to the chip surface and the neutral dipolar molecules are expected to interact much less with the surface than ions, this effect should not be relevant here either.

5.4 Summary & Conclusion

Trapping ammonia molecules on a chip would extend the capabilities of the chip due to longer trapping and manipulation times. Calculations of the effective trap depth for ammonia molecules (Chapter 2) show that the trap depth is comparable to the case of CO. However, no experimental evidence could be obtained for the trapping of ammonia on the chip.

The detection method has been tested and compared with data from other sources and no significant deviations were found. Techniques other than pure guiding were employed, such as decelerating molecules to regions with less background signal or spatially bunching them to increase the signal-to-noise ratio at the detector. The failure is attributed to nonadiabatic transitions from trappable to non-trappable states. Approaches to reduce their extent with magnetic or electric fields, which have been shown to work in other setups for molecules, cannot be done on the chip in a similar way. Magnetic fields on the order of hundreds of Gauss, which one could implement in the present setup, do not yield a sufficient splitting to suppress the losses. Electric fields are suppressed over the metallic electrodes, leading to energy splittings only up to at most a few MHz, which appear not to suffice to observe even a small signal which could then be used to optimize the trapping efficiency.

CHAPTER 6

A Ring Decelerator on a Chip

6.1 Introduction

The invention of the Stark decelerator [Bethlem99] opened up a new way of producing slow and cold samples of molecules and enabled a variety of applications. Due to the low achievable molecular velocities the interaction times of decelerated molecules with a radiation field are increased, enabling high-resolution spectroscopy [vanVeldhoven04, Hudson06] since the interaction time is fundamentally limiting the obtainable energy resolution in such spectra. With the ability of tuning the velocity over a large range with a Stark decelerator, quantum state selective inelastic collision studies can be performed, e.g., by scattering OH and Xe and thereby resolving the excitation of rotational transitions in OH. [Gilijamse06] The deceleration of polar molecules and their subsequent electrostatic trapping allows one to observe the decay of the number of trapped molecules and thereby to measure the lifetime of the trapped molecules directly. [vandeMeerakker05, Gilijamse07]

The operation principle of this first-generation Stark decelerator is based on the switching of high electric fields at fixed positions along the molecular beam. When the trapping and deceleration is performed only at these discrete points along the molecular beam axis, the trapping potential is not truly three-dimensional. This leads to trap loss predominantly at low molecule velocities, even though improvements were presented using a new quadrupolar decelerator design. [Sawyer08]

In 2010, a different type of Stark decelerator was presented that confines the molecules in truly three-dimensional potential wells at all times, also for low velocities, referred to as *traveling-wave ring decelerator* [Osterwalder10, Meek11a]. It shares basic operation principles with the Stark decelerator on a chip [Meek08] which has been used so far in this thesis. Heavy molecules like YbF are particularly interesting for high-resolution spectroscopy because they are excellent systems for looking for an electric dipole moment of the electron. However, their lfs states turn hfs at relatively low electric field strength. But in the travelling wave decelerators molecules are always close to the field minimum, thus experiencing lower electric field strengths than with first-generation decelerators. Deceleration of heavier molecules like YbF [Bulleid12] and SrF [vandenBerg14] has been demonstrated with these traveling-wave ring decelerators.

Commercially available high voltage amplifiers which are used to create the electric fields for trapping (like the commonly used Trek Model 5/80 [Quintero-Pérez13, vandenBerg14]) offer a useful waveform bandwidth on the order of 30 kHz–DC, which is sufficient to capture molecules directly from a 300 m/s molecular beam. The voltage amplitude, and therefore the trap depth and maximal acceleration, is restricted to ±5 kV. This amplitude is rather low compared to the ±16 kV which were used in the original design [Osterwalder10] by using custom built amplifiers with 30–10 kHz bandwidth, and this lower amplitude increases the minimum decelerator length needed to bring molecules to a standstill. A 50 cm long decelerator for ammonia [Quintero-Pérez13] and a 4 × 50 cm long decelerator for the heavier SrF [vandenBerg14] molecule were not sufficient to reach a standstill with Trek amplifiers. Thus, due to the technical limitations on the electronics, ring decelerators are mainly used as second stage deceleration units after a traditional switching decelerator [Quintero-Pérez13, Jansen13].

By miniaturizing this traveling-wave ring decelerator, large and deep, truly three-dimensional trapping can be combined with a much easier design of the electronics, allowing thus for full deceleration directly from a molecular beam down to a standstill.

6.2 Working Principle of a Ring Decelerator

The principle of operation of this decelerator has been described before in References [Osterwalder10, Meek11a, vandeMeerakker12], and a brief overview will be given here based on these previous works. Cylindrical coordinates are chosen here because they match the symmetry of the original decelerator design and are conceptually relatively easy to treat analytically, also because of the lower number of independent variables. In the chip version of the decelerator the geometry is rectangular, which changes the behavior especially in the corners of the rectangle. Because of the high aspect ratio of 1:10 the trap electric field will behave like a stretched version of the original one, which reduces the electric field at the far edges slightly. Nevertheless, simulations show that the resulting electric field there is still significantly higher than on the original chip, which still allows to create deeper traps.

The traveling-wave ring decelerator consists of a periodic arrangement of metallic ring electrodes. Each period consists of $N = 8$ electrodes to which voltages are applied, generating the electric field minima for trapping lfs molecules. The rings have an inner radius R_0 and the period length is called λ. The axis Z goes through the center of the rings at $R = 0$. Because of this ring geometry the electric field has cylindrical symmetry.

For the description of the electric field inside the ring structure it is helpful to first consider the potential inside an infinitely long, conducting, and hollow cylinder to which a spatially varying potential is applied along the Z-axis. The cylinder has an inner diameter of R_0 and the symmetry axis coincides with the Z-axis. In the absence of free charges, the electric potential $\Phi(R, Z)$ obeys the Laplace equation

$$\boldsymbol{\nabla}^2 \Phi(R, Z) = 0. \tag{6.1}$$

Using the ansatz of separation of variables, $\Phi(R, Z) = \Phi_R(R)\Phi_Z(Z)$, the Laplace equation can be separated in two independent parts, yielding two ordinary differential equations

$$\frac{\mathrm{d}^2\Phi_Z(Z)}{\mathrm{d}Z^2} + k^2\Phi_Z(Z) = 0 \tag{6.2}$$

and

$$R^2\frac{\mathrm{d}^2\Phi_R(R)}{\mathrm{d}R^2} + R\frac{\mathrm{d}\Phi_R(R)}{\mathrm{d}R} - k^2R^2\Phi_R(R) = 0, \tag{6.3}$$

where k is assumed to be a nonzero, real constant which describes the periodicity of the potential $\lambda = 2\pi/k$ and $\Phi_Z(Z)$ varies sinusoidally with this constant k. The solution for the radial part is proportional to a modified Bessel function of the first kind of zero order, so $\Phi_R(R) \propto I_0(kR)$, which can be approximated by $1 + (kR)^2/4$ in the range $0 \leq kR \leq 1$. Due to the linearity of the Laplace equation, the sum of its solutions is a solution as well. The general solution of the potential, which is cylindrically symmetric, finite along Z and periodic with periodicity $\lambda = 2\pi/k$, is given as

$$\Phi(R, Z) = \sum_{n=0}^{\infty} A_n \cos(nkZ + \delta_n) I_0(nkR). \tag{6.4}$$

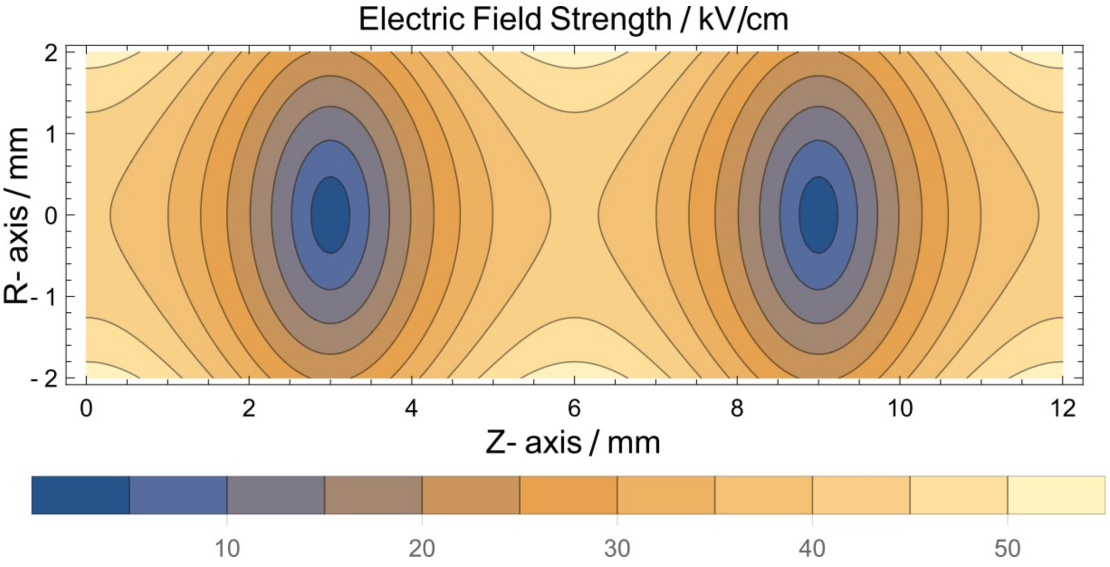

Figure 6.1: Electric field strength contours for an infinitely long, hollow, and conducting cylinder with sinusoidally varying potential at $|R_0| = 2$ mm, a periodicity $\lambda = 12$ mm and potential amplitude $U_0 = 10$ kV, given by Equation 6.6. Two electric field minima are generated which act as traps for dipolar molecules in lfs quantum states.

Under the assumption that the potential at the inner surface ($R = R_0$) is given by $\Phi(R_0, Z) = U_0 \cos(kZ)$, only the $n = 1$ term survives and

$$\Phi(R, Z) = \left[\frac{U_0}{I_0(kR_0)}\right] I_0(kR)\cos(kZ). \tag{6.5}$$

This directly yields the electric field $\vec{E}(R, Z) = -\boldsymbol{\nabla}\Phi(R, Z)$ inside the cylinder, with magnitude

$$E(R, Z) = \frac{U_0 k}{I_0(kR_0)}\sqrt{[I_1(kR)\cos(kZ)]^2 + [I_0(kR)\sin(kZ)]^2}, \tag{6.6}$$

where I_1 is the spatial derivative of I_0. A graphical version of this electric field is shown in Figure 6.1. Two electric field minima are generated per period, acting as traps for dipolar molecules in lfs quantum states.

In the decelerator setup, the continuous potential $\Phi(R, Z)$ is sampled by the $N = 8$ rings per period and the electric field will not be exactly the same as described here. Nevertheless, the basic features of the real trap field are reproduced very well with the continuous model. The voltage on each of the rings is then given by

$$U_n(t) = U_0 \sin(\phi_0(t) + 2\pi n/N), \tag{6.7}$$

where $n = 1, 2, \ldots, N$ numbers the electrodes and $\phi_0(t)$ describes the time evolution of the phase. To determine the exact trapping electric field and potential, numerical simulations must be performed, which is done in Subsection 6.3.2.

Trapping, Guiding and Deceleration

A constant phase ϕ_0 describes a static situation where the position of the traps is fixed in space and time. When the potential is varied sinusoidally in time, the phase can be described by $\phi_0(t) = 2\pi f t$ and the traps start to move smoothly along the long axis Z of the decelerator, which can be used for guiding trapped molecules with a particular velocity. The velocity of the traps is given by $v(t) = f(t) \cdot \lambda$. Thus, with a period of $\lambda = 0.6$ mm a frequency $f = 500$ kHz is needed to move the traps at a speed of 300 m/s. Ramping down the frequency $f(t)$ over time leads to smooth deceleration to arbitrarily low velocities. How fast the deceleration can be performed is limited by the trap depth, as will be described later.

An additional way of guiding molecules can be done, which is conceptually even simpler than the method described before. If the molecules entering the decelerator can be confined in the transverse direction within the area surrounded by the ring electrodes, they can be guided from the beginning to the end of the decelerator. To achieve this transverse confinement, a high electric field must be created between the electrodes, which can be done by applying a DC potential in an alternating way to the electrodes ($+U$, $-U$, $+U$, $\ldots$) and has been shown to work nicely in practice [Meek11a].

6.3 A Ring Decelerator on a Chip

6.3.1 Design

The geometry of the ring chip has been chosen to be basically a scaled-down version of the original decelerator from References [Osterwalder10, Meek11a] (1:20). The down scaling parameter is determined from the electronics: to achieve high voltage waveforms with good quality the amplitude is restricted to approximately 600 V with the current amplifiers, which would correspond to 12 kV in the original setup. To create trap electric fields with a similar strength, the geometry has to be scaled down with the same ratio.

Because the basic geometry is similar to the original decelerator one can take advantage of the parameter optimization by Osterwalder, Meek and others. During the optimization of geometrical parameters for the original ring decelerator it was found that with an inner ring electrode diameter of 4 mm, a period length of 12 mm, an electrode diameter of 0.6 mm and a periodicity of $N = 8$ the best trap field can be generated. While a higher parameter N means to sample the sine wave better and to create smoother electric fields, it involves higher technical complexity. Also, the performance of a decelerator with higher N was not necessarily better, as simulations showed. $N = 12$ and $N = 6$ performed worse than $N = 8$, while $N = 10$ is comparably good. The reason is that for a constant electrode thickness, with more electrodes per period the gaps between the electrodes shrink, which distorts the field close to the electrodes. With less than 8 electrodes per period this effect is reduced, but the electric field around the center axis decreases. Altogether, an optimum of electrode thickness and electrode gap was found with $N = 8$. [Meek11a]

Manufacturing a chip-based circular loop is difficult, therefore squared (rectangular) loops will be constructed. A trench is etched into a Si substrate (covered by an insulating layer of Benzocyclobutene (BCB), a polymer) and a regular pattern of metallic stripes is deposited along the trench. The three metallic sides of the stripes in the trench form three of the four sides of the loop, the fourth is a metallic wire added by a wire bonder, which closes the loop. By placing many of these squared loops next to each other, the total acceptance area of a trap is increased and more molecules can be trapped. By virtually removing the touching sides of the squared loops a large rectangular loop is formed with similar electric fields, but which is easier to manufacture. Each rectangular loop is approximately 200 µm high, 2000 µm wide, is approximately 20–30 µm thick, and has a center-to-center spacing of 75 µm to its next-nearest neighbors along the trench axis Z. The voltages repeat after $N = 8$ electrodes ($\lambda = 600$ µm).

In Figure 6.2 the final geometry of the design is shown. The metallic loops (Al) are shown in the center of the structure. They are connected to every electrode which is an integer multiple of 8 electrodes away via the distribution pads, which are connected with Al wires that extend over the surface of the chip. One of them has a connection to a larger pad (green line), farther away from the central structure, where the externally generated voltages are brought to the chip. A unit cell of the repeating structure with the 8 loops has been indicated with the dotted rectangle. The bonding process will have an accuracy in the height of a bond of approximately 20–30 µm, the positioning on the landing pads is within 5–10 µm. A cross section of the chip with one loop can be seen in figure (b). The trench with the metalization and the wire on top (forming the loop) is clearly visible. The substrate and surface manipulations are carried out either at the *Fraunhofer Institute for Reliability and Microintegration "IZM"*, Berlin or the *Halbleiterlabor of the Max-Planck-Society*, Munich.

6.3.2 Simulations

Traps for CO Molecules

The amplitude of the voltages for the ring chip is on the order of ±600 V, corresponding to a voltage of ±12 kV in the original design. The generated electric field corresponds to periodic Stark energy minima for polar molecules in lfs quantum states. Two-dimensional and one-dimensional cuts of this Stark energy are shown for ^{12}CO molecules in Figure 6.3 for the situation that the long trap axis is between two electrodes. The traps have a tubular shape with an aspect ratio of 10:1 (X:Y).

The trap depth is limited by the saddle points of Stark energy around each minimum which allow molecules with sufficient energy to escape. Electric field saddle points along trap axes of approximately 20–29 kV/cm (in X), 26–31 kV/cm (along Y), and 37 kV/cm (along Z) are generated. The range of values is a result of the fact that the saddle points change their height depending on the position of the trap along the beam axis Z. The lowest saddle point is generated in the 4 corners of the trap when the trap axis is between two electrodes (16 kV/cm, 250 mK).

In Figure 6.3(a) the two-dimensional $Y = 0$ mm plane (center position along this axis) is shown for one complete period, containing the two traps per period. At $X = \pm 1$ mm 8 electrodes are indicated by black squares. For large parts along X the trap energy does not change significantly, only close to the electrodes the Stark energy increases strongly, which closes the trap in this direction. The color-coded energy legend is clipping at 1000 mK to improve the visibility of the low energy details of the trap. Figure (b) shows the cut for the $Z = 0.1125$ mm plane, across the minimum of a trap shown in figure (a) where the lowest saddle point of approximately 16 kV/cm or 250 mK occurs in the four corners.

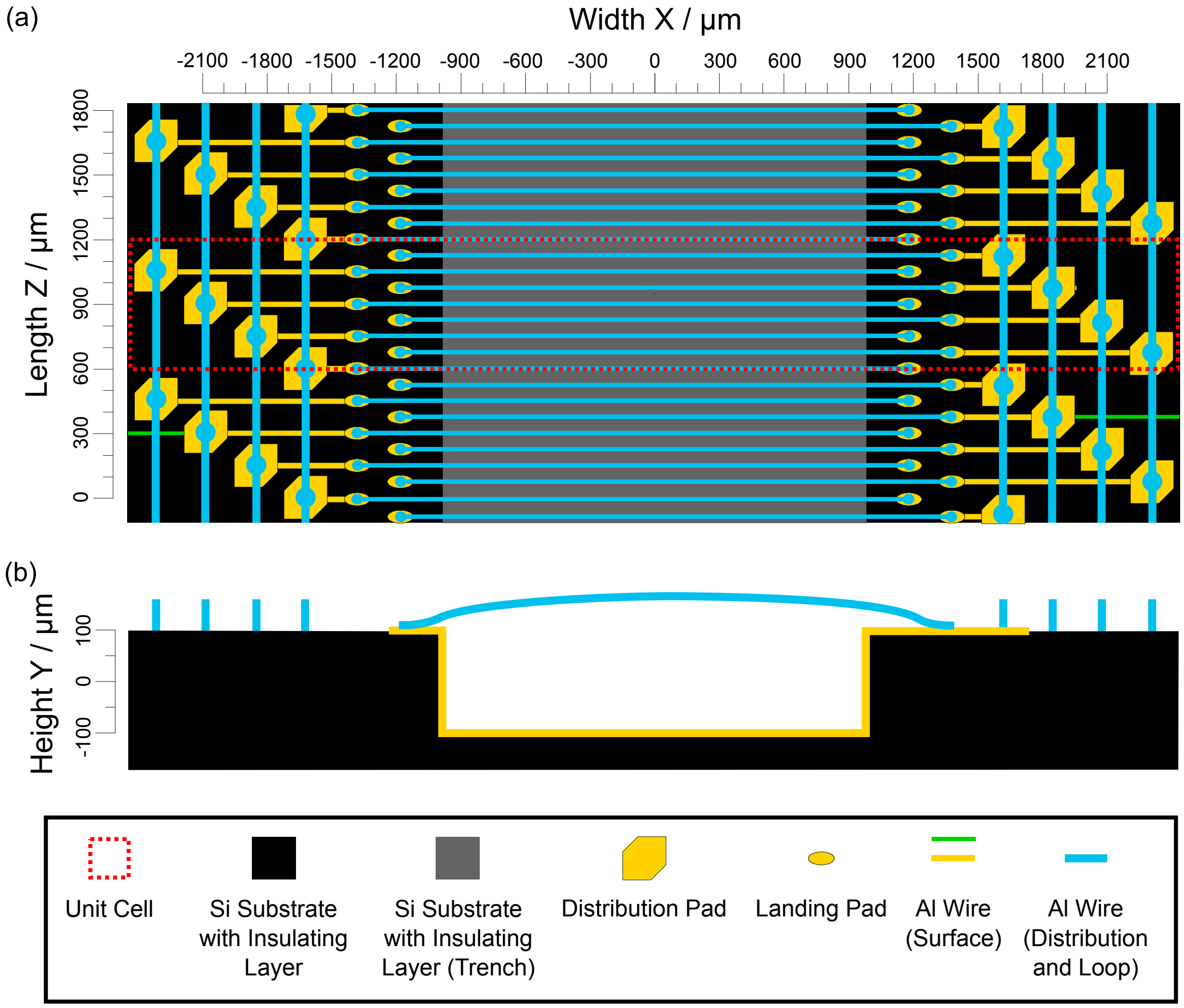

Figure 6.2: Geometry of the ring chip. (a) Top view on the center part of the chip. A Si substrate with an insulating layer has Al structures on its surface (Al wire, landing pad, distribution pad). A wire bonder connects the landing pads to form a closed loop electrode and it also connects the distribution pads among each other (wires extend above the surface). Also, because of the periodicity, every eighth electrode is connected to the same voltage (wires extend above the surface). The two green Al wires connect the distribution pads to the one pad which is connected to a waveform generator. (b) Cross sectional view on the center part of the chip. The aspect ratio is not to scale.

In figure (c) the $X = 0$ mm plane (center position along this axis) is shown for a complete period. The colored line profiles shown in figures (d)–(f) directly correspond to the colored lines and dots in figures (a)–(c). Figure (d) shows three cuts along the X-axis: one along the minimum, one along the saddle point and one directly in between. The potential along the X-direction is almost flat except for the region close to the electrodes. The cut along the minimum reaches a local maximum (saddle point) of approximately 325 mK on the trap axis within the area surrounded by the electrodes ($|X| \leq 1$ mm). The other two lines show an upshifted energy in the center and a slightly different behavior at the edges because no minimum is generated between the other electrodes along the X-direction. The cuts along the Z-direction are shown in figure (e). They have a rather linear slope close to the minima. The saddle point between the minima lies at an energy of approximately 600 mK for most parts along X. The cuts along the Y-direction are shown in figure (f). Again, the flanks of the potential are relatively linear across the trap minimum and show a saddle point of approximately 425 mK.

The trap shape is not completely constant when the trap moves along the Z-direction. The two extreme cases, the minimum being between two electrodes or above an electrode, are shown in Figure 6.4. The case with the minimum between two electrodes is already shown in Figure 6.3. Two-dimensional cuts of the Stark energy for these two cases can be seen in figures (a) and (b), centered along the long trap axis X. The effect that the trap height varies with the Z-position of the minimum has also already been described before in Reference [Meek11a]. In figures (c)–(e) one-dimensional cuts through the trap energy are shown. These lines always represent positions through the trap minimum in Z (for (c) and (d)) and centered along the long axis X (for (e)). In figures (c) and (d) it can be seen that for the X- and Y-direction within a distance of approximately 50 µm from the electrodes a significant change of the Stark energy is occurring. There, the energy changes by up to factor of 2 between the two cases. Along Z no change is observed. Note that the curve taken for case (b) has been shifted back by half an electrode spacing for better comparison between the two curves (which overlap strongly). The periodic modulation of the potential depending on the trap position with respect to the electrodes is experienced by guided molecules as a “breathing motion” of the trap with 4.4 MHz frequency at 330 m/s guiding speed. This periodic modulation of the trapping potential extends over approximately half the size of the trap (2×50 µm compared to 200 µm size along Y) with variable strength.

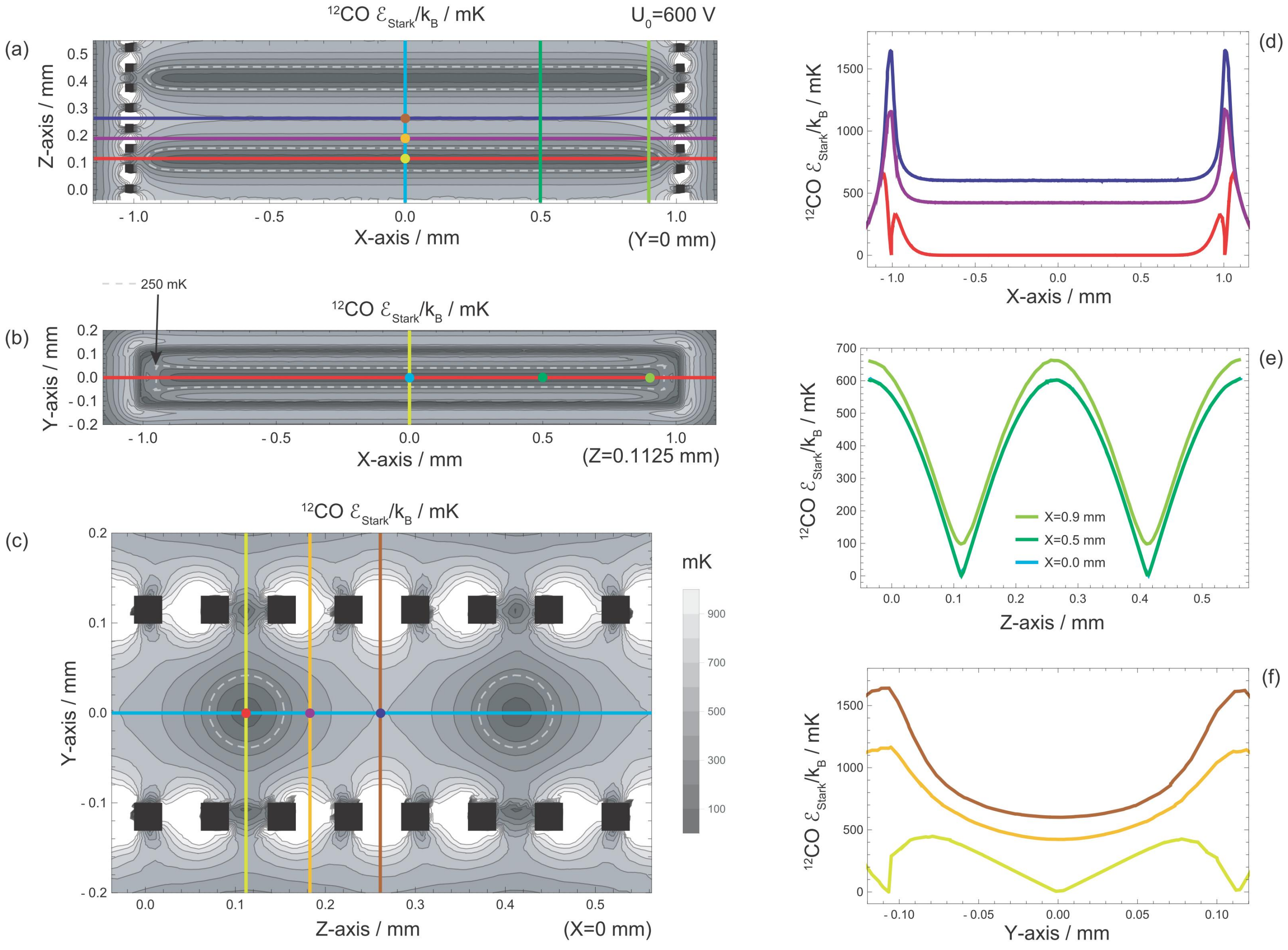

Figure 6.3: Traps for ^{12}CO generated with the ring chip decelerator. Figures (a)–(c) show the Stark energy on three perpendicular planes. The two minima per period can be observed. Figures (d)–(f) contain the Stark energy along several lines, which are also indicated in the other figures. The 250 mK dashed line indicates the volume where molecules can be stably trapped. In (a)–(c) the energy is clipped at 1000 mK.

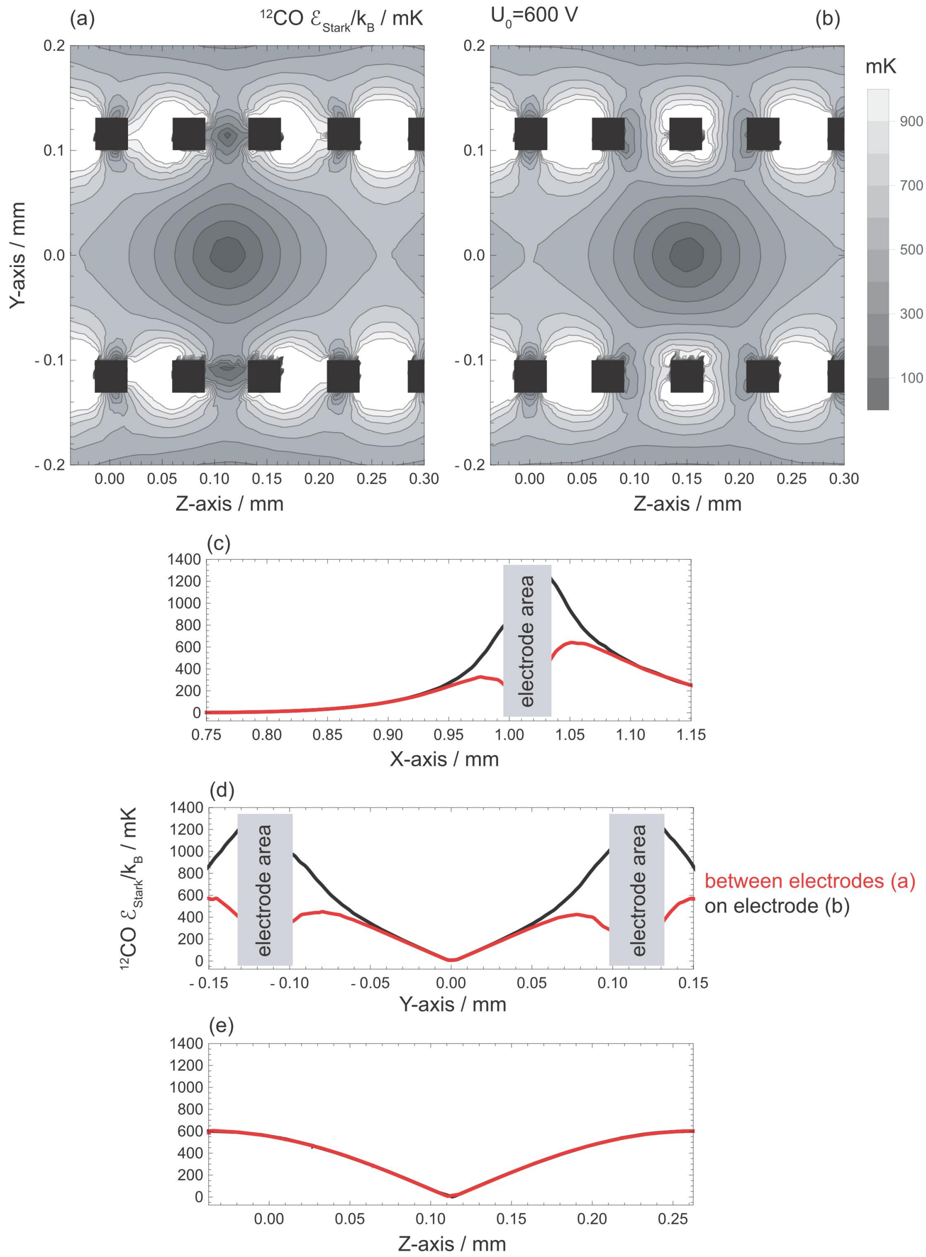

Figure 6.4: The figures shows how the trap energy for ^{12}CO changes for the two cases: trap axis between electrodes and on top of an electrode. (a) and (b) show the Stark energy for the two cases on the $X = 0$ mm (center) plane. In (c) a cut along X is shown going through the minimum, in (d) the same is shown for Y. In figure (e) the trap energy along the molecular beam axis Z is shown for each case; the line for the "on electrode" case is shifted back by half an electrode spacing for better comparison between the two curves, which overlap strongly. In (a) and (b) the energy is clipped at 1000 mK.

Effective Traps under Deceleration

As has been explained for the two-dimensional chip before, the effective trap volume is reduced during acceleration (deceleration). Again, this can be understood by modeling the acceleration as an additional (pseudo-)potential $U_{\mathrm{Pseudo}} = -m \cdot a \cdot Z$. The effect of adding this potential to the original trapping potential is shown in Figure 6.5, where the $Z = 0$ mm point has been chosen to be at the minimum. Four different accelerations a between 0.0 and -1.5 µm/µs^2 are shown in figures (a)–(d). By increasing the deceleration the effective potential is tilted. At -1.5 µm/µs^2 the trap for ^{12}CO and $U_0 = 600$ V is only ≈ 50 mK along Z, at 1.85 µm/µs^2 it opens up completely (not shown) and no molecules can be trapped anymore. In figure (e) this tilt in the effective potential due to the acceleration can be seen on the line going through the minimum ($X = Y = 0$ mm). To decelerate CO molecules from 330 m/s to a standstill using $a = -1.0$ µm/µs^2, a decelerator length of 54 mm is required. Chip lengths up to 300 mm are planned, in order to decelerate even much heavier molecules.

6.3.3 Comparison of Trappable Phase Space

To compare the estimated amount of trappable molecules on the new ring chip with the original chip, first the volume of one trap is calculated in which ^{12}CO molecules with a particular kinetic energy $\mathcal{E}_{\mathrm{Kin}}$ can be trapped. This is similar to the procedure from Section 4.3.1 and the result is shown in Figure 6.6(a) for both chips. At zero kinetic energy the whole trap volume is able to stably trap molecules, whereas at the trap maximum of 87 mK for the original chip and approximately 250 mK for the lowest energy saddle point of the ring chip this ability goes to zero. The peak-to-peak voltages used to create the trap electric field are 1200 V for the ring chip and 240 V for the original chip, which are on the upper end of possible voltages for each case. The curve for the original chip has been increased by a factor of 7 for better comparison.

The number of molecules in each trap, $N_{\mathrm{tot}}(\mathcal{E})$, is calculated as

$$N_{\mathrm{tot}}(\mathcal{E}) = \int_{\mathcal{E}_{\mathrm{Kin}}=0}^{\mathcal{E}_{\mathrm{Kin}}=\mathcal{E}} V(\mathcal{E}_{\mathrm{Kin}})\rho(\mathcal{E}_{\mathrm{Kin}})d\mathcal{E}_{\mathrm{Kin}}. \tag{6.8}$$

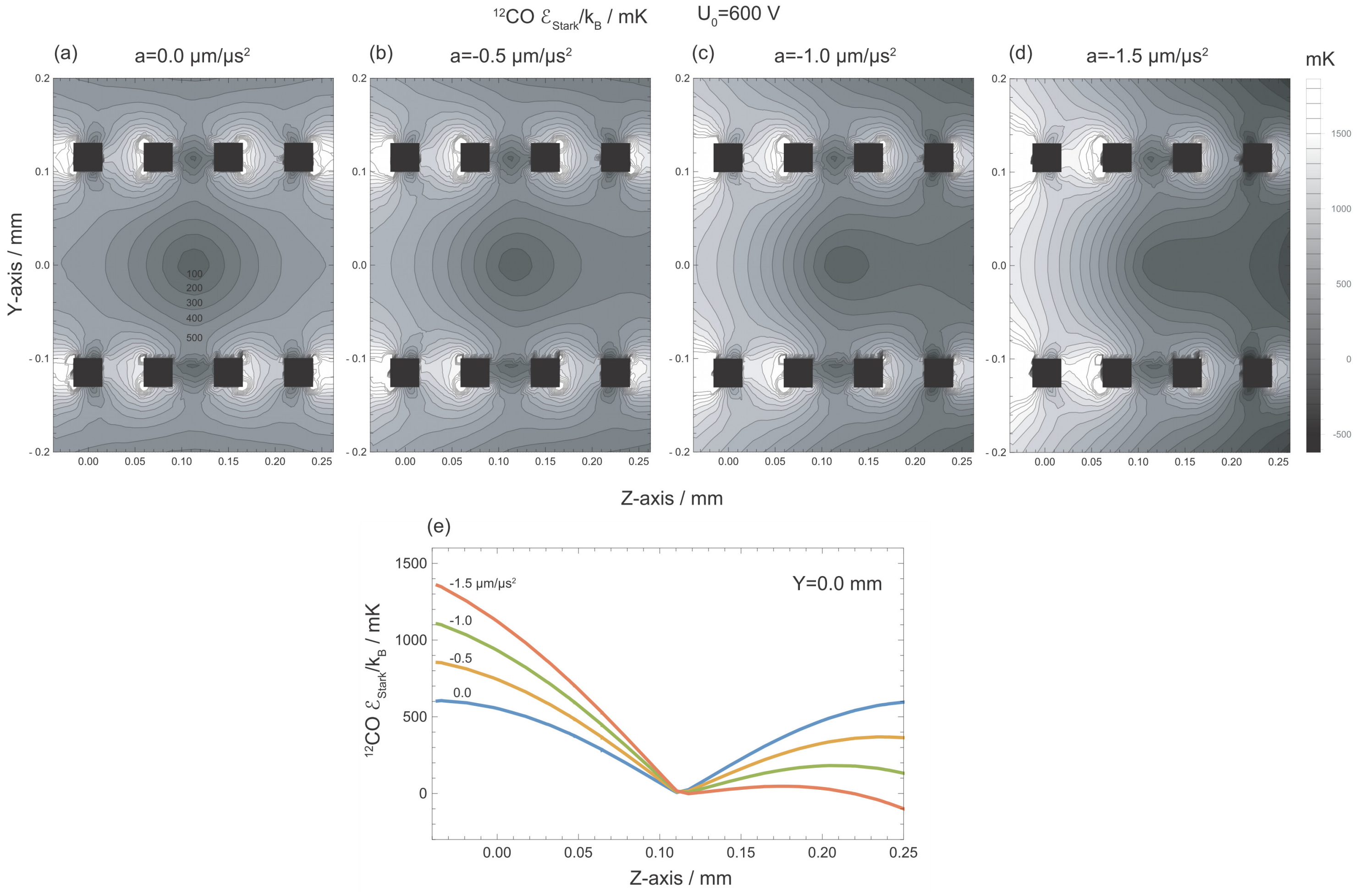

Figure 6.5: Effective trapping potential for ^{12}CO molecules under a deceleration a between 0 and -1.5 µm/µs^2. A higher deceleration decreases the trap depth until the trap is almost nonexistent anymore (≈ 50 mK at -1.5 µm/µs^2 along Z, 0 mK along Z at -1.85 µm/µs^2 at 600 V amplitude). Figure (e) shows a cut along the center line for each of the four cases. In (a)–(d) the energy is clipped at 1000 mK.

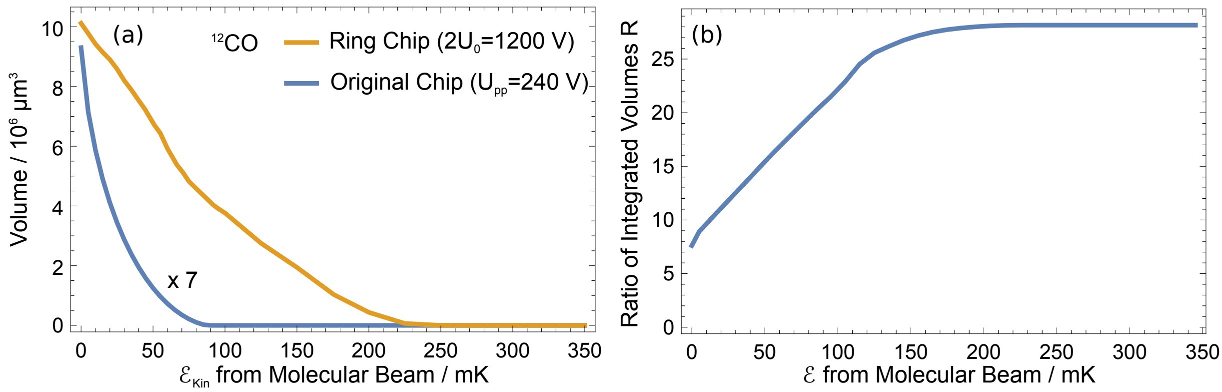

Figure 6.6: Comparison between a ring chip trap and one from the original trap. (a) The volume for each chip trap which allows to trap ^{12}CO molecules of a given kinetic energy $\mathcal{E}_{\mathrm{Kin}}$ in the molecular beam. (b) Ratio $R(\mathcal{E})$ of integrated trap volumes, reflecting the ratio of total particles trappable in the kinetic energy range between 0 and $\mathcal{E}$.

The ratio R of trapped molecules up to a kinetic energy $\mathcal{E}$ is given by

$$R(\mathcal{E}) = \frac{N_{\mathrm{tot,ring}}(\mathcal{E})}{N_{\mathrm{tot,orig}}(\mathcal{E})} = \int_{\mathcal{E}_{\mathrm{Kin}}=0}^{\mathcal{E}_{\mathrm{Kin}}=\mathcal{E}} \frac{V_{\mathrm{ring}}(\mathcal{E}_{\mathrm{Kin}})}{V_{\mathrm{orig}}(\mathcal{E}_{\mathrm{Kin}})} d\mathcal{E}_{\mathrm{Kin}}, \tag{6.9}$$

because the density in the molecular beam $\rho(\mathcal{E}_{\mathrm{Kin}})$ is assumed to be constant for the given energy range and the same for each case. This is shown in figure (b). The curve starts from a ratio of approximately 7 at zero kinetic energy and progressively increases to approximately $R = 28$ at 250 mK, which reflects the much larger volume of the ring chip trap at all energies. For energies larger than the maximum trap depth of the ring chip trap the ratio is constant because no more molecules can be (stably) trapped. For short times much more molecules could be trapped though (up to approximately $R = 420$ for the 600 mK highest energy saddle point along Z). Therefore, it is concluded that the new chip design will allow to trap much more molecules.

6.3.4 Capacitance

A technically important parameter for the design and operation of the ring chip is its capacitance. A high capacitance implies that large currents are needed to sustain the applied voltages and obtaining waveforms with low distortion is harder for larger currents. By minimizing the capacitance, the electronics can be simplified and/or the waveform quality can be improved. Furthermore, smaller currents induce less heating.

Using the COMSOL Multiphysics software suite the capacitance can be modeled by implementing the geometry and the material properties. To simplify the geometry it is assumed that the central structure of the chip (the loops) dominates the capacitance. This is justified because there the metallic structures are much closer together than in the outside region. One unit cell of 8 electrodes is simulated and periodic boundary conditions are applied to take into account the effect of neighboring unit cells. The total capacitance of a chip is then calculated by multiplying the capacitance per unit cell with the number of unit cells on the chip.

Since the system is more complex than a simple parallel plate capacitor, the mutual effects from each combination of two electrodes need to be taken into account. This can be done by setting up a capacitance matrix C with elements $C_{i,j}$, where indices i and j number the respective electrode 1–8 in the unit cell. The elements of the capacitance matrix define the charge on each electrode $Q_i = \sum_{j=1}^{8} C_{i,j} U_j$ for given voltages U_j on the electrodes. The charges Q_i are the elements of the charge vector $\vec{Q}$, whereas the elements U_i are the elements of the voltage vector $\vec{U}$. The elements $C_{i,i}$ describe the self-capacitance of the electrode i with itself, elements $C_{i,j}$ $(i \neq j)$ describe the mutual capacitance between electrodes i and j. Without loss of generality the capacitance matrix can be described with the form

$$C = \begin{pmatrix} c_1 & c_2 & c_3 & c_4 & c_5 & c_4 & c_3 & c_2 \\ c_2 & c_1 & c_2 & c_3 & c_4 & c_5 & c_4 & c_3 \\ c_3 & c_2 & c_1 & c_2 & c_3 & c_4 & c_5 & c_4 \\ c_4 & c_3 & c_2 & c_1 & c_2 & c_3 & c_4 & c_5 \\ c_5 & c_4 & c_3 & c_2 & c_1 & c_2 & c_3 & c_4 \\ c_4 & c_5 & c_4 & c_3 & c_2 & c_1 & c_2 & c_3 \\ c_3 & c_4 & c_5 & c_4 & c_3 & c_2 & c_1 & c_2 \\ c_2 & c_3 & c_4 & c_5 & c_4 & c_3 & c_2 & c_1 \end{pmatrix}, \tag{6.10}$$

because of the mirror symmetry around the electrode $i = j$ (i.e. the diagonal; the capacitance must be the same between electrodes that are in the same mutual position) together with the translational symmetry $(C_{i,j} = C_{i+1,j+1})$ of the loop structure. As has been stated before, the charge on the ith electrode Q_i at every instant of time is given by the voltages U_j on the electrodes j as $Q_i = \sum_{j=1}^{8} C_{i,j} U_j$. Since the voltage waveforms on the electrodes

$$\begin{aligned} c_1 &= 1.65\ 10^{-13} \quad \mathrm{F} \\ c_2 &= -4.94\ 10^{-14} \quad \mathrm{F} \\ c_3 &= -1.74\ 10^{-14} \quad \mathrm{F} \\ c_4 &= -1.16\ 10^{-14} \quad \mathrm{F} \\ c_5 &= -1.03\ 10^{-14} \quad \mathrm{F}, \end{aligned}$$

Table 6.1: Elements of the capacitance matrix of the ring chip.

have a phase shifted sinusoidal form, the charge on the electrode i is given by

$$\begin{aligned} Q_i &= \sum_{j=1}^{8} C_{i,j} U_0 \sin\Big(\omega t + \frac{2\pi}{8}(j-1)\Big) \\ &= ([c_1 - c_5]\sin(\omega t) + [c_3 - c_3]\sin(\omega t + \pi/2) \\ &\quad + [c_4 - c_2]\sin(\omega t + 3\pi/4) + [c_2 - c_4]\sin(\omega t + \pi/4))U_0 \\ &= [c_1 + \sqrt{2}(c_2 - c_4) - c_5]U_0 \sin\Big(\omega t + \frac{2\pi}{8}(i-1)\Big), \end{aligned} \tag{6.11}$$

where Q_i oscillates in phase with voltage U_i. An effective capacitance of

$$C_{\text{eff}} = Q_i/U_i = c_1 + \sqrt{2}(c_2 - c_4) - c_5 \tag{6.12}$$

can be assigned, which is also the eigenvalue of the capacitance matrix with an eigenvector where the neighboring voltages resemble a sine wave with a 45° interval, $\vec{U} = U_0(\sqrt{2}, 1, 0, -1, -\sqrt{2}, -1, 0, 1)$.

To evaluate C_{eff} it remains to determine the elements of the capacitance matrix. To achieve this, the induced charge on each electrode q_j is calculated by integrating the charge density over electrode j in COMSOL Multiphysics when the electrode i was set to 1 V. The elements c_i of the capacitance matrix C are then calculated as $c_i = q_i/1$ V. The elements are shown in Table 6.1 and give rise to the effective capacitance per channel and period of $C_{\text{eff}} = 1.22\ 10^{-13}$ F or 0.122 pF. Assuming a length of the chip of $l = 333\lambda = 20$ cm, one channel has a capacitance of $333C_{\text{eff}} = 40.7$ pF because these unit cells (capacitances) lie in parallel. Under the above-mentioned assumption that the central parts of the chip dominate the capacitance, the final total capacitance of one channel on the chip should roughly be between 1–2 times this value, approximately 40–80 pF, which is close to the measured values of approximately 80 pF for chips up to approximately 20 cm length.

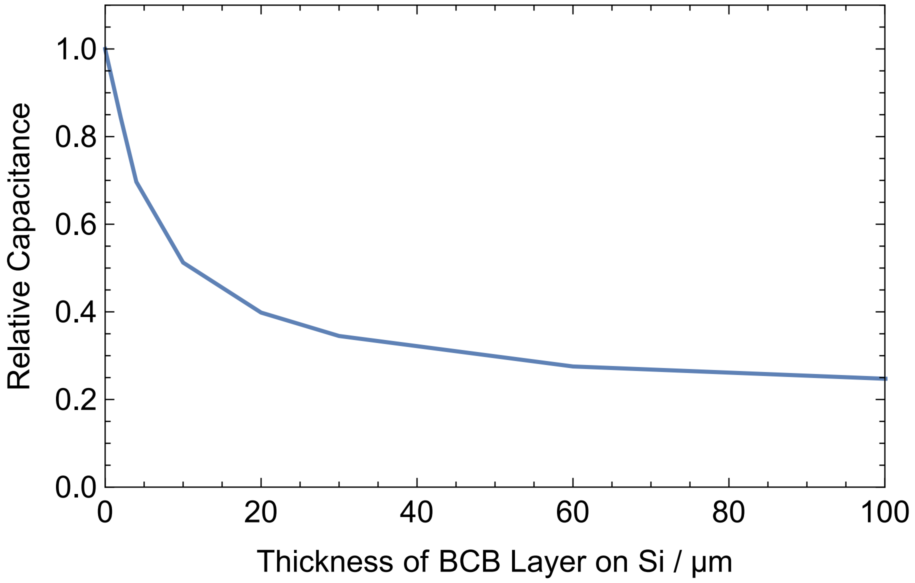

Figure 6.7: Relative dependence of the capacitance of the loop structure on the BCB insulating layer's thickness. The insulating layer separates the surface metallization and the semiconducting Si bulk material.

Minimization Since the capacitance of a (parallel plate) capacitor $C_{\mathrm{pp}} \propto \epsilon_{\mathrm{r}}$, the dielectric constant of the material in the vicinity and between the plates, the capacitance can be minimized by the choice of a material with low dielectric constant. One such material is the BCB polymer which is used as an insulating material on the chip and has a relatively low dielectric constant $\epsilon_{\mathrm{r}} \approx 2.7$ [Burdeaux90]. Especially the comparison to pure Si (the bulk material) is most important, which has a much larger dielectric constant $\epsilon_{\mathrm{r}} \approx 11.7$ [Dunlap53]. To minimize the capacitance, the effect of the BCB insulating layer between the surface metallization and the semiconducting Si substrate is calculated in dependence on the insulating layer's thickness with COMSOL, see Figure 6.7. At zero thickness, only the Si material influences the capacitance. The capacitance drops quickly by increasing the insulating layer's thickness, reaching a value of approximately 25% at infinite layer thickness (capacitance of a pure BCB substrate). A reasonable thickness of 20 μm amounts already to a 40% relative capacitance compared to pure Si, which is chosen in the setup.

6.4 Status and Outlook

So far, several versions of the ring chip have been fabricated but they had various problems. Either they could not withstand a high enough voltage, they had shorts between the electrodes or parts of the loops were electrically isolated. Two of these chips are shown in Figure 6.8, one in top view and the other in cross section. Additionally, the amplifier rack and a measurement of the voltage waveforms is shown. These prototypes have a trench width of 1 mm and 2 mm, respectively, and a loop height of roughly 220 µm. They can be used to test the design, the materials and the amplifiers producing the voltage waveforms. Tests were performed to measure technical parameters and to find the weak point in the current design. Parameters include the resistance between the channels, the capacitance, the temperature increase during operation and how much voltage the structure is able to withstand. Different versions of the chip have different lengths (a few up to 20 cm) and material composition (Au or Al on Si).

The capacitance of the chips of approximately 80 pF is already in a range which the amplifiers can handle and the overall temperature increase is low, so no more effort will be taken to reduce it further. The resistance between the channels is at least on the order of 1 GΩ, which is satisfactory.

A problem that was encountered was the local heating in spots with higher resistance on the surface metallization. This lead to the melting of material from the surface. To reduce this effect, the latest version has a thicker metallization layer (3 µm) and wider connectors, which will reduce the resistance by a considerable factor.

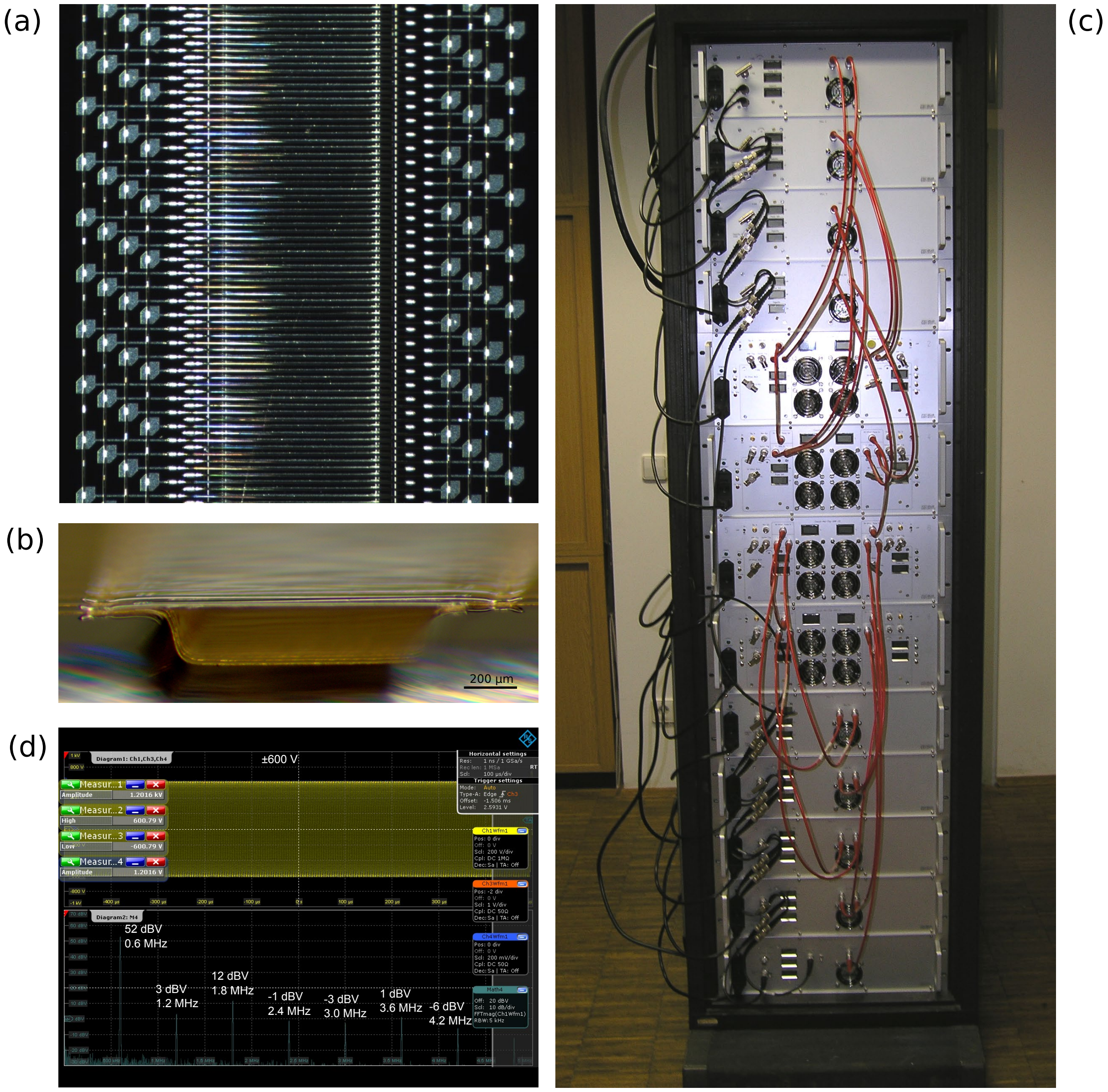

Figure 6.8: Overview about the existing setup: a test chip and the amplifier rack. (a) Bonded chip with 2-mm trench width. (b) A zoomed cross section of a 1-mm trench width chip, showing the entrance of the chip. (c) The rack with the 8 amplifiers producing the waveforms for the chip electrodes. (d) Measured waveforms with 600 V amplitude at 600 kHz frequency (360 m/s) shown together with the frequency spectrum of this waveform, indicating the waveform quality of approximately −40 dB harmonic distortion.

CHAPTER 7

Outlook

The coldest molecular species to date are alkali dimers created by associating ultracold atoms. [Quéméner12] They have been employed, for instance, in the studies of ultracold bimolecular reactions [deMiranda11, Ospelkaus10] and have been trapped in optical lattices to analyze their quantum dynamics, which represents the first step towards using these systems to explore many-body dynamics in regimes that are inaccessible to current theoretical techniques [Hazzard14]. Understandably, these quite exotic species have not been at the focus of the spectroscopists' and chemists' attention. Instead, ordinary molecules cooled by direct methods have reached temperatures around 1 mK, or slightly below [Prehn16, Norrgard16], an improvement of about three orders of magnitude on a free supersonic beam.

This level of control of the molecular motion has proved itself precious for high-resolution atom-molecule collision experiments [Gilijamse06, Shagam15] and for measurements of the lifetime of metastable molecular states [vandeMeerakker05, Gilijamse07]. In the field of high-resolution spectroscopy, though, cold, decelerated molecules have found remarkably little application [vanVeldhoven04, Bethlem08].

In the frequency range starting from about the mid-IR, Doppler broadening is the main source of frequency uncertainty in high-resolution spectroscopic measurements. Molecular beams have reduced this to the level of the transversal temperature of the supersonic beam, with uncertainties on the order of a MHz or below. Alternatively, two-photon or saturation spectroscopy also overcomes this limit. In a gas cell the uncertainty limits are collisional broadening and the interaction time, whereas only the latter is relevant for experiments in the beam. Experiments on free supersonic beams have reached interaction (coherence) time on the order of 1 ms for SF_6 [Shelkovnikov08], YbF [Hudson11], and ThO [Baron14] molecules.

Ideally, a high-resolution spectroscopic experiment is performed away from any object that could induce stray fields and thus perturb the measurement. Thus, a convenient experimental setup involves launching decelerated molecules in a fountain configuration or in a beam. Once the molecular ensemble has been launched, it immediately starts to expand at a speed related to its temperature. Thus, it is clear that the molecular cloud must be launched at a speed which is several times the average thermal velocity in order to allow most of the molecules to participate to the measurement. A mK temperature corresponds to a few m/s for a small molecule of the kind that is typically decelerated, which implies a launching speed of tens of m/s. The three orders of magnitude in temperature reduction from the free supersonic beam to a Stark decelerated packet of molecules corresponds to a reduction of a factor 30 in velocity. Nevertheless, to date, the better signal-to-noise ratios obtained with free, non-decelerated, beams have generally been more successful than the decelerated molecules for high-resolution spectroscopy [Shelkovnikov08, Hudson11, Baron14]. One of the few examples of spectroscopy on a decelerated species is $^{15}ND_3$. The low velocity of the decelerated molecule allowed for the resolution of two hyperfine transitions within the $|J = 1, K = 1\rangle$ state lying close in energy, which are separated by approximately 3 kHz. [vanVeldhoven04]

For a significant improvement in spectroscopy, a further cooling stage is thus required. After the first direct cooling of the molecules to the mK range, their temperature could be reduced further by a sympathetic cooling step, where they interact with atoms that are previously laser-cooled down to the µK range. Sympathetic cooling has been successfully applied to atomic ions [Drullinger80], atoms [Myatt97] and molecular ions [Mølhave00] but not yet to neutral molecules.

Once an ultracold molecular sample is produced, more experiments become possible than pure spectroscopic measurements. Rotational states of molecules having a permanent electric dipole moment, like the ones used in this thesis, can be coherently manipulated with DC or low frequency electric fields. These electric fields can be created and controlled already to high precision with current microwave technology, which has already been implemented on microchips. [Clarke08, Böhi09, Hammer15] Therefore, the coherent manipulation of ultracold dipolar molecules on microelectronic devices seems to be a rather straightforward method. In addition, the long-ranged nature of the dipole-dipole interaction between molecules in defined rotational states is a very useful property for generating superposition and entangled states between molecules, because these kinds of states lie at the heart of quantum computation. [André06]

Danksagung

Schlussendlich möchte ich die Gelegenheit ergreifen um den vielen Leuten, ohne die diese Arbeit so nicht möglich gewesen wäre, für ihre Unterstützung während meiner Promotion zu danken.

Zuerst möchte ich meinem Betreuer Gerard Meijer dafür danken, dass ich die letzten Jahre an diesem spannenden Projekt arbeiten durfte, sowie für seine Motivation und Unterstützung während der Arbeit und für seine unkomplizierte Art.

Besonders Gabriele Santambrogio habe ich ebenso sehr viel zu verdanken. Er hat mir vieles beigebracht, speziell was das Verständnis der Physik und den Laboralltag angeht, aber auch wie man Wissenschaft betreibt und wie man sein Projekt möglichst schnell zum Erfolg bringt. Auch für die Zeit in Italien und für die persönliche Ratschläge, für die Hilfe beim wissenschaftlichen Schreiben und das Lesen der Dissertation, sowie dafür, dass er mich zu hoher Leistung angespornt hat, möchte ich mich sehr herzlich bedanken!

Die praktische Laborerfahrung und speziell die Optik- und Englischkenntnisse von David Adu Smith haben mir besonders geholfen. Großer Dank gebührt auch Mark Abel, mit dem ich anfänglich im Labor zusammengearbeitet habe und der mir so lange erklären musste, wie die Dinge im Labor genau funktionieren, bis ich sie wirklich verstanden hatte. Sam Meek hatte vor meiner Ankunft bereits sehr erfolgreich den Chip mitentwickelt und mit ihm gearbeitet. Er wusste glücklicherweise auch immer bei schwierigen Fragen Bescheid. Mit Giacomo Insero habe ich einige Zeit im Labor zusammenarbeiten können, was immer Spaß gemacht hat. Ich bin sicher, dass er erfolgreich mit dem Chip weiterarbeiten wird. Daher möchte ich auch ihnen meinen Dank aussprechen.

Die technische Unterstützung durch Georg Hammer und Andreas Liedke war immer sehr hilfreich. Georgs praktische Kenntnisse beim Umgang und der Reparatur der Düse

waren immer äußerst gefragt. Wolfgang Erlebach und Henrik Haak danke ich für die Unterstützung bei der Konstruktion und dem technischen Zeichnen und Sandy Gewinner für die Hilfestellungen beim Betrieb der Laser. Auch auf Uwe Hoppes Hilfe für KouDa & Co. konnte man immer zählen.

Ohne die Tatkraft von Inga von Dölln und Andrea Braaker wäre wohl viel Organisatorisches in der Abteilung sehr langsam vonstatten gegangen, oder wäre erst gar nicht zustande gekommen, was auch sehr zu der besonders guten Stimmung innerhalb der Abteilung beigetragen hat.

Bretislav Friedrich danke ich für die Organisation der vielen interessanten Vorträge, die immer wieder zeigten, was noch für interessante Forschung in anderen Instituten und Universitäten stattfindet. Boris Sartakov und Phil Bunker danke ich dafür, dass sie mir erklärt haben, wie Moleküle funktionieren.

Auch die Mitarbeiter der Verwaltung und der Zentrale haben mir viel Arbeit abgenommen, was ich sehr zu schätzen weiß. Carmen Pilat danke ich für die Motivation, auch einmal als „Künstler“ anstatt als Wissenschaftler aufzutreten, indem wir zusammen mit Georg Heyne eine Fotoausstellung mit meinen Bildern organisiert haben.

Das Wissen und das Geschick der Mitarbeiter des Elektroniklabors, speziell von Georg Heyne, Viktor Platschkowski und Thomas Zehentbauer haben meine Projekte entscheidend vorangebracht oder zum Teil überhaupt erst ermöglicht. Thomas’ Engagement war immer herausragend, ganz besonders in den schwierigen Momenten, nachdem Teile der Verstärker kaputt gingen und repariert werden mussten, als ich einen Ausfall am wenigsten gebrauchen konnte. Die handwerkliche Unterstützung durch Petrik Bischoff und die Werkstattmitarbeiter war ebenfalls essenziell für das Gelingen der Arbeit.

Auch den vielen Praktikanten, Masteranden, Doktoranden, Postdocs und Gruppenleitern aus der Abteilung Molekülphysik, die man zum Teil auch zu ungewöhnlicher Zeit am Institut antraf, möchte ich für die gute Atmosphäre und ihre Unterstützung in den unterschiedlichsten Situationen danken. Die Weinverkostungen von Alex Woodham und Christian Kerpal waren immer etwas besonderes. Doch auch Veranstaltungen wie die Weihnachtsfeiern, Wandertage, Sommerfeste, die vielen „Kaffee und Kuchen“, die Diavolezza „Science and Ski“-Konferenz, den Aufenthalt in Amsterdam mit Andreas, Carmen und Andrea und vieles mehr werde ich nicht vergessen.

Schließlich in besonderer Weise gebührt mein großer Dank meiner Familie, meinen Eltern Uta und Uwe und meiner Freundin Dorette für die bedingungslose Unterstützung und die Nachsicht, die sie für mich während meines Studiums und der Promotion aufgebracht haben!

List of Publications

1 Abel, M. J., **Marx, S.**, Meijer, G., and Santambrogio, G.
Vibrationally exciting molecules trapped on a microchip.
Molecular Physics, 110(15–16):1829, 2012.
doi:10.1080/00268976.2012.683885

2 **Marx, S.**, Adu Smith, D., Abel, M. J., Zehentbauer, T., Meijer, G., and Santambrogio, G.
Imaging cold molecules on a chip.
Physical Review Letters, 111:243007, 2013.
doi:10.1103/PhysRevLett.111.243007

3 **Marx, S.**, Adu Smith, D., Insero, G., Meek, S. A., Sartakov, B., Meijer, G., and Santambrogio, G.
Measuring and manipulating the temperature of cold molecules trapped on a chip.
Physical Review A, 92(6):063408, 2015.
doi:10.1103/physreva.92.063408

Selbstständigkeitserklärung

Hiermit erkläre ich, Silvio Marx, die vorliegende Arbeit selbstständig und nur unter Verwendung der angegebenen Hilfsmittel und Hilfen angefertigt zu haben. Die Arbeit wurde nicht schon einmal in einem früheren Promotionsverfahren angenommen oder als ungenügend beurteilt.

Ort, Datum	Unterschrift

Academic Curriculum Vitae

For reasons of data protection, the curriculum vitae is not included in the online version.

Aus Gründen des Datenschutzes ist der Lebenslauf in der Onlineversion nicht enthalten.

Bibliography

[Abel12a] Abel, M. J. Private communication, 2012.

[Abel12b] Abel, M. J., Marx, S., Meijer, G., and Santambrogio, G. Vibrationally exciting molecules trapped on a microchip. *Mol. Phys.*, 110(15-16):1829, 2012. doi:10.1080/00268976.2012.683885.

[André06] André, A. A., DeMille, D., Doyle, J. M., Lukin, M. D., Maxwell, S. E., Rabl, P., Schoelkopf, R. J., and Zoller, P. A coherent all-electrical interface between polar molecules and mesoscopic superconducting resonators. *Nat. Phys.*, 2:636, 2006. doi:10.1038/nphys386.

[Ashfold88] Ashfold, M. N. R., Dixon, R. N., Little, N., Stickland, R. J., and Western, C. M. The $\tilde{B}^1$ E' state of ammonia: Sub-Doppler spectroscopy at vacuum ultraviolet energies. *J. Chem. Phys.*, 89(4):1754, 1988. doi:10.1063/1.455715.

[Ashfold94] Ashfold, M. N. R. and Howe, J. D. Multiphoton Spectroscopy of Molecular Species. *Annu. Rev. Phys. Chem.*, 45(1):57, 1994. doi:10.1146/annurev.pc.45.100194.000421.

[Atkins05] Atkins, P. W. and Friedman, R. *Molecular Quantum Mechanics*. Oxford University Press, fourth edition, 2005. ISBN 978-0-19-927498-7.

[Bagdonaite13] Bagdonaite, J., Jansen, P., Henkel, C., Bethlem, H. L., Menten, K. M., and Ubachs, W. A Stringent Limit on a Drifting Proton-to-Electron Mass Ratio from Alcohol in the Early Universe. *Science*, 339:46, 2013. doi:10.1126/science.1224898.

[Baron14] Baron, J., Campbell, W. C., DeMille, D., Doyle, J. M., Gabrielse, G., Gurevich, Y. V., Hess, P. W., Hutzler, N. R., Kirilov, E., Kozyryev, I., O'Leary, B. R., Panda, C. D., Parsons, M. F., Petrik, E. S., Spaun, B., Vutha, A. C., and West, A. D. Order of Magnitude Smaller Limit on the Electric Dipole Moment of the Electron. *Science*, 343:269, 2014. doi:10.1126/science.1248213.

[Bertsche14] Bertsche, B. *Low Energy Collisions in Merged Neutral Molecular Beams*. Ph.D. thesis, École polytechnique fédérale de Lausanne, 2014. doi:10.5075/epfl-thesis-6210.

[Bethlem99] Bethlem, H. L., Berden, G., and Meijer, G. Decelerating Neutral Dipolar Molecules. *Phys. Rev. Lett.*, 83:1558, 1999. doi:10.1103/PhysRevLett.83.1558.

[Bethlem00] Bethlem, H. L., Berden, G., Crompvoets, F. M. H., Jongma, R. T., van Roij, A. J. A., and Meijer, G. Electrostatic trapping of ammonia molecules. *Nature*, 406:491, 2000. doi:10.1038/35020030.

[Bethlem02] Bethlem, H. L. *Deceleration And Trapping Of Polar Molecules Using Time-Varying Electric Fields*. Ph.D. thesis, Katholieke Universiteit Nijmegen, 2002. URL `http://hdl.handle.net/2066/19162`.

[Bethlem08] Bethlem, H. L., Kajita, M., Sartakov, B., Meijer, G., and Ubachs, W. Prospects for precision measurements on ammonia molecules in a fountain. *Eur. Phys. J. Special Topics*, 163:55, 2008. doi:10.1140/epjst/e2008-00809-5.

[Böhi09] Böhi, P., Riedel, M. F., Hoffrogge, J., Reichel, J., Hänsch, T. W., and Treutlein, P. Coherent manipulation of Bose–Einstein condensates with state-dependent microwave potentials on an atom chip. *Nat. Phys.*, 5(8):592, 2009. doi:10.1038/nphys1329.

[Born27] Born, M. Das Adiabatenprinzip in der Quantenmechanik. *Z. Phys.*, 40(3-4):167, 1927. doi:10.1007/bf01400360.

[Born28] Born, M. and Fock, V. Beweis des Adiabatensatzes. *Z. Phys.*, 51(3-4):165, 1928. doi:10.1007/bf01343193.

[Brown03] Brown, J. M. and Carrington, A. *Rotational Spectroscopy of Diatomic Molecules*. Cambridge University Press, 2003. ISBN 978-0-521-53078-1.

[Bücker09] Bücker, R., Perrin, A., Manz, S., Betz, T., Koller, C., Plisson, T., Rottmann, J., Schumm, T., and Schmiedmayer, J. Single-particle-sensitive imaging of freely propagating ultracold atoms. *New J. Phys.*, 11(10):103039, 2009. doi:10.1088/1367-2630/11/10/103039.

[Bulleid12] Bulleid, N. E., Hendricks, R. J., Hinds, E. A., Meek, S. A., Meijer, G., Osterwalder, A., and Tarbutt, M. R. Traveling-wave deceleration of heavy polar molecules in low-field-seeking states. *Phys. Rev. A*, 86:021404(R), 2012. doi:10.1103/PhysRevA.86.021404.

[Bunker04] Bunker, P. R. and Jensen, P. *The Fundamentals of Molecular Symmetry*. Institute of Physics Publishing, 2004. ISBN 978-0-7503-0941-7.

[Bunker06] Bunker, P. R. and Jensen, P. *Molecular Symmetry and Spectroscopy*. NRC Research Press, second edition, 2006. ISBN 978-0-660-19628-2.

[Burdeaux90] Burdeaux, D., Townsend, P., Carr, J., and Garrou, P. Benzocyclobutene (BCB) dielectrics for the fabrication of high density, thin film multichip modules. *J. Electron. Mater.*, 19(12):1357, 1990. doi:10.1007/bf02662825.

[Carr09] Carr, L. D., DeMille, D., Krems, R. V., and Ye, J. Cold and ultracold molecules: science, technology and applications. *New J. Phys.*, 11(5):055049, 2009. doi:10.1088/1367-2630/11/5/055049.

[Clarke08] Clarke, J. and Wilhelm, F. K. Superconducting quantum bits. *Nature*, 453(7198):1031, 2008. doi:10.1038/nature07128.

[Cleeton34] Cleeton, C. E. and Williams, N. H. Electromagnetic Waves of 1.1 cm Wave-Length and the Absorption Spectrum of Ammonia. *Phys. Rev.*, 45:234, 1934. doi:10.1103/PhysRev.45.234.

[Daussy99] Daussy, C., Marrel, T., Amy-Klein, A., Nguyen, C. T., Bordé, C. J., and Chardonnet, C. Limit on the Parity Nonconserving Energy Difference between the Enantiomers of a Chiral Molecule by Laser Spectroscopy. *Phys. Rev. Lett.*, 83:1554, 1999. doi:10.1103/PhysRevLett.83.1554.

[Daussy07] Daussy, C., Guinet, M., Amy-Klein, A., Djerroud, K., Hermier, Y., Briaudeau, S., Bordé, C. J., and Chardonnet, C. Direct Determination of the Boltzmann Constant by an Optical Method. *Phys. Rev. Lett.*, 98:250801, 2007. doi:10.1103/PhysRevLett.98.250801.

[Davies90] Davies, P. B. and Martin, P. A. Diode-laser spectroscopy of $a^3\Pi$ CO. *Mol. Phys.*, 70:89, 1990. doi:10.1080/00268979000100861.

[Daw06] Daw, R. and Finkelstein, J. Lab on a chip. *Nature*, 442(7101):367, 2006. doi:10.1038/442367a.

[DeMille02] DeMille, D. Quantum Computation with Trapped Polar Molecules. *Phys. Rev. Lett.*, 88:067901, 2002. doi:10.1103/PhysRevLett.88.067901.

[deMiranda11] de Miranda, M. H. G., Chotia, A., Neyenhuis, B., Wang, D., Quéméner, G., Ospelkaus, S., Bohn, J. L., Ye, J., and Jin, D. S. Controlling the quantum stereodynamics of ultracold bimolecular reactions. *Nat. Phys.*, 7:502, 2011. doi:10.1038/nphys1939.

[Doyle95] Doyle, J. M., Friedrich, B., Kim, J., and Patterson, D. Buffer-gas loading of atoms and molecules into a magnetic trap. *Phys. Rev. A*, 52:R2515–R2518, 1995. doi:10.1103/PhysRevA.52.R2515.

[Drullinger80] Drullinger, R. E., Wineland, D. J., and Bergquist, J. C. High-resolution optical spectra of laser cooled ions. *J. Appl. Phys.*, 22(4):365, 1980. doi:10.1007/bf00901058.

[Dunlap53] Dunlap, W. C. and Watters, R. L. Direct Measurement of the Dielectric

Constants of Silicon and Germanium. *Phys. Rev.*, 92(6):1396, 1953. doi:10.1103/physrev.92.1396.

[Englert11] Englert, B. G. U., Mielenz, M., Sommer, C., Bayerl, J., Motsch, M., Pinkse, P. W. H., Rempe, G., and Zeppenfeld, M. Storage and Adiabatic Cooling of Polar Molecules in a Microstructured Trap. *Phys. Rev. Lett.*, 107:263003, 2011. doi:10.1103/PhysRevLett.107.263003.

[Eppink97] Eppink, A. T. J. B. and Parker, D. H. Velocity map imaging of ions and electrons using electrostatic lenses: Application in photoelectron and photofragment ion imaging of molecular oxygen. *Rev. Sci. Instrum.*, 68(9):3477, 1997. doi:10.1063/1.1148310.

[Erisman08] Erisman, J. W., Sutton, M. A., Galloway, J., Klimont, Z., and Winiwarter, W. How a century of ammonia synthesis changed the world. *Nat. Geosci.*, 1(10):636, 2008. doi:10.1038/ngeo325.

[Ertl08] Ertl, G. Reaktionen an Oberflächen: vom Atomaren zum Komplexen (Nobel-Vortrag). *Angew. Chem.*, 120(19):3578, 2008. doi:10.1002/ange.200800480.

[Feshbach58] Feshbach, H. Unified theory of nuclear reactions. *Ann. Phys.*, 5(4):357, 1958. doi:http://dx.doi.org/10.1016/0003-4916(58)90007-1.

[Field72] Field, R. W., Tilford, S. G., Howard, R. A., and Simmons, J. D. Fine Structure and Perturbation Analysis of the $a^3\Pi$ State of CO. *J. Mol. Spectrosc.*, 44:347, 1972. doi:10.1016/0022-2852(72)90110-5.

[Folman02] Folman, R., Krüger, P., Schmiedmayer, J., Denschlag, J., and Henkel, C. Microscopic Atom Optics: From Wires to an Atom Chip. volume 48 of *Advances in Atomic, Molecular, and Optical Physics*, page 263. Academic Press, 2002. ISBN 978-0-12-003848-0. doi:10.1016/S1049-250X(02)80011-8.

[Fortàgh07] Fortàgh, J. and Zimmermann, C. Magnetic microtraps for ultracold atoms. *Rev. Mod. Phys.*, 79:235, 2007. doi:10.1103/RevModPhys.79.235.

[Fusina86] Fusina, L., Di Lonardo, G., and Johns, J. W. C. The ν_2 and ν_4 bands of $^{14}ND_3$. *J. Mol. Spectrosc.*, 118(2):397, 1986. doi:10.1016/0022-2852(86)90178-5.

[Fusina91] Fusina, L., Carlotti, M., Di Lonardo, G., Murzin, S. N., and Stepanov, O. N. Pure inversion and inversion-rotation spectra of $^{15}ND_3$ in the ground state. *J. Mol. Spectrosc.*, 147(1):71, 1991. doi:10.1016/0022-2852(91)90169-b.

[Gerhards04] Gerhards, M. High energy and narrow bandwidth mid IR nanosecond laser system. *Opt. Commun.*, 241:493, 2004.

doi:10.1016/j.optcom.2004.07.035.

[Gilijamse06] Gilijamse, J. J., Hoekstra, S., van de Meerakker, S. Y. T., Groenenboom, G. C., and Meijer, G. Near-Threshold Inelastic Collisions Using Molecular Beams with a Tunable Velocity. *Science*, 313(5793):1617, 2006. doi:10.1126/science.1131867.

[Gilijamse07] Gilijamse, J. J., Hoekstra, S., Meek, S. A., Metsälä, M., van de Meerakker, S. Y. T., Meijer, G., and Groenenboom, G. C. The radiative lifetime of metastable CO ($a^3\Pi$, $v = 0$). *J. Chem. Phys.*, 127:221102, 2007. doi:10.1063/1.2813888.

[González-Flórez11] González-Flórez, A. I., Meek, S. A., Haak, H., Conrad, H., Santambrogio, G., and Meijer, G. An electrostatic elliptical mirror for neutral polar molecules. *Phys. Chem. Chem. Phys.*, 13:18830, 2011. doi:10.1039/c1cp20957d.

[Gordon54] Gordon, J. P., Zeiger, H. J., and Townes, C. H. Molecular Microwave Oscillator and New Hyperfine Structure in the Microwave Spectrum of NH_3. *Phys. Rev.*, 95:282, 1954. doi:10.1103/PhysRev.95.282.

[Gordon55] Gordon, J. P., Zeiger, H. J., and Townes, C. H. The Maser—New Type of Microwave Amplifier, Frequency Standard, and Spectrometer. *Phys. Rev.*, 99:1264, 1955. doi:10.1103/PhysRev.99.1264.

[Gring12] Gring, M., Kuhnert, M., Langen, T., Kitagawa, T., Rauer, B., Schreitl, M., Mazets, I., Adu Smith, D., Demler, E., and Schmiedmayer, J. Relaxation and Prethermalization in an Isolated Quantum System. *Science*, 337(6100):1318, 2012. doi:10.1126/science.1224953.

[Hammer15] Hammer, J., Thomas, S., Weber, P., and Hommelhoff, P. Microwave chip-based beam splitter for low-energy guided electrons. *Phys. Rev. Lett.*, 114:254801, 2015. doi:10.1103/PhysRevLett.114.254801.

[Hänsel01] Hänsel, W., Hommelhoff, P., Hänsch, T. W., and Reichel, J. Bose-Einstein condensation on a microelectronic chip. *Nature*, 413:498, 2001. doi:10.1038/35097032.

[Hazzard14] Hazzard, K. R. A., Gadway, B., Foss-Feig, M., Yan, B., Moses, S. A., Covey, J. P., Yao, N. Y., Lukin, M. D., Ye, J., Jin, D. S., and Rey, A. M. Many-Body Dynamics of Dipolar Molecules in an Optical Lattice. *Phys. Rev. Lett.*, 113(19):195302, 2014. doi:10.1103/physrevlett.113.195302.

[Henkel99] Henkel, C. and Wilkens, M. Heating of trapped atoms near thermal surfaces. *Europhys. Lett.*, 47(4):414, 1999. doi:10.1209/epl/i1999-00404-8.

[Henkel12] Henkel, C., Menten, K. M., Murphy, M. T., Flambaum, V. V., Levshakov, S. A., Lapinov, A. V., Molaro, P., and Braatz, J. A.

Ammonia as a tracer of fundamental constants. In *The Twelfth Marcel Grossmann Meeting*, volume B of *Proceedings of the MG12 Meeting on General Relativity*, page 1500. World Scientific, 2012. doi:10.1142/9789814374552_0256.

[Ho83] Ho, P. T. P. and Townes, C. H. Interstellar Ammonia. *Annu. Rev. Astron. Astrophys.*, 21(1):239, 1983. doi:10.1146/annurev.aa.21.090183.001323.

[Hoekstra07] Hoekstra, S., Gilijamse, J. J., Sartakov, B., Vanhaecke, N., Scharfenberg, L., van de Meerakker, S. Y. T., and Meijer, G. Optical Pumping of Trapped Neutral Molecules by Blackbody Radiation. *Phys. Rev. Lett.*, 98:133001, 2007. doi:10.1103/PhysRevLett.98.133001.

[Huber79] Huber, K. and Herzberg, G. *Molecular Spectra and Molecular Structure*, volume IV. Constants of Diatomic Molecules. Van Nostrand, 1979. ISBN 978-0-442-23394-5.

[Hudson06] Hudson, E. R., Lewandowski, H. J., Sawyer, B. C., and Ye, J. Cold Molecule Spectroscopy for Constraining the Evolution of the Fine Structure Constant. *Phys. Rev. Lett.*, 96(14):143004, 2006. doi:10.1103/physrevlett.96.143004.

[Hudson11] Hudson, J. J., Kara, D. M., Smallman, I. J., Sauer, B. E., Tarbutt, M. R., and Hinds, E. A. Improved measurement of the shape of the electron. *Nature*, 473(7348):493, 2011. doi:10.1038/nature10104.

[Hüttner74] Hüttner, W. Symmetric top molecules. In *Molecular Constants from Microwave, Molecular Beam, and Electron Spin Resonance Spectroscopy*, volume 6 of *Landolt-Börnstein - Group II Molecules and Radicals*, page 416. Springer Berlin Heidelberg, 1974. ISBN 978-3-540-05977-6. doi:10.1007/10201226_56.

[Jansen13] Jansen, P., Quintero-Pérez, M., Wall, T. E., van den Berg, J. E., Hoekstra, S., and Bethlem, H. L. Deceleration and trapping of ammonia molecules in a traveling-wave decelerator. *Phys. Rev. A*, 88:043424, 2013. doi:10.1103/PhysRevA.88.043424.

[Jongma97] Jongma, R. T. *Molecular Beam Experiments and Scattering Studies with State-Selected Metastable CO*. Ph.D. thesis, Katholieke Universiteit Nijmegen, 1997. URL `http://hdl.handle.net/2066/40146`.

[Ketterle99] Ketterle, W., Durfee, D. S., and Stamper-Kurn, D. M. Making, probing and understanding Bose-Einstein condensates. *Proc. Internat. School Phys. Enrico Fermi*, page 67, 1999. Also published as arXiv:cond-mat/9904034.

[Kirste09] Kirste, M., Sartakov, B. G., Schnell, M., and Meijer, G. Nonadiabatic transitions in electrostatically trapped ammonia molecules. *Phys. Rev. A*, 79:051401(R), 2009. doi:10.1103/PhysRevA.79.051401.

[Krems08] Krems, R. V. Cold controlled chemistry. *Phys. Chem. Chem. Phys.*, 10:4079, 2008. doi:10.1039/B802322K.

[Kukolich73] Kukolich, S. G. and Casleton, K. H. Molecular Zeeman effect in NH_3. *Chem. Phys. Lett.*, 18(3):408, 1973. doi:10.1016/0009-2614(73)80203-9.

[Landau93] Landau, L. D. and Lifshitz, E. M. *Mechanics*. Butterworth-Heinemann, third edition, 1993. ISBN 978-0-7506-2896-9.

[Lefebvre-Brion04] Lefebvre-Brion, H. and Field, R. W. *The Spectra and Dynamics of Diatomic Molecules*. Elsevier Academic Press, 2004. ISBN 978-0-12-441455-6.

[LinodaSilva06] Lino da Silva, M. and Dudeck, M. Arrays of radiative transition probabilities for CO_2-N_2 plasmas. *J. Quant. Spectrosc. Ra.*, 102(3):348, 2006. doi:10.1016/j.jqsrt.2006.02.018.

[Marbach11] Marbach, J., Bronold, F. X., and Fehske, H. Auger de-excitation of metastable molecules at metallic surfaces. *Phys. Rev. B*, 84:085443, 2011. doi:10.1103/PhysRevB.84.085443.

[Martin91] Martin, J. M. L., François, J. P., and Gijbels, R. On the effect of centrifugal stretching on the rotational partition function of an asymmetric top. *J. Chem. Phys.*, 95(11):8374, 1991. doi:10.1063/1.461265.

[Marx13] Marx, S., Adu Smith, D., Abel, M. J., Zehentbauer, T., Meijer, G., and Santambrogio, G. Imaging Cold Molecules on a Chip. *Phys. Rev. Lett.*, 111:243007, 2013. doi:10.1103/PhysRevLett.111.243007.

[Meek08] Meek, S. A., Bethlem, H. L., Conrad, H., and Meijer, G. Trapping Molecules on a Chip in Traveling Potential Wells. *Phys. Rev. Lett.*, 100:153003, 2008. doi:10.1103/PhysRevLett.100.153003.

[Meek09a] Meek, S. A., Conrad, H., and Meijer, G. A Stark decelerator on a chip. *New J. Phys.*, 11(5):055024, 2009. doi:10.1088/1367-2630/11/5/055024.

[Meek09b] Meek, S. A., Conrad, H., and Meijer, G. Trapping Molecules on a Chip. *Science*, 324(5935):1699, 2009. doi:10.1126/science.1175975.

[Meek10] Meek, S. A. *A Stark decelerator on a chip*. Ph.D. thesis, Freie Universität Berlin, 2010. URL `http://www.diss.fu-berlin.de/diss/receive/FUDISS_thesis_000000019286`.

[Meek11a] Meek, S. A., Parsons, M. F., Heyne, G., Platschkowski, V., Haak, H., Meijer, G., and Osterwalder, A. A traveling wave decelerator for neutral polar molecules. *Rev. Sci. Instrum.*, 82(9):093108, 2011.

doi:10.1063/1.3640413.

[Meek11b] Meek, S. A., Santambrogio, G., Sartakov, B. G., Conrad, H., and Meijer, G. Suppression of nonadiabatic losses of molecules from chip-based microtraps. *Phys. Rev. A*, 83:033413, 2011. doi:10.1103/PhysRevA.83.033413.

[Metcalf99] Metcalf, H. J. and van der Straten, P. *Laser Cooling and Trapping*. Springer Berlin, 1999. ISBN 978-0-387-98728-6.

[Milonni10] Milonni, P. W. and Eberly, J. H. *Laser Physics*. John Wiley & Sons, 2010. ISBN 978-0-470-38771-9.

[Mølhave00] Mølhave, K. and Drewsen, M. Formation of translationally cold MgH^+ and MgD^+ molecules in an ion trap. *Phys. Rev. A*, 62(1):011401(R), 2000. doi:10.1103/physreva.62.011401.

[Morse96] Morse, M. D. 2. Supersonic Beam Sources. In F. Dunning and R. G. Hulet, editors, *Atomic, Molecular, and Optical Physics: Atoms and Molecules*, volume 29, Part B of *Experimental Methods in the Physical Sciences*, page 21. Academic Press, 1996. ISBN 978-0-12-475976-3. doi:10.1016/S0076-695X(08)60784-X.

[Myatt97] Myatt, C. J., Burt, E. A., Ghrist, R. W., Cornell, E. A., and Wieman, C. E. Production of Two Overlapping Bose-Einstein Condensates by Sympathetic Cooling. *Phys. Rev. Lett.*, 78(4):586, 1997. doi:10.1103/physrevlett.78.586.

[Norrgard16] Norrgard, E. B., McCarron, D. J., Steinecker, M. H., Tarbutt, M. R., and DeMille, D. Submillikelvin Dipolar Molecules in a Radio-Frequency Magneto-Optical Trap. *Phys. Rev. Lett.*, 116:063004, 2016. doi:10.1103/PhysRevLett.116.063004.

[Ockeloen10] Ockeloen, C. F., Tauschinsky, A. F., Spreeuw, R. J. C., and Whitlock, S. Detection of small atom numbers through image processing. *Phys. Rev. A*, 82:061606(R), 2010. doi:10.1103/PhysRevA.82.061606.

[Ospelkaus10] Ospelkaus, S., Ni, K.-K., Wang, D., de Miranda, M. H. G., Neyenhuis, B., Quéméner, G., Julienne, P. S., Bohn, J. L., Jin, D. S., and Ye, J. Quantum-State Controlled Chemical Reactions of Ultracold Potassium-Rubidium Molecules. *Science*, 327(5967):853, 2010. doi:10.1126/science.1184121.

[Ospelkaus11] Ospelkaus, C., Warring, U., Colombe, Y., Brown, K. R., Amini, J. M., Leibfried, D., and Wineland, D. J. Microwave quantum logic gates for trapped ions. *Nature*, 476(7359):181, 2011. doi:10.1038/nature10290.

[Osterwalder10] Osterwalder, A., Meek, S. A., Hammer, G., Haak, H., and Meijer, G. Deceleration of neutral molecules in macroscopic traveling traps. *Phys.*

Rev. A, 81:051401(R), 2010. doi:10.1103/PhysRevA.81.051401.

[Padgett11] Padgett, M. and Di Leonardo, R. Holographic optical tweezers and their relevance to lab on chip devices. *Lab Chip*, 11:1196, 2011. doi:10.1039/C0LC00526F.

[Penning27] Penning, F. M. Über Ionisation durch metastabile Atome. *Naturwissenschaften*, 15(40):818, 1927. doi:10.1007/BF01505431.

[Petrich95] Petrich, W., Anderson, M. H., Ensher, J. R., and Cornell, E. A. Stable, Tightly Confining Magnetic Trap for Evaporative Cooling of Neutral Atoms. *Phys. Rev. Lett.*, 74:3352, 1995. doi:10.1103/PhysRevLett.74.3352.

[Prehn16] Prehn, A., Ibrügger, M., Glöckner, R., Rempe, G., and Zeppenfeld, M. Optoelectrical Cooling of Polar Molecules to Submillikelvin Temperatures. *Phys. Rev. Lett.*, 116:063005, 2016. doi:10.1103/PhysRevLett.116.063005.

[Quéméner12] Quéméner, G. and Julienne, P. S. Ultracold Molecules under Control! *Chem. Rev.*, 112(9):4949, 2012. doi:10.1021/cr300092g.

[Quintero-Pérez13] Quintero-Pérez, M., Jansen, P., Wall, T. E., van den Berg, J. E., Hoekstra, S., and Bethlem, H. L. Static Trapping of Polar Molecules in a Traveling Wave Decelerator. *Phys. Rev. Lett.*, 110:133003, 2013. doi:10.1103/PhysRevLett.110.133003.

[Reichel10] Reichel, J. and Vuletic, V. *Atom Chips*. Wiley-VCH, 2010. ISBN 978-3-527-40755-2.

[Salumbides08] Salumbides, E. J., Bailly, D., Khramov, A., Wolf, A. L., Eikema, K. S. E., Vervloet, M., and Ubachs, W. Improved Laboratory Values of the H_2 Lyman and Werner Lines for Constraining Time Variation of the Proton-to-Electron Mass Ratio. *Phys. Rev. Lett.*, 101:223001, 2008. doi:10.1103/PhysRevLett.101.223001.

[Salumbides11] Salumbides, E. J., Dickenson, G. D., Ivanov, T. I., and Ubachs, W. QED Effects in Molecules: Test on Rotational Quantum States of H_2. *Phys. Rev. Lett.*, 107:043005, 2011. doi:10.1103/PhysRevLett.107.043005.

[Santambrogio11] Santambrogio, G., Meek, S. A., Abel, M. J., Duffy, L. M., and Meijer, G. Driving Rotational Transitions in Molecules on a Chip. *ChemPhysChem*, 12(10):1799, 2011. doi:10.1002/cphc.201001007.

[Sawyer08] Sawyer, B. C., Stuhl, B. K., Lev, B. L., Ye, J., and Hudson, E. R. Mitigation of loss within a molecular Stark decelerator. *Eur. Phys. J. D*, 48(2):197, 2008. doi:10.1140/epjd/e2008-00097-y.

[Schleipen92] Schleipen, J. J. H. B. *State-to-State Cross Sections for Rotational Exci-*

tation of NH_3 and OH by Collisions with He, Ar and H_2. Ph.D. thesis, Katholieke Universiteit Nijmegen, 1992. URL `http://hdl.handle.net/2066/114129`.

[Schulz04] Schulz, S. A., Bethlem, H. L., van Veldhoven, J., Küpper, J., Conrad, H., and Meijer, G. Microstructured Switchable Mirror for Polar Molecules. *Phys. Rev. Lett.*, 93:020406, 2004. doi:10.1103/PhysRevLett.93.020406.

[Schumm05] Schumm, T., Hofferberth, S., Andersson, L. M., Wildermuth, S., Groth, S., Bar-Joseph, I., Schmiedmayer, J., and Krüger, P. Matter-wave interferometry in a double well on an atom chip. *Nat. Phys.*, 1:57, 2005. doi:10.1038/nphys125.

[Schwenker65] Schwenker, R. P. Experimental Oscillator Strengths of CO and CO^+. *J. Chem. Phys.*, 42:1895, 1965. doi:10.1063/1.1696223.

[Shagam15] Shagam, Y., Klein, A., Skomorowski, W., Yun, R., Averbukh, V., Koch, C. P., and Narevicius, E. Molecular hydrogen interacts more strongly when rotationally excited at low temperatures leading to faster reactions. *Nat. Chem.*, 7(11):921, 2015. doi:10.1038/nchem.2359.

[Shelkovnikov08] Shelkovnikov, A., Butcher, R. J., Chardonnet, C., and Amy-Klein, A. Stability of the Proton-to-Electron Mass Ratio. *Phys. Rev. Lett.*, 100(15):150801, 2008. doi:10.1103/physrevlett.100.150801.

[Smith11] Smith, D. A., Aigner, S., Hofferberth, S., Gring, M., Andersson, M., Wildermuth, S., Krüger, P., Schneider, S., Schumm, T., and Schmiedmayer, J. Absorption imaging of ultracold atoms on atom chips. *Opt. Express*, 19(9):8471, 2011. doi:10.1364/OE.19.008471.

[Stick06] Stick, D., Hensinger, W. K., Olmschenk, S., Madsen, M. J., Schwab, K., and Monroe, C. Ion trap in a semiconductor chip. *Nat. Phys.*, 2(1):36, 2006. doi:10.1038/nphys171.

[Strekalov95] Strekalov, M. L. Rotational relaxation and collisional energy transfer. *Mol. Phys.*, 86(1):39, 1995. doi:10.1080/00268979500101831.

[Stwalley99] Stwalley, W. C. and Wang, H. Photoassociation of ultracold atoms: A new spectroscopic technique. *J. Mol. Spectrosc.*, 195(2):194, 1999. ISSN 0022-2852. doi:10.1006/jmsp.1999.7838.

[Swalen62] Swalen, J. D. and Ibers, J. A. Potential Function for the Inversion of Ammonia. *J. Chem. Phys.*, 36(7):1914, 1962. doi:10.1063/1.1701290.

[Townes75] Townes, C. H. and Schawlow, A. L. *Microwave Spectroscopy*. Dover Publications, Inc., 1975. ISBN 978-0-486-61798-5.

[Truppe13] Truppe, S., Hendricks, R. J., Tokunaga, S. K., Lewandowski, H. J., Kozlov, M. G., Henkel, C., Hinds, E. A., and Tarbutt, M. R. A search for varying fundamental constants using hertz-level frequency measurements of cold CH molecules. *Nat. Commun.*, 4:2600, 2013. doi:10.1038/ncomms3600.

[Tscherbul08] Tscherbul, T. V. and Krems, R. V. Quantum theory of chemical reactions in the presence of electromagnetic fields. *J. Chem. Phys.*, 129:034112, 2008. doi:10.1063/1.2954021.

[vandeMeerakker05] van de Meerakker, S. Y. T., Vanhaecke, N., van der Loo, M., Groenenboom, G., and Meijer, G. Direct Measurement of the Radiative Lifetime of Vibrationally Excited OH Radicals. *Phys. Rev. Lett.*, 95(1):013003, 2005. doi:10.1103/physrevlett.95.013003.

[vandeMeerakker12] van de Meerakker, S. Y. T., Bethlem, H. L., Vanhaecke, N., and Meijer, G. Manipulation and Control of Molecular Beams. *Chem. Rev.*, 112(9):4828, 2012. doi:10.1021/cr200349r.

[vandenBerg14] van den Berg, J. E., Mathavan, S. C., Meinema, C., Nauta, J., Nijbroek, T. H., Jungmann, K., Bethlem, H. L., and Hoekstra, S. Traveling-wave deceleration of SrF molecules. *J. Mol. Spectrosc.*, 300:22, 2014. doi:10.1016/j.jms.2014.02.004.

[vanVeldhoven04] van Veldhoven, J., Küpper, J., Bethlem, H. L., Sartakov, B., Roij, A. J. A., and Meijer, G. Decelerated molecular beams for high-resolution spectroscopy. *Eur. Phys. J. D*, 31(2):337, 2004. doi:10.1140/epjd/e2004-00160-9.

[vanVeldhoven06] van Veldhoven, J. *AC trapping and high-resolution spectroscopy of ammonia molecules*. Ph.D. thesis, Radboud Universiteit Nijmegen, 2006. URL `http://hdl.handle.net/2066/29874`.

[vanZoest10] van Zoest, T., Gaaloul, N., Singh, Y., Ahlers, H., Herr, W., Seidel, S. T., Ertmer, W., Rasel, E., Eckart, M., Kajari, E., Arnold, S., Nandi, G., Schleich, W. P., Walser, R., Vogel, A., Sengstock, K., Bongs, K., Lewoczko-Adamczyk, W., Schiemangk, M., Schuldt, T., Peters, A., Könemann, T., Müntinga, H., Lämmerzahl, C., Dittus, H., Steinmetz, T., Hänsch, T. W., and Reichel, J. Bose-Einstein Condensation in Microgravity. *Science*, 328(5985):1540, 2010. doi:10.1126/science.1189164.

[Velarde10] Velarde, L., Engelhart, D. P., Matsiev, D., LaRue, J., Auerbach, D. J., and Wodtke, A. M. Generation of tunable narrow bandwidth nanosecond pulses in the deep ultraviolet for efficient optical pumping and high resolution spectroscopy. *Rev. Sci. Instrum.*, 81(6):063106, 2010. doi:10.1063/1.3436973.

[Vogels15] Vogels, S. N., Onvlee, J., Chefdeville, S., van der Avoird, A., Groenenboom, G. C., and van de Meerakker, S. Y. T. Imaging resonances in low-energy NO-He inelastic collisions. *Science*, 350(6262):787, 2015. doi:10.1126/science.aad2356.

[Špirko83] Špirko, V. Vibrational anharmonicity and the inversion potential function of NH_3. *J. Mol. Spectrosc.*, 101(1):30, 1983. doi:10.1016/0022-2852(83)90004-8.

[Weiss89] Weiss, D. S., Riis, E., Shevy, Y., Ungar, P. J., and Chu, S. Optical molasses and multilevel atoms: experiment. *J. Opt. Soc. Am. B*, 6(11):2072, 1989. doi:10.1364/JOSAB.6.002072.

[Wicke72] Wicke, B. G., Field, R. W., and Klemperer, W. Fine Structure, Dipole Moment, and Perturbation Analysis of $a^3\Pi$ CO. *J. Chem. Phys.*, 56(12):5758, 1972. doi:10.1063/1.1677113.

[Wing84] Wing, W. H. On neutral particle trapping in quasistatic electromagnetic fields. *Prog. Quant. Electron.*, 8(3-4):181, 1984. doi:10.1016/0079-6727(84)90012-0.

[Woods88] Woods, R. C. and Saykally, R. J. A reanalysis of the molecular beam electric resonance Stark effect data for the $a^3\Pi$ state of carbon monoxide. *J. Chem. Phys.*, 89:2781, 1988. doi:10.1063/1.455031.

[Zare88] Zare, R. N. *Angular Momentum*. John Wiley & Sons, 1988. ISBN 978-0-471-85892-8.

[Zieger12] Zieger, P. C. *A Synchrotron for Polar Molecules*. Ph.D. thesis, Radboud Universiteit Nijmegen, 2012. URL `http://hdl.handle.net/2066/100603`.